Controlled light propagation in random, periodic, and superperiodic silicon nanophotonic materials

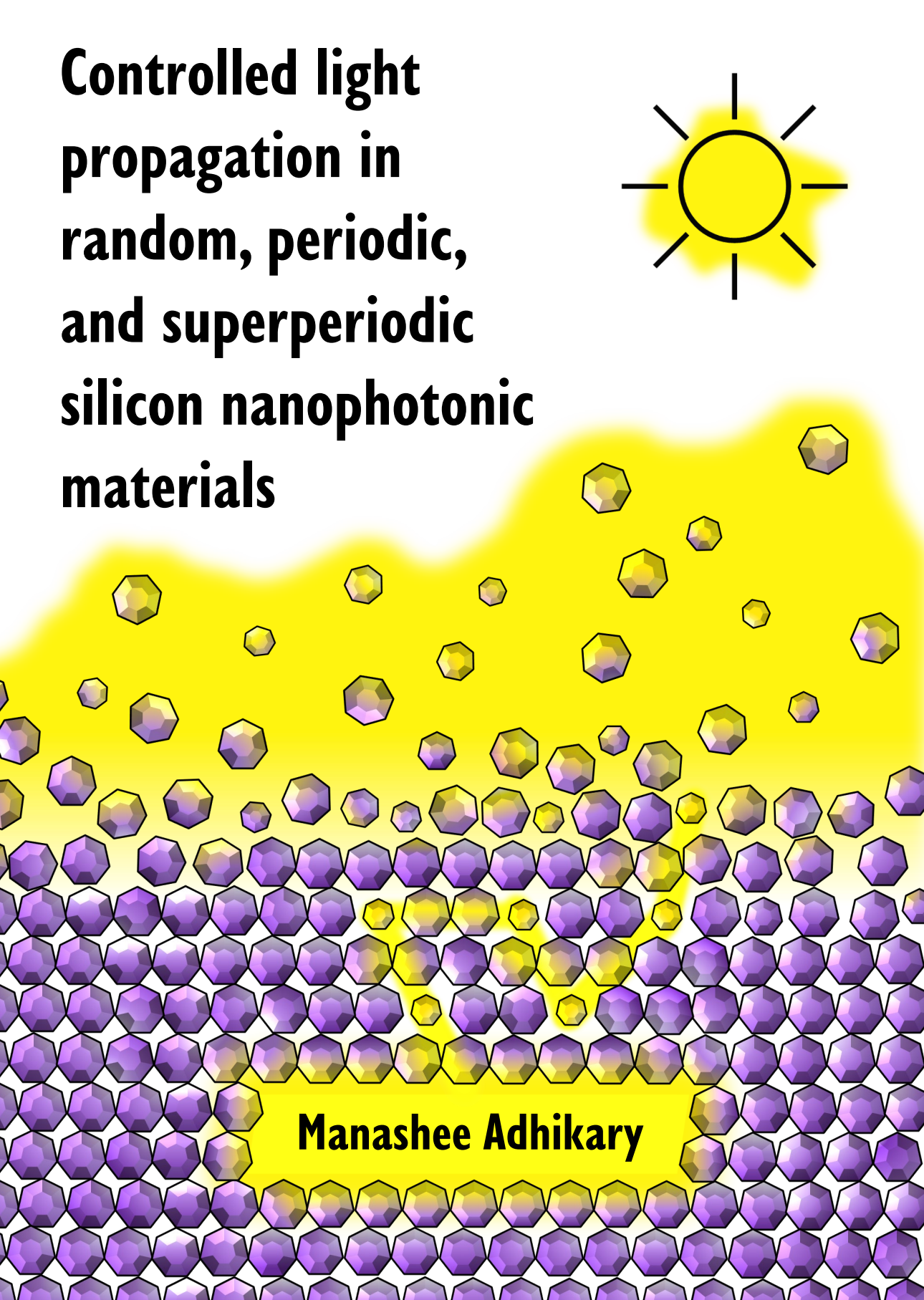

Manashee Adhikary

CONTROLLED LIGHT PROPAGATION IN RANDOM, PERIODIC, AND SUPERPERIODIC SILICON NANOPHOTONIC MATERIALS

Manashee Adhikary

CONTROLLED LIGHT PROPAGATION IN RANDOM, PERIODIC, AND SUPERPERIODIC SILICON NANOPHOTONIC MATERIALS

DISSERTATION

To obtain
the degree of doctor at the University of Twente,
on the authority of the rector magnificus,
prof.dr.ir. A. Veldkamp,
on account of the decision of the Doctorate Board,
to be publicly defended
on Thursday the 14th of October 2021 at 16.45 hours

by

Manashee Adhikary

Born on the 23rd of January 1992
in Guwahati, India.

This dissertation has been approved by:

Supervisor:
prof.dr. W.L. Vos

Co-supervisor:
dr. R. Uppu

Cover: Artistic illustration of light propagation. Randomly arranged particles scatter light everywhere while defects within periodically arranged particles guide light towards and store light in a space containing the author's name within the periodic part that depicts the photonic band gap crystal. Concept and design by M. Adhikary.
Printed by: Gildeprint, Enschede, The Netherlands
ISBN: 978-90-365-5236-3
DOI: 10.3990/1.9789036552363

Graduation Committee:

Chair/secretary	prof.dr.ir. J.L. Herek
Supervisor	prof.dr. W. L. Vos
Co-supervisor	dr. R. Uppu
Committee Members	prof.dr. S. M. García Blanco prof.dr. M. D. Ackermann prof.dr. A. P. Mosk prof.dr. W. Bogaerts

This work was financially supported by NWO-TTW program "Free-form Scattering Optics P15-36" and NWO "Stirring of Light!".

It was carried out at the
Complex Photonic Systems (COPS) chair,
Faculty of Science and Technology
and MESA+ Institute for Nanotechnology,
University of Twente, P.O. Box 217,
7500 AE Enschede, The Netherlands.

Contents

Chapter 1

Introduction

The goal of this thesis is to steer light deep inside otherwise opaque media. Opaque media are those that strongly interact with light, leading to low transmission and high scattering or reflection. We perform experimental studies on samples that interact with light in different manners. The opaque samples range from randomly distributed nanoparticles that scatter light in all directions to 3D periodically ordered photonic crystals with a forbidden range of light frequencies, a full photonic band gap, and even superperiodic structures, namely 3D arrays of coupled resonating cavities in a 3D band gap. In presence of multiple scattering, the wavefront shaping phase modulation technique is used to focus light behind or inside the medium. We apply this technique to photonic crystals with a forbidden energy gap for light that have intrinsic fabrication disorder that results in multiple scattering. By adding periodically repeated cavities in 3D band gap crystals, we finally present a novel controlled wave transport in superperiodic media, where light hops from cavity to cavity within an otherwise forbidden photonic band gap.

1.1 Light

Light gets tremendous attention from people all around the world, opening up numerous research fields and contributing to ever-growing high-tech industries and exploring new physics. Manipulation of light, be in the form of spectral, temporal, or spatial, offers variety of applications. In various techniques such as sensing, imaging, manufacturing, light finds its application in the fields of medical science, astronomy, environment, communication, and recently even in integrated circuits [1]. Therefore, playing with light has been a huge interest for industrial and academic researchers in pursuit of finding even more ways to manipulate and control light, to solve specific questions, ease life or just to explore new,

interesting scientific phenomena.

When we speak of light here, we mean not only the colorful visible radiation, but also the infrared (IR) radiation typical of heat, and highly energetic ultraviolet (UV) light. As is well-known, light is an electromagnetic (EM) wave, where electric and magnetic fields oscillate perpendicular to the light propagation direction [2, 3]. If the field oscillates in a certain direction, then the radiation is called polarized and its polarization is given by the oscillation direction of the electric field. There are mainly two types of polarization states: linear and circular or elliptical. In the first case the fields oscillate in a single direction, while in the latter case the fields rotate at a constant rate in a plane as light propagates. In this thesis, we typically work with linearly polarized light. The intensity of light is proportional to the square of the amplitudes of its constituent fields, while the oscillation frequency ν determines the energy of light, given by the Planck-Einstein relation $E = h\nu$, where h is Planck's constant. Light has frequencies that varies from about 10^{13} Hz (IR) to 10^{16} Hz (UV). The spatial frequency is also expresses as wavenumber (in cm^{-1}), which is the number of cycles per unit distance. The corresponding wavelength of light waves are expressed as $\lambda = \frac{c}{\nu}$, where c is the speed of light in the medium. IR waves have frequency lower than that of visible light and invisible to human eye. For both short and long-range wireless communications IR waves are used. The different optical communication bands in IR are given in Table 1.1. In this thesis, we perform experiments with the near infrared (NIR) range. Here we use the term NIR to define the range including all the infrared communication bands listed above ($5000 < \nu/c < 10000$ or $1000\ \mathrm{nm} < \lambda < 2000\ \mathrm{nm}$).

The wavelength of light depends on the speed of light in the medium, and is related to the free-space wavelength by a certain property called the refractive index of the medium, defined as the ratio of speed of light in vacuum to that in the medium, $n = \frac{c_0}{c}$. Light is proverbially fast when it propagates through vacuum[1], and as soon as it enters other media such as glass or water, its phase velocity decreases as a result of disturbance in the charges of the medium by the electric field of light [3]. The refractive index n is defined by the ratio of speed of light in vacuum (c_0) to the speed of light in the medium (c), and the wavelength changes accordingly as $\lambda = \frac{\lambda_0}{n}$. If the incident light is polarized, certain types of media such as birefringent crystals [2, 5] or multiple scattering media [6], can alter the polarization state after light interacts with them. Thus, the medium in which light travels, plays a very important role in propagation of light.

1.2 Light in opaque media

In a medium with a spatially uniform refractive index, such as glass or water, light follows the simple laws of reflection and refraction [8]. In such cases, light

[1]Superluminal light is well-known, as is a negative light speed, see S. Chu *et al.* [4]

Table 1.1: The ranges of NIR telecommunication bands [7]

Band	**Wavelength range (nm)**	**Frequency range (cm^{-1})**	**Long name**
O-band	1260 - 1360	7936 - 7353	Original
E-band	1360 - 1460	7353 - 6849	Extended
S-band	1460 - 1530	6849 - 6536	Short wavelength
C-band	1530 - 1565	6536 - 6390	Conventional
L-band	1565 - 1625	6390 - 6154	Long wavelength
U-band	1625 - 1675	6154 - 5970	Ultralong wavelength

propagates in straight lines and propagation is well described by geometrical or ray optics [3]. Since light can pass through these media without any obstacles, there is no redirection or of light within the medium. However, when the refractive index varies spatially within the medium, whether in a randomly or periodic fashion, completely new behavior emerges. Due to the wave nature of light, when light encounters a medium that has refractive index variation on length scales comparable to the wavelength, alterations to light propagation take place in form of direction and phase, known as the scattering of light. The variation in refractive index can have a broad range of symmetries starting from fully random or disordered to periodic structures. Light waves become multiply scattered and display new behavior such as Anderson localization [9–11] . This behavior is called complexity [12], a field that extends over many types of waves, electrons, spins, and sound [13–16]. Since this field started from condensed matter, most terminology derives from that field. For instance, the waves are said to be strongly interacting with the photonic material when the refractive index contrast is so high that interference dominates the wave transport [17, 18]. When the refractive index has complex components, some part of the incident light is absorbed by the medium. The study of the interaction of light waves with matter is called Nanophotonics, and is a popular subject in physics [19–25].

Nanophotonic media interact with light and thereby alter the initial information of direction, phase, or intensity. A medium is opaque when it is not possible to see through it because of such nanophotonic interaction. Opacity in nanophotonic materials is caused by the underlying structure, be it random or periodic arrangements of the constituent matter. For example, a medium that randomly scatters most of the incident light appears opaque, *e.g.*, paper, paint, skin, clouds. It is important to note the frequency dependence of the opacity of different media because if the length scale variation of the medium is much smaller than the wavelength, the medium effectively appears uniform to that wavelength, for instance, water molecules are scatterers spaced by only about 0.5 nm and therefore a glass of water is transparent at much longer visible wavelengths. While the same glass of water scatters or absorbs shorter wavelengths.

Scattering of light in periodically arranged structures is explained by diffraction, such as crystallographic diffraction, similar to X-ray diffraction in atomic

and molecular crystals [26]. Since the wavelength of visible and IR light is much longer than that of X-rays (hence of periodicity of crystals), atomic or molecular crystals do not diffract visible or IR radiations. For such a range, periodic arrangement of materials with alternating refractive index creates photonic crystals that diffract light [10, 27, 28]. Such materials possess so-called photonic gaps that include a range of frequencies that are forbidden to enter the structure, thereby making it fully opaque for that range [29, 30].

In the following sections, we will discuss the types of real opaque media that we are going to study in this thesis, from random media to ordered periodic media with intentional defects, and how light interacts with them. In table 1.2, a summary of the four types of nanophotonic media studied in this thesis are shown from point of view of three parameters stated below:

- **Arrangement type:** The type of arrangement of constituent materials or particles with different refractive indices in the medium. For example, in random arrangement there is no correlation in the positioning of the particles, and periodic arrangement.
- **Density of states (DOS):** The DOS is the number of states per unit frequency interval in a given volume of the medium. DOS vanishes in media where light cannot exist.
- **Wave propagation:** Defines the ways waves propagate in a certain medium, which is determined by its structure and the DOS.

1.2.1 Scattering of light in disordered media

One important physical phenomenon that takes place in light-matter interaction is scattering of light. In nanophotonics, a widely studied system is a disordered medium that interacts with light by scattering, either elastic, inelastic (*e.g.* absorption), or a combination of both [31]. Scattering is the process of redirection of incident light due to the interaction of photons with constituent particles of the medium [31, 32]. The particles in a bulk medium or elements of a rough surface that scatter light are called scatterers. Examples of disordered media are clouds, snow, tissue, paper, foam, paint, etc. The color of a medium is determined by the wavelength that gets scattered from it (others being absorbed or directly transmitted). If visible light scatters from the medium, in absence of absorption, that medium appears white. For example, a widely studied material is nanoparticles of the wide band gap semiconductor zinc oxide (ZnO). Due to its high scattering and UV absorption properties, ZnO is used in many daily products such as sunscreen, cosmetics, food packaging, and paint. In a disordered medium, the density distribution of the constituent particles has no long-range order. When particles of disordered media are much smaller than the wavelength of light, the scattering is described by Rayleigh scattering. Scattering is classified into two main types, single and multiple scattering. In single scattering, the light wave is scattered only once before exiting the medium. Well-known examples of single scattering are reflection and refraction of light on an interface between two media.

When light scatters repeatedly inside the medium and the initial direction of light is completely lost, then it is called multiple scattering. As light propagates in a disordered medium by multiple scattering, there is no restriction to the propagation, or in other words, there is no energy gap for light in the medium. Hence light can freely travel in such a medium by taking random walks through it. In this case, the DOS is continuous at all frequencies inside the medium. The length scale for multiple scattering is defined by the transport mean-free path (ℓ), which is the average distance traveled by the photons before their direction of propagation gets completely randomized. The medium is in the multiple scattering regime when the thickness of the medium L is larger than ℓ, see Figure 1.1. Multiple scattering scrambles the initial polarization of light [6, 33, 34]. Therefore in experiments, detecting only the orthogonal polarized light with respect to input confirms detecting multiply scattered light and avoiding non-scattered or single scattered light.

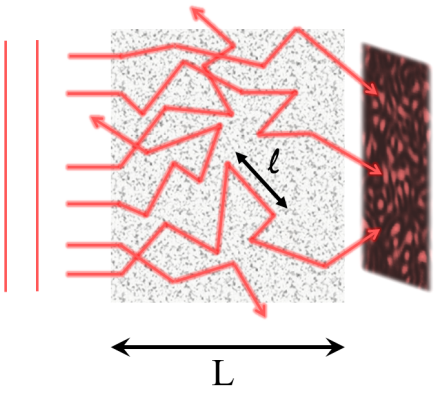

Figure 1.1: Multiple scattering of light in a medium where constituent nanoparticles are randomly placed. The incident light undergoes random walk through the sample, and produces an interference pattern, also known as speckle pattern at the exiting side. The transmission mean free path ℓ and the sample thickness L are indicated. Within ℓ, there are more than one scattering events.

Multiple scattering of light from a temporally coherent source such as a laser results in many random paths that light takes through the medium. Due to the difference in paths lengths, random phases are added to the various paths of light, causing constructive or destructive interference. The output is a combination of random intensity and phase, called a random phasor [35]. As a result, a random interference pattern is produced on the transmission side, reflection side, or any light exiting side of the sample. This interference pattern is known as the speckle pattern [36, 37], which is widely studied in the field of optics. Speckles are used in a broad range of applications, for instance, 3D imaging [38], sensing [39], microscopy [40, 41], cryptography [42, 43], and holography [44]. Isotropic scattering of high temporal coherent light produces 'fully developed' speckles that have the highest contrast (100%) between the intensity at constructive and destructive interference spots. The intensity I of such fully-developed speckles follows an exponential distribution given by

$$p_I(I) = \left(\frac{I}{\bar{I}}\right) e^{-I/\bar{I}}, \tag{1.1}$$

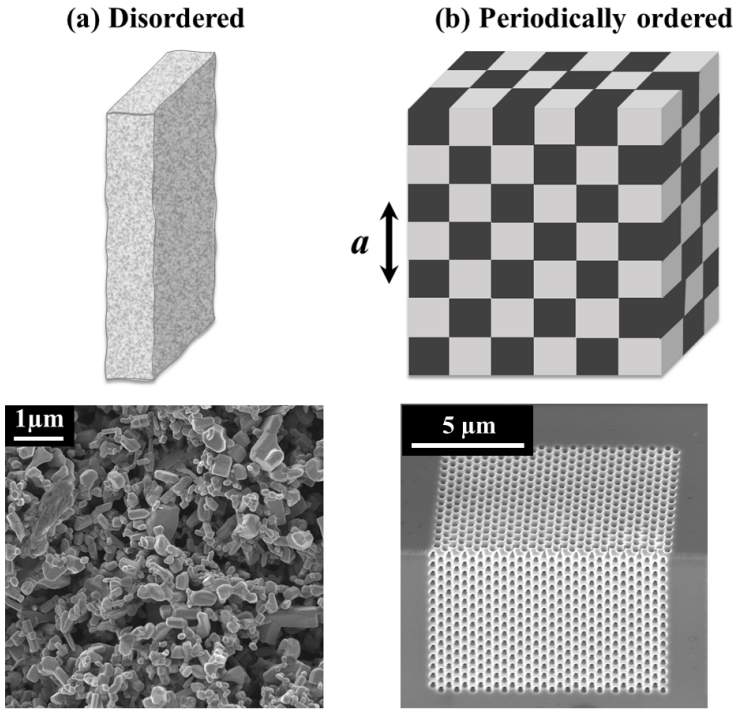

Figure 1.2: Examples of opaque media: (a) Disordered nanophotonic media where constituent particles are smaller than the light wavelength and are randomly located. Here scattering plays the dominant role. For example, a layer of ZnO nanoparticles as seen in the scanning electron microscopy (SEM) image at the bottom left figure (picture courtesy: M. Goodwin) (b) Periodic, ordered structures with a pitch or periodicity a comparable to the wavelength of light. Here Bragg diffraction is dominant and such structures have a photonic band gap. Bottom right: a 3D periodic structure made of Silicon fabricated in the MESA+ nanolab of the University of Twente (picture courtesy: C. Harteveld). The photonic crystal has the inverse woodpile design that consists of pores running along two perpendicular planes in crystalline silicon. Such crystals have a band gap in the NIR range.

Table 1.2: Interaction of light in various nanophotonic media

Arrangement	**Structure**	**Density of states**	**Wave propagation**
Random	Random assembly of nanoparticles	Continuous (no gap)	Multiple scattering, random walk
2D periodic	2D photonic crystal	2D gap	Bloch (outside gap), no Bloch (in gap) + random walk
3D periodic	3D photonic crystal	3D gap	Bloch (outside gap), no Bloch + random walk (in gap)
3D superperiodic	3D photonic crystal with superlattice of defects	3D gap + defect bands	Bloch (outside gap), no Bloch + light hopping (in gap) + random walk

where $\bar{I}$ is the mean intensity.
In **chapter 3**, we study intensity statistics of speckle patterns produced by a disordered medium at different wavelengths using our broadband tunable source, which helps us to characterize various features of the experimental setup that affects measurements, such as linewidth of the source and detector noise.

In the past decade, ever since its invention in our research group [45], the manipulation of light propagation in multiple scattering media has been boosted by the technique called wavefront shaping (WFS)[46–52]. Although conceptually related, WFS is different from adaptive optics [53] because it uses interference instead of ray optics to steer light to targets [54]. A scattering medium scrambles the plane phase front of the input wave, resulting in a speckle pattern of intensities at the output. In linear scattering, light transport is fully deterministic and can be described by the transmission matrix approach, which connects waves with incident field E_a to transmitted field E_b as [55]

$$E_b = \sum_a t_{ab} E_a, \tag{1.2}$$

where a and b label the modes of the incident and transmitted fields, respectively, and the elements t_{ab} of the transmission matrix that describes scattering in the sample. WFS solves the optimization problem by searching for the incident field that maximizes transmission from modes a into a desired output mode β

$$E_a = E_0 t^*_{\beta a}, \tag{1.3}$$

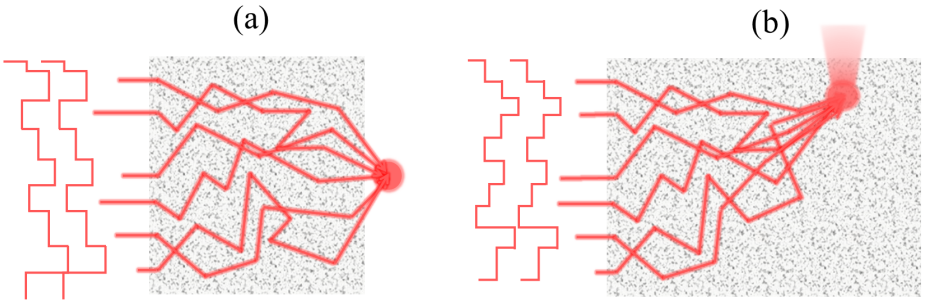

Figure 1.3: The spatial phases of the incident wavefronts are adjusted to obtain maximum intensity enhancement (a) behind a medium and (b) inside a medium. In the second case, the detection is done from the lateral direction to probe the energy density inside the medium through lateral scattered light.

where E_0 is a normalization constant to keep the incident power fixed. In phase-only WFS, the spatial phases of the incident coherent light beam are adjusted to get the desired output (for example, a focus) at the output, instead of a random speckle pattern. In experiments, a liquid crystal device called spatial light modulator (SLM) is used to adjust the phase front of the incident light. The output pattern can be outside or inside the medium, depending on the application (see Figure 1.3). Since the change of phase is dependent on the wavelength of light, the WFS optimized phase pattern is usually valid for a narrow bandwidth of wavelengths or frequencies. Within the limit of multiple scattering, we show in **chapter 4** that it is possible to tune the frequency bandwidth to a few tens of THz in the NIR range.

1.2.2 Periodic nanophotonic media

Manipulation of light in a whole new different way is achieved when a medium is designed to have a periodic variation of the refractive index of the order of wavelength ($a \approx \lambda$, where a is the periodicity). In this case, light waves reflect from the periodic planes. The simplest example of a periodic nanophotonic structure is a stack of alternating layers of high and low refractive index materials, known as a Bragg mirror [3, 27]. Light waves reflects partially at each layer boundary. When the wavelength of light is comparable to the optical thickness (or periodicity) of the layers, constructive interference of the reflected light takes place, thus resulting in a high-quality mirror for a specific wavelength range. The Bragg condition is fulfilled for the wavelengths λ along certain angles of the incident beam [56],

$$n\lambda = 2a \sin\theta \tag{1.4}$$

where n is the diffraction order, a is the pitch or lattice constant of the periodic planes and θ is the angle of incidence. The Bragg mirror is a periodic medium of

one dimension (1D), since the refractive index varies along 1D and uniform along the other two. In periodic nanophotonic structures of higher dimensions (2D or 3D), Bragg conditions are fulfilled along many different crystal plane orientations. Since the crystal planes have a pitch of the order of the wavelength of light, these structures are called photonic crystals [20].

Like other types of crystals, photonic crystals are described using reciprocal lattices, which is the Fourier transform of the real periodic lattice. In the reciprocal space (or k - space), the frequencies corresponding to the various directions of the wave vectors along the boundaries of the Brillouin zone are expressed in the *band structures*[57].

In a homogeneous medium, the relation of the frequency ω with the wave vector k defines the modes that lie along the *light line*, given by the product of velocity of light in the medium and the wave vector,

$$\omega(k) = ck. \tag{1.5}$$

The light lines in this case are continuous. When there is periodicity in the medium in real space, k is also repeated outside the Brillouin zone as $k + 2\pi/a = k$, where a is the periodicity or lattice constant of the medium. The crystal periodicity is described by a dominant reciprocal lattice vector $\mathbf{G}$. The light waves are Bragg diffracted, where incident light with a wave vector k_{in} is diffracted to outgoing light with a wave vector k_{out} by the reciprocal lattice vector such that

$$k_{\text{out}} - k_{\text{in}} = \mathbf{G}. \tag{1.6}$$

In this case, the light lines instead of being continuous, are folded back to the Brillouin zone when they reach the edges. Thus a photonic gap appears with a dimension depending on the dimensionality of the periodicity of the medium. For 3D structures, there are multiple directions of orientation of lattice planes that reflect light. The width of the gap is determined by the contrast of the refractive index between the two materials of the periodic structure. The directional energy gaps are called stop gaps that arise for the relevant incident wavevector. In 3D, when the stop gaps have a common overlap range for all wavevectors and all polarizations, the 3D nanostructure has a photonic band gap.

Outside the gap, both below and above, there are propagating modes called Bloch modes with Bloch wave vector $\mathbf{k}$ in the Brillouin zone [20, 57] ,

$$\mathbf{H}_{\mathbf{k}}(\mathbf{r}) = e^{i\mathbf{k}.\mathbf{r}}\mathbf{u}_{\mathbf{k}}(\mathbf{r}), \tag{1.7}$$

where $\mathbf{u}_{\mathbf{k}}(\mathbf{r})$ is a periodic function with property $\mathbf{u}_{\mathbf{k}}(\mathbf{r}) = \mathbf{u}_{\mathbf{k}}(\mathbf{r} + \mathbf{R})$ for all lattice vectors $\mathbf{R}$.

When light waves with frequency within the gap are incident on the crystal, no purely real wave vectors exist inside the crystal. In other words, the wave vector has complex character and there are no extended states. The modes are called evanescent modes, and the wave amplitudes decay exponentially as

$$\mathbf{H}(\mathbf{r}) = e^{i\mathbf{k}.\mathbf{r}}\mathbf{u}(\mathbf{r})e^{-\kappa.\mathbf{r}}, \tag{1.8}$$

with a complex wave vector $\mathbf{k}+i\kappa$. Within the gap, no light modes are allowed in the crystal due to multiple Bragg interference [58–61], hence the density of states (DOS) strictly vanishes. Within the band gap, light only enters to a limited depth called the *Bragg length* L_B, given by the length scale ($L_B = 1/\kappa$) of the exponent in equation (1.8).

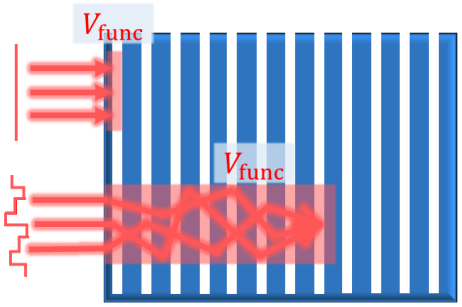

Figure 1.4: Illustration to define the functional volume of photonic crystals. For plane wave incidence, the light within the photonic gap enters to a limited depth defined by the Bragg length of the structure. In this case, the functional volume V_{func} is small, indicated by the red region. Making use of the multiply scattered waves in the crystal, light is steered much deeper into the crystal beyond the Bragg length, increasing V_{func}.

Since the local density of states (LDOS) [62, 63] also vanishes in a 3D photonic band gap, the 3D gap is a powerful tool to radically control spontaneous emission and cavity quantum electrodynamics (QED) of embedded quantum emitters [28, 64–66]. Applications of 3D photonic band gap crystals range from dielectric reflectors for antennae [67] and for efficient photovoltaic cells [68–70], via white light-emitting diodes [71], mode and polarization converter [72] to elaborate 3D waveguides [73, 74], for 3D photonic integrated circuits [75], to miniature lasers [76, 77] and to devices that control quantum noise for quantum measurement, amplification, and information processing [66, 78].

Photonic crystals are abundantly found in nature and also synthesized artificially for scientific research. Natural photonic crystals are found in opals, wings of butterflies, feathers of peacocks, and many other birds. Their vivid colors are because of the photonic gap of the constituent photonic structures being in the visible wavelengths. With improving nano fabrication techniques, it is now possible to synthesize photonic crystals compatible with desired wavelength range and of various materials in the laboratory. Here we study 2D and 3D photonic crystals that have the inverse woodpile design that consists of nanopores etched into crystalline silicon. The crystals are made of silicon with CMOS compatible methods, meaning the Silicon (backbone material) of the crystals are compatible with Silicon electronics, making the photonic crystals a good candidate for integrating into optoelectronic devices. In Figure 1.2(b) we show an exemplary 3D crystal that was fabricated by reactive ion etching. All the optical measurements of the crystals are done using near-IR light to avoid absorption because Silicon is almost transparent to these wavelengths. We give a detailed description of the fabricated samples and the NIR-compatible experimental setup to measure them optically in **chapter 2**.

When nanophotonic periodic media are fabricated, it is impossible to reach perfect periodicity without any roughness or deviations in sub-wavelength scale

[79]. Hence, all real samples that we study experimentally have their intrinsic structural disorder. Disorder in crystals also alters the properties of the crystal from the expected model. The identification of a complete three-dimensional (3D) photonic band gap in real crystals typically employs theoretical or numerical models that invoke idealized crystal structures. Such an approach is prone to false positives (gap wrongly assigned) or false negatives (gap missed). In experiments, since we deal with real crystals, fabrication deviations cannot be avoided and have to be accounted for. Therefore, we propose a purely experimental probe of the 3D photonic band gap that pertains to any class of photonic crystals. In **chapter 5** of this thesis, this issue is addressed and we present a purely experimental method to measure the full band gap of three-dimensional photonic crystals. This practical probe is model-free and provides fast feedback on the advanced nanofabrication needed for 3D photonic crystals and stimulates practical applications of band gaps.

Due to the forbidden gap, if a light-emitting device such as a quantum emitter is placed inside a photonic crystal, its emission is prohibited. The band gap provides excellent shielding of such functional devices in photonic crystal cavities from vacuum fluctuations of the electromagnetic field [80]. However, this makes it difficult to address such devices from outside due to the band gap. Thus the *functional volume* V_{func} of the crystal is limited to the volume which the Bragg length covers, which is usually very small, see Figure 1.4. The functional volume is the total useful volume of all functional light-matter interfaces (e.g., cavities) embedded within the crystal. This volume is ideally as large as possible, and should not be confused with the mode volume of a cavity that is typically as small as possible, see, *e.g.*, [81]. Hence, a control knob is needed to send light deeper into crystals that would facilitate increasing V_{func} and thereby accessing functional devices inside. For this case, we exploit the additional transport channels within the band gap created due to random scattering.

Structural disorder in crystals leads to multiple scattering, which results in additional transport channels even within the band gap. Hence, although ideally there should be no propagating modes within the gap, in real crystals there is also a small fraction of incoming light that gets into the structure and undergoes random walk by multiple scattering. This is where we combine WFS with periodic materials. In **chapter 6**, we show that multiply scattered light within the forbidden gap of a two-dimensional photonic crystal is steered to desired depths much deeper than the Bragg length by spatially shaping the wavefront of the incident light, thereby enlarging the functional volume (see cartoon illustration in Figure 1.4.

1.2.3 Superperiodic nanophotonic media

We have seen in section 1.2.2 that disruption in periodicity of photonic crystals leads to light transport within the band gap. Fabrication disorder is uncontrolled and hence usually not interesting and in fact, undesirable in crystals. All kinds of disorders that lead to scattering and hence transport of light are because of local variation of refractive index within the crystal. Addition of intentional defects

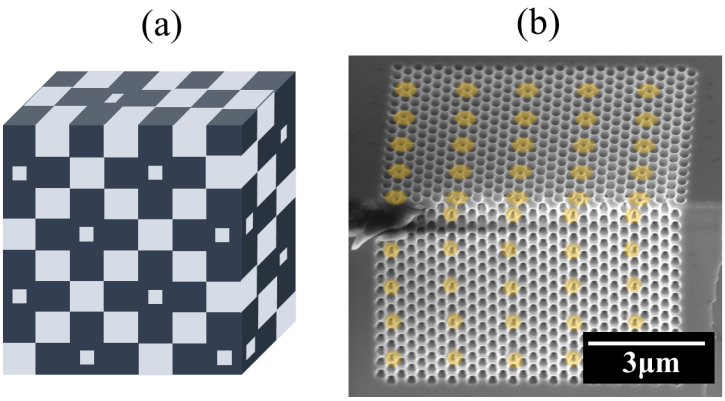

Figure 1.5: (a) An illustration of 3D superperiodic nanophotonic structure with periodically repeated intentional defects. In this case, the dark grey material is increased at specific points to have point defects in the structure. (b) A real 3D photonic crystal made of silicon with an array of point defects, also call superlattice (picture courtesy: C. Harteveld). The yellow highlighted areas indicate the location of defect pores that are smaller than the other pores. Inside the structure near the intersections of the smaller pores, a point defect is created as an excess of silicon.

in periodic media for controlling light propagation has been a widely studied area in photonics. The idea of fabricating defects into crystals is to disrupt the periodicity by increasing the amount of high index or low index material locally. For an illustration, see Figure 1.5.

Defects in photonic crystals may also permit *localized* modes to exist. If the frequencies of the modes lie within the photonic gap, then it exponentially decays into the surrounding crystal. In that case, the surrounding crystal works as a mirror to confine the modes in the defect area, making it a cavity for light. The confining can be in one, two, or three dimensions. For example, in Bragg mirrors (sometimes also called 1D photonic crystal), planar defects are created by changing the thickness of one or more layers, that act as 1D photonic cavities [82, 83]. In this case, the waves are confined in 1D and propagating along the other two. In 2D planar photonic crystals, line defects confine modes along one direction and sustain propagating modes along the other, resulting in efficient low-loss waveguides [84, 85]. Point defects in 2D crystals are used to make high quality factor cavities for trapping of light [86, 87], lasers [88–90], and coupled cavities [91]. Waveguiding in 3D photonic crystals have been also reported by creating line defects in the structures [74, 92].

In 3D, the concept of donor and acceptor modes within the band gap was first put forward by Yablonovitch *et al* [93]. Point defects in 3D photonic crystals are created by either removing or adding higher index material locally from the otherwise periodic structure. When the size and shape of the defects are optimally tuned, isolated bands appear within the photonic band gap that confines light in a small volume in the crystal, making it a cavity that confines light in all three

dimensions. In this thesis, we study light interaction with a 3D network of such 3D cavities buried in 3D band gap crystals.

If multiple cavities are placed in the vicinity of a cavity, the cavities 'talk to each other' as a result of evanescent-wave coupling. A simple case is when a 1D array of coupled cavities placed close to each other, an intricate waveguiding system appears known as CROW (coupled-resonator optical waveguide) [94]. Such systems have been studied as 1D coupled cavities in a 3D microwave photonic crystal [95] and 2D coupled cavities in 2D photonic crystal slabs [96]. Remarkably, 3D superlattices of optical coupled cavities that resonate inside a 3D band gap have not been studied to date. In 3D superlattices, cavities are periodically repeated with a longer lattice constant in the photonic crystal, thereby making the structure *superperiodic*. Recently, theoretical work in our research group has predicted the occurrence of intricate "Cartesian light" in superperiodic medium, wherein light propagates by hopping only in a few high symmetry directions in space with different coupling strengths [97]. Such propagation differs fundamentally from the conventional spatially-extended Bloch wave propagation outside the photonic gap[2]. In such photonic crystals with embedded cavities, the superlattice modes also exist within the band gap along with randomly scattered light due to disorder (in real crystals). The superlattice of cavities in the 3D band gap establishes a novel way of light propagation and represents the optical analog of the famous Anderson tight-binding Hamiltonian for spins or electrons. In **chapter 7**, we experimentally investigate the optical response of photonic crystals modified with a 3D array of resonating cavities (see Figure 1.5(b)).

[2]Cartesian light is also fundamentally different from higher order spatial Bloch modes [98, 99] and is not just a CROW in 3D [97]

Chapter 2

Samples and experimental setup

Here we describe the samples used in this thesis and explain the experimental setup. The main samples studied here are 3D periodic nanophotonic metamaterials, known as photonic band gap crystals. Photonic crystals consist of periodically stacked high and low refractive index materials with a spatial periodicity in the order of the wavelength of light. The photonic crystals that we study are made of silicon with CMOS-compatible methods, and thus are also good candidates for optoelectronics in the telecommunication industry. The photonic band gap of the crystals covers the near-infrared (NIR) frequencies, including the telecom ranges. Therefore, we build a compatible optical setup that operates in the NIR frequencies to perform spectroscopy and wavefront shaping on silicon photonic crystals and other photonic materials.

2.1 Silicon samples

The basic design of the photonic crystals goes by having deep nanopores periodically in a high-index material, in our case, silicon. The crystals are fabricated by etching pores into crystalline silicon using CMOS-compatible methods [100, 101]. We employed deep reactive ion etching through an etch mask that was fabricated on silicon beams [102]. Below we discuss the two types of inverse woodpile photonic crystals based on the dimension along which the refractive index varies periodically, *viz.*, two-dimensional (2D) and three-dimensional (3D) that are studied here.

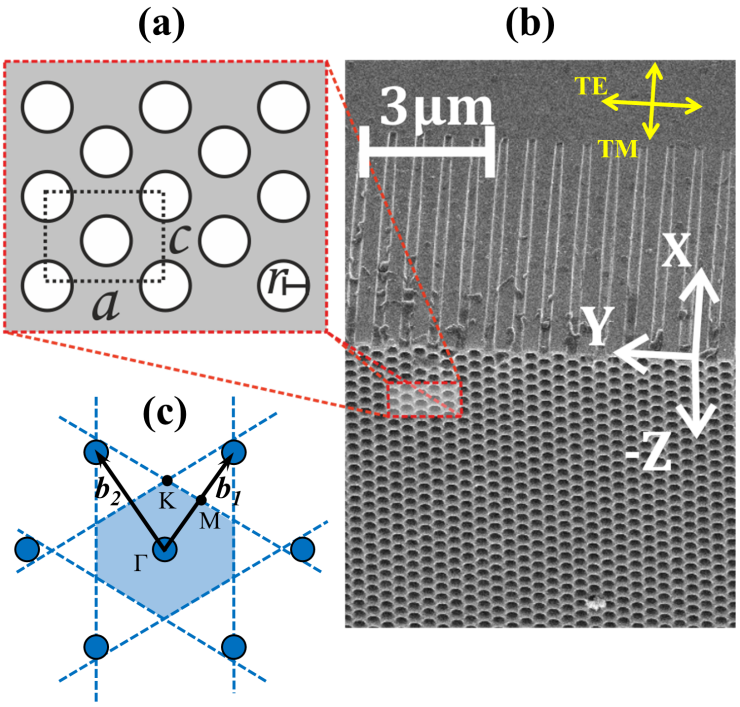

Figure 2.1: (a) YZ-plane with the centered rectangular crystal with lattice parameters $a = 695$ nm and $c = a/\sqrt{2}$. (b) Scanning electron microscopy (SEM) image of a fabricated 2D inverse woodpile photonic crystal made of silicon. The lower half shows the 2D array of pores in the YZ-plane, and the upper half shows the XY cleavage plane with 6 μm deep pores (see 3 μm scale bar). Figure courtesy of C. Harteveld. On the top right, the polarization orientation TE and TM are shown of the incoming E-field along $-Z$ direction, used for measurements. The pores have a diameter $2r = 290$ nm (or $r/a = 0.21$). (c) The reciprocal space of the centered rectangular lattice (blue circles). The filled area is the first Brillouin zone, b_1 and b_2 are the primitive lattice vectors. The relevant high symmetry points Γ, K, and M are shown.

2.1.1 2D photonic crystals

The 2D photonic crystals consist of large periodic arrays of nanopores etched in a silicon wafer [100, 103], see Figure 2.1. The 2D array of pores has a centered-rectangular structure with lattice constants a and c in a ratio $a/c = \sqrt{2}$, as depicted in Figure 2.1. As the periodic variation of the refractive index is in two dimensions in space, namely Y and Z, these samples are called 2D photonic crystals. A hard mask, made by UV-lithography is defined on a silicon wafer on the YZ-plane with a centered rectangular array of circular holes, with a radius to pitch ratio $r/a = 0.21$, see Figure 2.1(a). Then deep reactive ion etching is applied along the X-direction to fabricate nanopores, as described in detail previously [101]. The lateral YZ-extent of the 2D crystal is 10×10 mm^2 at the

center of the wafer. After etching the pores, the wafer is cleaved along the crystal plane to expose the XY surface for optical experiments. Since the crystals are carefully cleaved along a high-symmetry crystal plane of the underlying Si crystal, no further polishing is required.

The Brillouin zone in the reciprocal lattice (shown in blue filled circles) of the crystal is drawn in Figure 2.1(c), showing the relevant high-symmetry points Γ, K, and M. In optical measurements of the 2D crystals in this thesis, the incident light is probed along the $-Z$-direction that corresponds to the ΓK direction of the wave vector. When linearly polarized incident light is used, if the E-field oscillates along the Y-direction, *i.e.*, perpendicular to the length of the pores, the polarization state is called transverse electric (TE) and when the oscillation is along the x-direction, *i.e.*, parallel to the length of the pores, the polarization state is called transverse magnetic (TM).

2.1.2 3D photonic crystals

The 3D photonic crystals studied in this thesis have the inverse woodpile structure that consists of two identical arrays of pores with radius r running orthogonal in the X- and Z-directions. This design is similar to the woodpile structure [105], but for an inversion of the refractive index profile. On each plane (*i.e.*, xy or yz), the array of pores has a centered-rectangular structure with lattice constants a and c with the ratio $a/c = \sqrt{2}$. The resultant 3D crystal structure is cubic with a diamond-like symmetry, as illustrated in Figure 2.2(a) and also in an animation [106]. Inverse woodpile crystals have a broad 3D photonic band gap (see Figure 2.3) on account of their diamond-like structure [107–110]. The inset of Figure 2.3 shows the first Brillouin zone of the inverse woodpile structure with the high-symmetry points identified and the origin at Γ. The ΓX and ΓZ correspond to waves propagating along each set of nanopores. The band gap has a maximum relative bandwidth of 25.4% for a reduced pore radius $r/a = 0.245$ at a relative permittivity $\epsilon_{\mathrm{Si}} = 11.68$, typical of a silicon high-index backbone [107, 109].

For the 3D crystals, the etch mask was fabricated by depositing chromium on the surfaces followed by focused ion beam milling in a single step on both perpendicular faces of the edge of the silicon wafer as explained in Ref. [112]. The nanopore etching is carried out in two steps on each face independently using inductively coupled plasma-reactive ion etching. More details on the fabrication process can be found in Refs. [112, 113]. The two perpendicular sets of pores have a shift of one pore radius along the Y-axis so that each pore overlaps its perpendicular counterpart through half diameter inside the bulk of the crystal. A number of crystals with different design pore radii r_d at a fixed lattice parameter $a = 680$ nm were fabricated on multiple silicon beams. Figure 2.2 shows a scanning electron microscopy (SEM) image of one of our crystals with a designed pore radius $r_d = 160$ nm ($r_d/a = 0.235$). The dimensions of each crystal are typically $8 \times 10 \times 8$ $\mu\mathrm{m}^3$. Figure 2.2 shows that the sample geometry allows for good optical access to the XY and YZ crystal surfaces. For 3D crystals, we use the notation s and p to define the polarization state of light. In this case, s-polarized light is perpendicular to the X-directed pores while p-polarized light

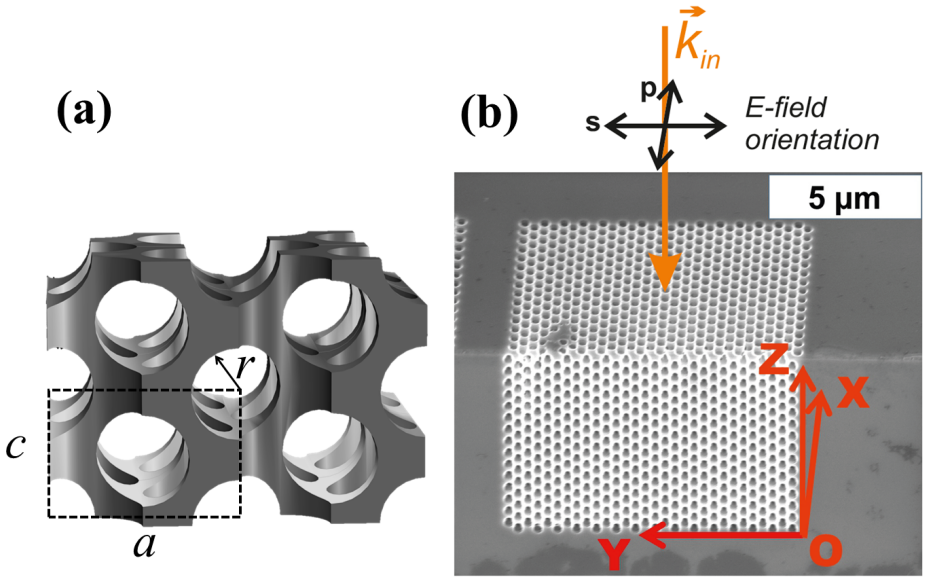

Figure 2.2: (a) Schematic illustration of a $2 \times 2 \times 2$ supercell of a 3D inverse woodpile photonic crystal, image from Ref. [104]. The two sets of pores are parallel to the X and Z-directions, while the lattice constants along X, Y, and Z are c, a, and c, respectively, with the ratio $a/c = sqrt2$. (b)Scanning electron microscopy (SEM) image of the edge of the silicon beam PG-EBAR-18072017-CH-6C (in short, 6C) with a cubic 3D inverse woodpile crystal in perspective view. The crystal consists of two sets of perpendicular pores along the X and Z directions with design radius $r_d = 160$ nm. The crystal has lattice parameters $a = 680$ nm in the Y-direction and c in the X and Z-directions with $c = a/\sqrt{2}$. Figure courtesy of C. Harteveld. The incoming direction of the wave vector $\mathbf{k}_in$ used in the measurements is shown on the top with the polarization directions s and p (equivalent of TE and TE polarization respectively for 2D crystals) of the E-field.

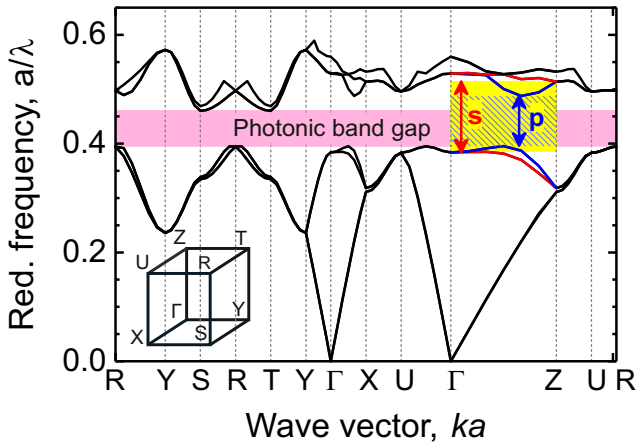

Figure 2.3: Band structures calculated for an infinite inverse woodpile photonic crystal with $r/a = 0.19$ and relative permittivity $\varepsilon_{Si} = 11.68$. The abscissa is the wave vector in the first Brillouin zone (see inset). The experimentally relevant ΓZ high-symmetry direction is enlarged for clarity. The ΓZ stop gaps for s and p-polarized light are indicated by the yellow and hatched bars, respectively. The p-polarized bands are shown in blue and s bands in red [111]. The pink bar is the 3D photonic band gap. Band structure calculated by R. Nair.

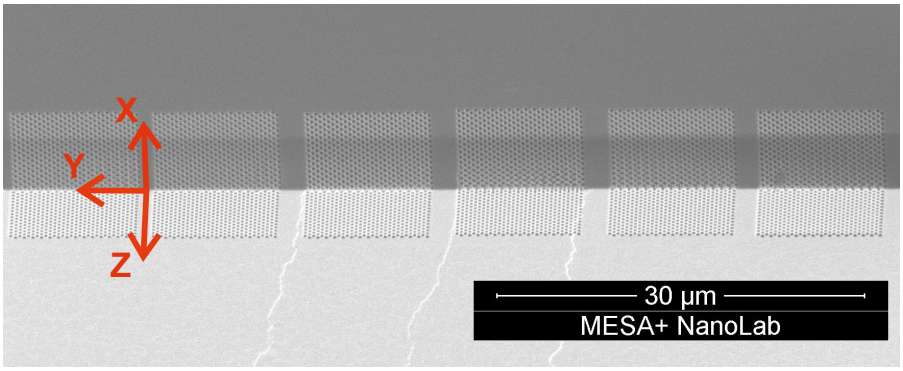

Figure 2.4: An array of fabricated 3D inverse woodpile photonic crystals on the edge of the silicon beam PG-EBAR-18072017-CH-6C. Figure courtesy of C. Harteveld.

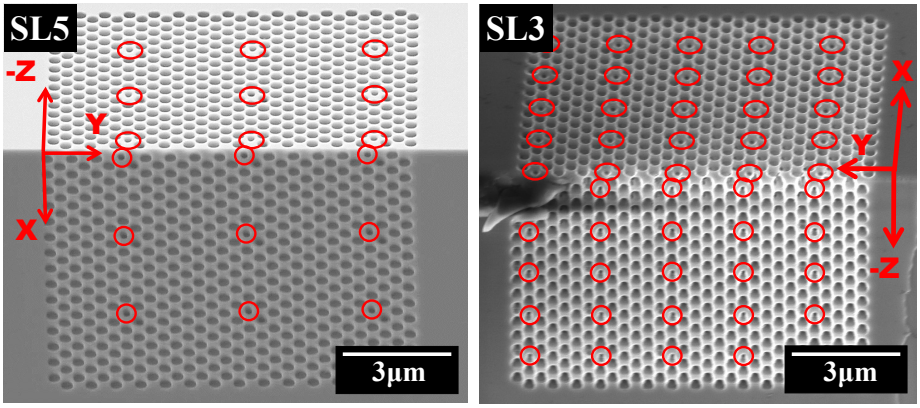

Figure 2.5: SEM images of two 3D inverse woodpile photonic crystals with a 3D superlattice, SL5 and SL3, viewed in the (X,Z)-direction. They are fabricated in the silicon beam PG-EBAR-18072017-CH-6C, together with the other crystals shown in Figure 2.4. The designed pore radius is $r = 0.16$ μm for the main nanopores and $r' = r/2 = 0.08$ μm for the defect pores. The defect pores are positioned every 5th lattice constant in SL5 and every 3rd lattice constant in SL3. The excess silicon at the intersections of these defect pores inside the material form point defects which constitute the superlattice of 3D cavities. The superlattice of the point defects has the unit cell with dimensions $5c, 5a, 5c$ in SL5 and $3c, 3a, 3c$ in SL3. Figure courtesy of C. Harteveld.

is parallel to the X-directed pores. A zoom-out view of an array of fabricated 3D crystals on the edge of a silicon beam is shown in Figure 2.4.

2.1.3 3D photonic crystals with cavities

We study 3D inverse woodpile photonic band gap crystals with periodically repeated point defects that form 3D superlattices of cavities. Such structures are called superperiodic, due to the presence of more than one periodicity within the same structure. As mentioned in the previous section, inverse woodpile crystals have a broad and robust 3D photonic band gap, which is optimal to confine embedded optical cavities and shield them from the surrounding vacuum [80, 114].

To realize a 3D cavity in an inverse woodpile structure, we design two proximal and perpendicular "defect" nanopores to have smaller radii r' [115]. Near the intersection of the two defect pores, the excess high index backbone creates a donor-like cavity. When the radii of the pair of defect pores are tuned to $r' = r/2$, light is maximally confined inside the cavity [115]. When multiple cavities are repeated periodically in the crystal, coupling between the cavities results in a 3D cavity superlattice that sustains 'Cartesian light' [97], which will be explained in detail in chapter 5. In presence of cavities, additional states are created inside the original band gap of the underlying 3D band gap crystal. Figure 2.5 shows

scanning electron microscopy (SEM) images of two fabricated inverse woodpile crystals, each with an array of defects with different spacing between the defect pores. In the first crystal on the left of Figure 2.5, the defect pores are situated every five lattice constants apart. Hence the lattice parameters of the superlattice are $a_{\mathrm{SL}} = 5a$ along Y and $c_{\mathrm{SL}} = 5c$ along X and Z directions. There are $3 \times 3 = 9$ defect pores on each crystal surface, hence there are up to $3 \times 9 = 27$ pore crossings and thus cavities inside the superlattice. The second crystal on the right of Figure 2.5 a superlattice with cavities repeated every three lattice constants apart, *i.e.*, superlattice constants $a_{\mathrm{SL}} = 3a$ and $c_{\mathrm{SL}} = 3c$ with up to $5 \times 5 \times 5 = 125$ number of cavities. For convenience, we will call the first crystal SL5 (referring to five lattice spacings between neighboring cavities) and the latter SL3 (referring to three lattice spacings between neighboring cavities).

2.2 Experimental setup

We have developed a versatile near-infrared setup to collect position-resolved broadband reflectivity and lateral scattering spectra of photonic nanostructures, as well as to perform wavefront shaping to focus light inside samples. All measurements are processed in LabView environments. The near-infrared range of operation is compatible with 3D silicon nanophotonics as it avoids intrinsic silicon absorption. A pictorial representation of the full optical setup is shown in Figure 2.6. The setup consists of three main components:

1. a broadband tunable coherent source,
2. a broadband wavefront shaper, and
3. twin-arm imaging of reflected and lateral (YZ-plane) scattered signals from the sample.

The broadband tunable coherent source is realized by spectrally filtering the emission from a supercontinuum source (Fianium SC 450-4, 450 - 2400 nm) using a monochromator (Oriel MS257; 1200 lines/mm grating). A long-pass filter (cut-off wavelength: 850 nm) is used to reject the background from second-order diffraction of shorter wavelengths. The filter is slightly tilted so that the reflected light from the supercontinuum source does not go back into the collimator[1], but gets absorbed in a beam dump as shown in the figure. The filtered light is sent through a reflecting beam expander and then to a parabolic mirror (PM) that focuses the light to fit through the input slit of the monochromator. The monochromator scans optical frequencies ranging from 4700 to 11000 cm^{-1} (or wavelengths $900 < \lambda < 2120$ nm) with a linewidth of 0.6 ± 0.1 nm exiting from the output slit of size 50 μm (see Figure 2.7) and a tuning precision better than 0.2 nm. Since we use this setup also for wavefront shaping, we use sequential scanning of wavelengths instead of measuring the spectrum at once with a spectrometer as in [116–118]. A He:Ne laser is used to calibrate the grating of the

[1]When back-reflected, stray light could lead to unwanted feedback and damage of the source

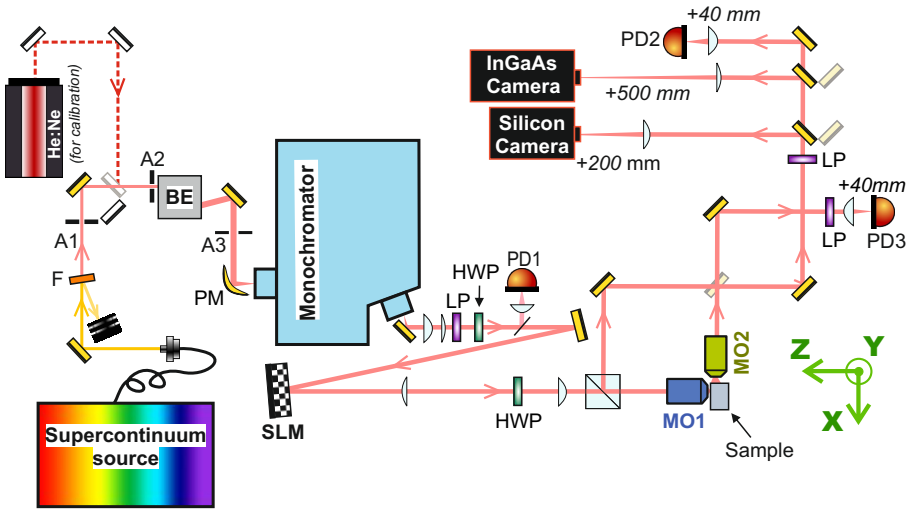

Figure 2.6: Optical setup to measure position-resolved microscopic broadband reflectivity, lateral scattering and wavefront shaping. The Fianium SC is the broadband supercontinuum source, the long-pass glass filter F blocks the visible light at $\lambda < 850$ nm, the BE is a reflective beam expander. The monochromator filters the light to a narrow band with linewidth of about 0.7 nm. HWP are half-wave plates and LP's are linear polarizers. The SLM is a spatial light modulator that is used for wavefront shaping and also for correcting the direction of incoming light onto the sample. Incident light is focused on the sample with a 100× objective MO1 that also collects the reflected light; the other objective MO2 collects the scattered light from the sample in the lateral direction and sends for detection. The NIR camera (InGaAs) views the sample in reflection with an effective magnification of 250×. The other Silicon camera can also be used to view the sample when using shorter wavelengths. The photodiode PD1 monitors the incident light power, and PD2 and PD3 measure reflected and scattered signals from the crystal, respectively.

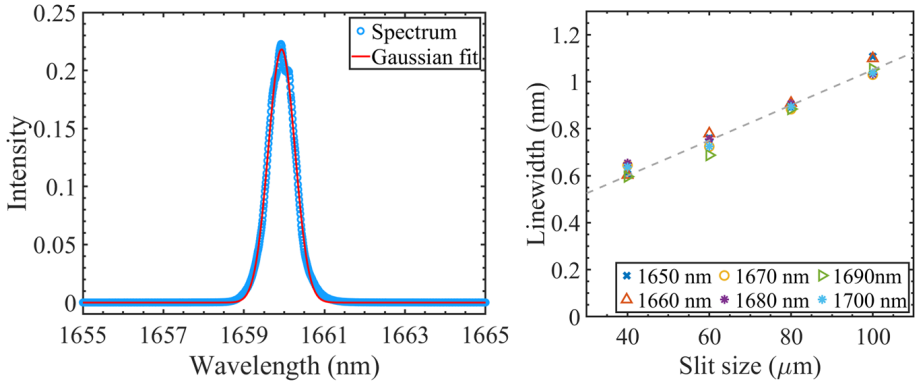

Figure 2.7: Left: The output spectrum of the monochromator for one single wavelength (1660 nm) measured by a spectrometer. The linewidth is estimated by fitting a Gaussian to the data points and finding the FWHM. In this case, the linewidth at $\lambda_c = 1660$ nm or $\omega_c = 6024$ cm^{-1} is 0.78 nm, or $\delta\omega = 2.83$ cm^{-1}. Here the slit width of the monochromator was set at 60 μm. For all our experiments, the slit width was set at 50 μm. Right: The linewidth of the source versus slit width of the monochromator output at 6 different wavelengths. The linewidth increases linearly as slit width is increased.

monochromator, and not used for measurements. The filtered light is then collimated and expanded to a beam diameter of 7.5 mm. A small fraction (8%) of the light is sent to a photodiode PD1 using a glass plate as a reference to monitor the input power. The rest of the light beam is then incident on a reflective phase-only spatial light modulator (Meadowlark optics; 1920×1152 pixels; AR coated: $850 - 1650$ nm). Since the output of the source is randomly polarized, a linear polarizer (LP) followed by a half-wave plate (HWP) are placed at the monochromator output to select the desired linear polarization orientation, since the polarization has to be parallel to the slow axis (in this case the Y-axis of the SLM) for the SLM to optimally function. At this point, the setup is described in detail first from the point of view of spectroscopy and next wavefront shaping.

2.2.1 Near-infrared reflectivity and lateral scattering

In the optical setup shown in Figure 2.6, the sample is mounted on an XYZ translation stage that has a step size of about 30 nm. The reflected light from the SLM [2] is sent to an infrared apochromatic objective (Olympus LC Plan N 100×) to focus the light onto the sample's surface with a numerical aperture NA = 0.85. The beam waist of the light reflected from the SLM is narrowed and re-collimated by a pair of lenses so that it fits the back aperture of the

[2] For spectral measurements the SLM is used to reflect as a mirror. In addition, the SLM is also used to correct a tilted beam in the setup as explained in the Appendix of this chapter.

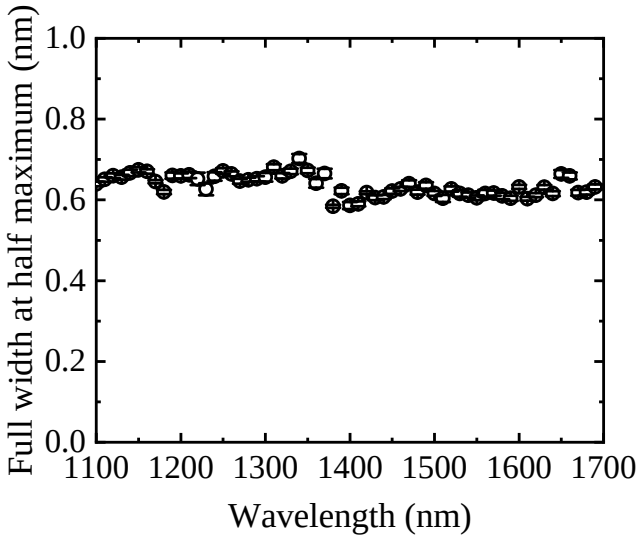

Figure 2.8: The linewidth of the source is constant near 0.6 nm at a slit width 50 μm that is used for all the measurements.

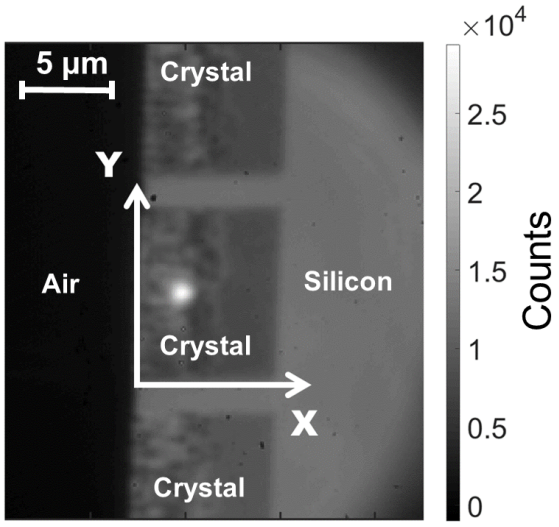

Figure 2.9: Image XY-surface of 3D crystals on the edge of a Si beam, captured by the InGaAs camera, with 250× magnification. The surface is illuminated by an NIR LED at 950 nm, where the rectangular darker areas are the photonic crystals. The bright spot on the middle crystal is the focus of incident light from the tunable source.

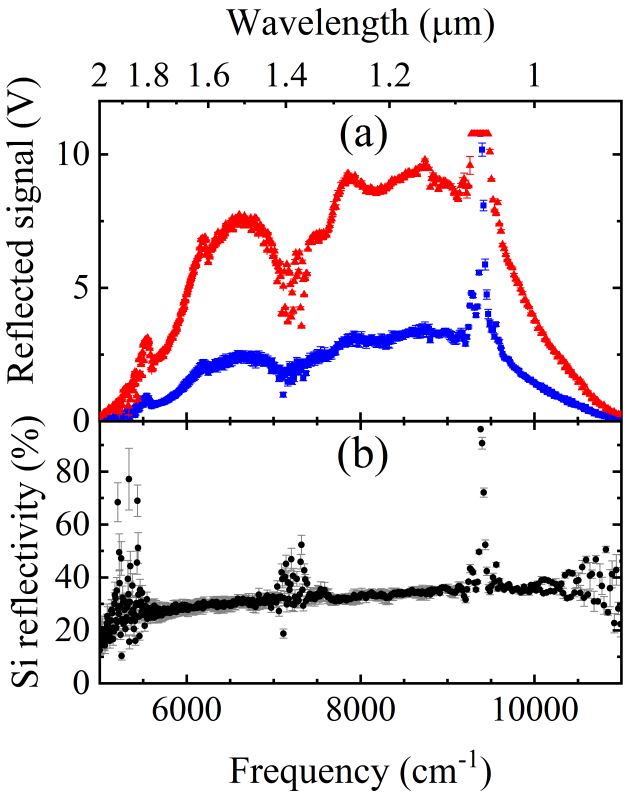

Figure 2.10: (a) The raw spectrum recorded by the photodiode PD2 of the reflected light from a gold mirror (red triangles) and clean silicon substrate next to the photonic crystals (blue squares). Due to the very high power near the pump frequency 9400 cm^{-1} of the supercontinuum source, the intensity is usually saturated, which is not considered to interpret measurement data. (b) The bulk Si reflectivity normalized to the gold reflectivity reference.

objective. The diffraction limit in the setup is about 1 μm at longer wavelengths. A second HWP is introduced on the beam path before the objective to rotate the linear polarization of the incident light on the sample for polarization-dependent measurements.

Light reflected by the sample is collected by the same objective and a beam splitter directs the reflected light towards the detection arm where the reflection from the sample is imaged onto an IR camera (Photonic Science InGaAs). In order to locate the focus of the input light on the surface, a NIR LED is used to illuminate the sample surface. We use the XYZ translation stage to move the sample to focus the light on the desired location. For example, an image of a 3D crystal as seen on the IR camera (see Figure 2.9) reveals the XY surface of the Si beam. The bright circular spot with a diameter of about 2 μm is the focus of light reflected from the crystal. The rectangular darker areas of about 8 μm $\times$10

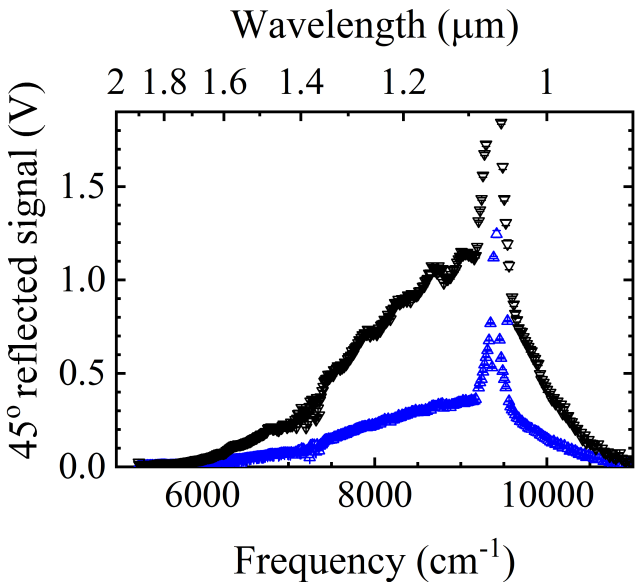

Figure 2.11: The raw spectra recorded by the photodiode PD3 of the reflected light at 45 deg incident from a Silicon surface for *s*-polarized (black down triangles) and *p*-polarized (blue up triangles) light.

μm are the XY surfaces of the 3D photonic crystals. They appear dark compared to the surrounding silicon since the LED illumination is outside the band gap of these crystals whose effective refractive index is less than that of silicon.

Once the input light beam is focused on the sample, the reflected light is sent to photodiode PD2 (Thorlabs InGaAs DET10D/M, 900 nm - 2600 nm) by flipping out the mirror in front of the camera. The photodiode records the reflected intensity I_R as the monochromator scans the selected wavelength range. At the same time, the scattered light from the sample in the lateral direction is collected by a long working distance apochromatic objective MO2 (NA = 0.42), and sent to a third photodiode PD3 (similar to PD2). An analyzer in front of each photodiode is used to select either parallel or cross polarization of the reflected and scattered light with respect to the input. Thus, in total we get two sets of spectra as signal every time the wavelengths are scanned through the desired range: a reflectivity spectrum, and a lateral scattering spectrum.

The raw reflectivity measured on two reference samples *viz.* the clean gold mirror and the bulk silicon substrate are shown in figure 2.10(a). The reference spectra show that the intensity of the supercontinuum source is not uniform. The intensity cut-off at high frequencies is due to limited detection bandwidth of the photodiode and that at the low frequencies is primarily due to the use of refractive optics in the setup (e.g. lenses, objectives, wave plates). There are noisy data points in the middle of all the spectra near 1400 nm wavelength that is attributed to possible water vapor absorption that could vary from day-to-day depending

on the lab conditions. This noise could potentially be suppressed in future experiments by creating a dry-air or nitrogen purge box around the sample. Hence one must be very careful while analyzing data in this wavelength range. The high-intensity peak at 1064 nm is the pump wavelength of the supercontinuum source. A typical measurement of the reflectivity or lateral scattering spectrum takes about 5 to 25 minutes to record depending on the chosen wavelength step size (typically 10 nm or 2 nm). The calibrated reflectivity and lateral scattering are defined as

$$R \equiv I_R / I_{0R} \tag{2.1}$$

$$LS \equiv I_{LS} / I_{0LS} \tag{2.2}$$

For reflectivity, the spectral response I_R of the samples is referenced to the reflected signal I_{0R} from a clean gold mirror that reflects 96%. Since it is tedious to dismount and realign the sample to take reference spectra during long measurements on crystals on a silicon beam, we also take secondary reference measurements on bulk silicon outside the crystals, which has a flat response $R \approx 31\%$ with respect to the gold mirror. The bulk silicon reflectivity is plotted in figure 2.10(b) that agrees with the expected $\approx 31\%$ reflectivity of Si for normal incidence in NIR. The spectrum is flat[3] without any features other than the noisy data points described above. Therefore, we use the Si signal also as a reference for reflectivity measurements.

The reference for lateral scattering is a bit tricky since we need to have the input signal go through the objective MO2 for correct referencing. Therefore we used the edge of a silicon beam that was cut at 45° to reflect the incoming light coming through MO1 towards MO2 and send it to PD3, just like the lateral scattering signal. Using Fresnel reflectivity of 45° incident light on silicon, we use a calibration of $R_p = 43\%$ reflectivity for s-polarized light and $R_p = 19\%$ reflectivity for p-polarized light. To ensure that the signal to noise ratio of the photodiode response is sufficient to detect signal in the desired range, each detector photodiodes are fed into a lock-in amplifier to amplify the signal with a suitable gain. Since a serial measurement mode holds the risk of possible temporal variations in the supercontinuum source, we simultaneously collect the output of the monochromator with photodiode PD1 in each reflectivity scan. An example of reference spectra for LS measurements is shown in figure 2.11 for two orthogonal polarizations of the incident light.

2.2.2 Near-infrared wavefront shaping

The setup is also designed to do wavefront shaping (WFS) to focus light inside nanostructures. We perform phase-only WFS using the spatial light modulator (SLM) mentioned in the previous section. In addition to traditional WFS where scattered light is imaged on the transmission side, in this setup the imaging and WFS is also done from the side of the sample. This facilitates controlled focusing

[3] The Si reflectivity spectrum has a small positive slope with frequency since we do not consider the change of refractive index with frequency within this range.

of light at different depths of the sample. Also, it is beneficial for photonic crystals where transmission measurement is not easy due to the bulky silicon substrate behind the crystals (see Figure 2.4).

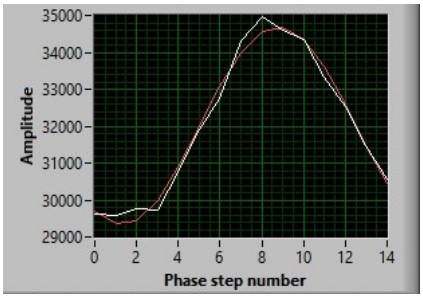

Figure 2.12: A plot of target intensity in camera as phase of one super-pixel of the SLM is changed from 0 to 2π to find the optimum phase value to assign to that pixel. The white line goes through the data points while the red curve is the cosine fit.

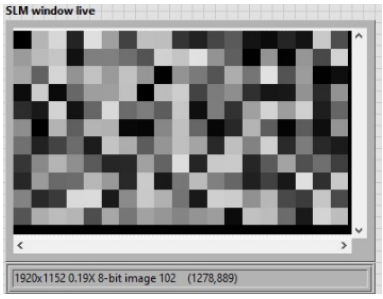

Figure 2.13: An example phase pattern on the SLM during an optimization. Each super-pixel contains 100×100 pixels and there are $N = 209$ super-pixels. The gray values from black to white corresponds to phases from 0 to 2π.

The light from the SLM is imaged to the back focal plane of the large numerical aperture (NA = 0.85) infrared apochromatic objective MO1. Then, the transmitted (as in chapter 4) or the laterally scattered light (as in chapter 6) from the sample is collected using a long working distance apochromatic objective MO2 (NA = 0.42). Light collected by MO2 is then imaged on the InGaAs camera. In the case of WFS in laterally scattered light, the side view of the sample is imaged on the camera where the target spot of a few pixels is chosen at a desired depth from the surface. Then, using the camera intensity counts at the target spot as the feedback, the phase of each pixel is changed from 0 to 2π (translated to corresponding gray values) in 8 steps, sufficient to get a good cosine fit for the amplitude versus phase. Using a higher number of phase steps is not required as the algorithm fits only a three-parameter function ($A\cos(\phi + \phi_0) + C$) to extract ϕ_0. For proper calibration, the target intensity is normalized by the signal in the reference photodiode PD1. Then, a cosine curve is fitted to the target intensity variation with phase to estimate the phase of the corresponding pixel that generates the highest intensity on the target. An example of this process as it takes place during the optimization is shown in figure 2.12. Then the SLM pixel is assigned the phase value corresponding to maximum target intensity and the procedure is iterated for every pixel in the chosen area of the SLM. Thus, during the optimization, the intensity at the target gradually increases. After the optimization, the desired focus is obtained for the selected frequency of light. A typical optimization procedure per pixel of the SLM takes about 1 to 2 seconds that is determined by the number of phase steps, the integration time of the camera, and 10 Hz refresh rate of the SLM. Thus the total optimization takes

time equal to this number times the total number of superpixels.

Usually, instead of assigning a phase value to each and every pixel of the SLM (total 1920×1152 pixels), neighboring pixels are merged to form so called super-pixels, which are assigned collectively the same phase value. Total area of the super-pixels on the SLM is conserved, which means increasing the size of super-pixels decreases their total number N. The enhancement of intensity on the target scales with the number of segments N for the optimized case compared to averaged non-optimized random wavefronts as [55]

$$\eta = \frac{\pi}{4}(N-1) + 1, \tag{2.3}$$

assuming all segments of the selected SLM area have equal contribution to the total intensity. However, in experimental situations, it is not always the case. In our setup, the incident beam has a Gaussian-like profile. When the beam is aligned to the center of the SLM, the pixels near the center have more contribution to the target intensity compared to those near the edges. Another factor that decreases the expected enhancement in our setup is that 100% of the reflected light from the SLM does not reach the sample. In our setup, the incident beam fills the whole SLM screen and therefore the reflected beam from SLM has a rectangular shape similar to the rectangular SLM display. Since we fill the circular aperture of the focusing objective with a rectangular-shaped beam, automatically part of the long side of the beam gets clipped. Therefore, more pixels near the short edges of the SLM do not contribute to WFS optimization. Therefore, to compute enhancement precisely, the contributing area on the SLM needs to be identified.

The time required for a full optimization collectively depends on the following factors:

- The size of the super-pixels: using larger super-pixels reduces the number of optimization steps.
- Illumination area on the SLM screen: The beam diameter of the light illuminating the SLM was chosen to match the pupil diameter of the objective MO1 in order to realize a diffraction-limited focus on the sample. As the laser beam is Gaussian, we select a circular region on the SLM (diameter = $2\times$ pupil diameter = 6.2 mm) for defining the super-pixels. This helps decrease the runtime of the WFS algorithm in comparison to using the whole SLM screen (19 mm $\times$ 10 mm).
- A suitable integration time that ensures good signal to noise ratio for WFS optimization is chosen (typically on the order of a few hundred milliseconds per exposure).

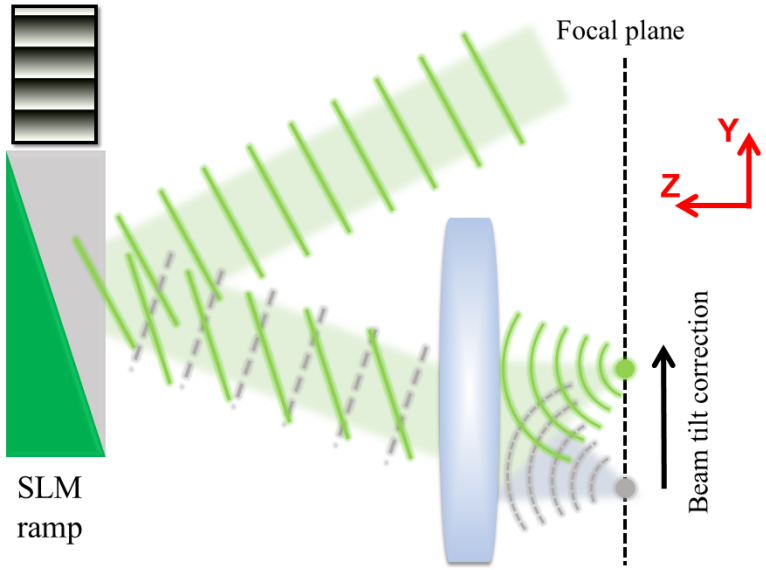

Figure 2.14: Side view of the beam tilt correction system in the optical setup. A ramp pattern is introduced to the SLM for each wavelength that results in tilting the plane phase of the reflected beam and as a result, the focus is shifted to the desired (green) spot on the focal plane. Without correction, the beam is focused on the grey dot below the target spot. On the top left, a phase pattern displayed by the SLM (front view) to correct beam position for wavelength 1550 nm is shown. In the phase pattern, black corresponds to 0 and white corresponds to 2π phase values.

Appendix 2

2.A Correction of beam tilt using SLM

The rotation stage of the grating of the monochromator has a very small, non-adjustable tilt with respect to the horizon. Therefore, when wavelengths are scanned across a broad range by rotating the stage, after approximately 2.65 meters of the beam path and multiple mirror reflections until it reaches the sample, the beam shifts significantly (over 11 μm on the focal plane) in the Y direction (gray dot in Figure 2.14). This is very undesirable since we work with inhomogeneous samples whose dimensions are less than the beam shift. To correct for the beam shift so that at each wavelength the location of the focus is exactly the same on the sample surface, a phase ramp pattern is written on the SLM. For reference, we selected a wavelength (1375 nm) near the center of the range of used wavelengths as the central wavelength, which means, this wavelength is aligned without using a ramp pattern on the SLM. We call the location of the focus on the camera at 1375 nm without a correction pattern as the central spot

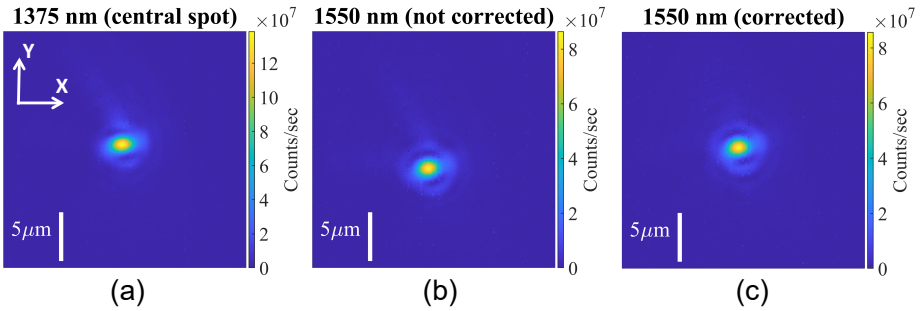

Figure 2.15: The process of correction of beam tilt using SLM phase ramp. Image of reflected beam when light is focused on a gold mirror for three different situations of input wavelength and pattern on the SLM: (a) at 1375 nm, with a flat phase pattern on SLM (central spot) (b) at 1550 nm, flat phase pattern on SLM (focus moves downward) (c) at 1550 nm, optimized ramp pattern on SLM (the focus is sent back to the central spot).

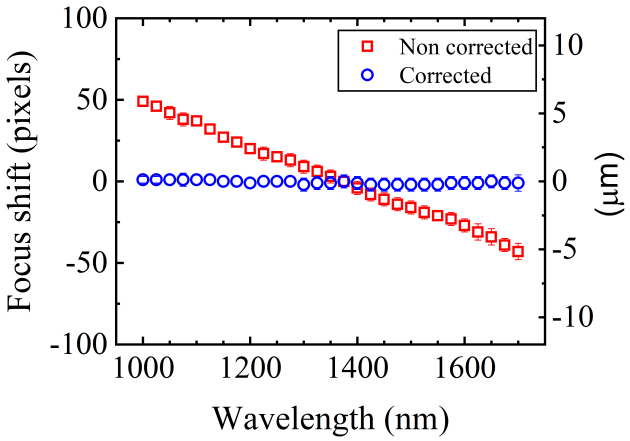

Figure 2.16: The position of focus on the camera versus wavelength set by the monochromator. Without correction, the focus shifts downwards with wavelength (red open squares). After correcting with the SLM ramps, the focus for each wavelength is positioned at the same location (blue open circles).

(see Figure 2.15(a)). Without correction, the focus produced by wavelengths shorter and longer than 1375 nm shift up or down with respect to the central spot. For example, when we set wavelength 1550 nm on the monochromator, the focus shifts down, as seen in Figure 2.15(b). We quantify the shift of focus position with respect to the central spot in figure 2.16. The angle of the blaze grating ramp was estimated geometrically by monitoring the shift of the focus with respect to the central spot. Thus, a blaze grating pattern is written on the SLM to correct the tilted light out of the monochromator by tilting the phase pattern to shift the focus to the central spot (Figure 2.15(c)). The maximum gray value that corresponds to 2π phase retardation for each wavelength in the entire measurement range was also calibrated. This was done by maximizing the reflected intensity from the SLM grating at the focal plane while changing the gray value from 0 to 255. The positions of focus for each wavelength after correction are also plotted in Figure 2.16.

Chapter 3

Characterization of the experimental setup using speckle statistics

Zinc oxide (ZnO) nanoparticles are known to scatter visible and NIR light. In an ideal situation of monochromatic light and uniform particle distribution, the intensity of speckles produced by such a medium is expected to follow an exponential probability distribution function. However, the limited temporal coherence of source and noise level of detectors cause deviations from the expected statistical parameters. We investigate the effect of the linewidth of our broadband tunable source and detector on the intensity statistics of speckle patterns produced at the scattered reflection of a slab of ZnO nanoparticles. We quantify the effect of the source linewidth and detector noise on our measurements by comparing the results with other high coherent laser sources and low noise detectors.

3.1 Introduction

Optical speckles are the result of constructive and destructive interference among the many paths that light takes while encountering a multiply scattering medium. In photonics, speckles are studied to characterize scattering of various samples and shaping wavefront of light to optimize speckle intensity to a certain target, also known as wavefront shaping. If the scattering nature of the material is known, the speckle pattern has expected intensity and phase distributions explained using speckle statistics [36]. Hence, in experimental studies, deviations from such expected parameters are studied to characterize experimental setups. In this chapter, we show characterization of our setup from speckle statistics in

a disordered scattering medium.

When laser light with a plane phase front is incident on a scattering sample such as an ensemble of zinc oxide (ZnO) nanoparticles, a speckle pattern is produced at both the transmission and the reflection side. The study of resulting speckle intensity and phase pattern is called speckle statistics, which is very useful for characterizing scattering media. In our experiments, camera images of speckle patterns are recorded, where only intensity and not phase information is collected. Therefore, we study the specific case of intensity statistics of speckles in this chapter. For a large number of phasors, the intensity I of fully developed speckles follow a negative exponential density function p_I given by [35]

$$p_I(I) = \left(\frac{I}{\bar{I}}\right) e^{-I/\bar{I}}, \tag{3.1}$$

where $\bar{I}$ is the mean intensity.

A widely used parameter to describe how well a speckle is developed is the speckle contrast C, that quantifies the fluctuations of the intensities with respect to the average intensity.

$$C = \frac{\sigma_I}{\bar{I}}, \tag{3.2}$$

where σ_I is the standard deviation of intensity.

A fully developed speckle has a maximum contrast $C = 1$ and the intensity follows the negative exponential distribution shown in eq. (3.1). To obtain fully developed speckles, uniform phase statistics of the phasors are required. If the phase distributions are non-uniform, the speckles are referred to as partially developed [119]. Partially developed or smeared speckle has contrast $C < 1$ and the intensity distribution deviates from the negative exponential. This type of speckle corresponds to scattering media with anisotropic components in optically very thin media with a limited number of scatterers [120, 121]. Another reason for partially developed speckle is media composed of scatterers that are in motion with speed faster than the frame rate of the detector [122]. For example, suspended particles in a fluid medium or medium with vibration. In such cases, the resulting speckles are averaged over multiple speckle patterns produced by every "freeze-frame" of the scatterers, thereby decreasing contrast. Hence static medium is another requirement for fully developed speckle.

In experiments, other factors namely coherence of the source and detector noise also largely influence intensity distributions and therefore the speckle contrast [123, 124]. In the case of low temporal coherence, *i.e.*, when the coherence length of the source is comparable to the sample size, interference effects are less strong and speckles are smeared due to speckle overlap among constituent frequency components. In this case, one expects lower contrast as intensity fluctuations are less. If detectors have high dark noise, that results in an underlying correlation in the background of the speckle images, which also decreases the contrast and intensity distribution deviates from exponential. Therefore, speckle patterns pro-

duced by a known strongly scattering medium can be used to characterize the effect of source linewidth and detector noise by comparing their behavior with ideal theoretical case in intensity statistics, and is the main goal of this study.

In this chapter, we characterize our newly developed setup by studying speckle statistics of a strongly scattering medium. In our optical setup, the spectrally filtered supercontinuum light has a linewidth $\Delta\lambda \approx 0.6$ nm that is 2 to 5 times magnitudes broader than typical commercial laser sources such as the above-mentioned source **2**[1]. To study the effect of the linewidth and detector noise, we investigate speckles produced by a slab of scatterers, when we use separate laser sources with different linewidths and detect with detectors with different noise levels. We study an ensemble of ZnO nanoparticles that are known to be transparent and scattering for visible and near-infrared (NIR) light [125–127]. We show that smeared speckles of contrast $C < 1$ are produced by the supercontinuum filtered by the monochromator. To verify that the effect is a combination of broad linewidth and high noise of the camera, we measure the same sample with a narrow linewidth source and low-noise camera and show that perfect exponential distribution of intensities and contrast $C = 1$ are achievable for such samples. We also study the intensity statistics of smeared speckle patterns obtained from adding multiple independent speckle patterns (Appendix 3.A) and find good agreement with theory.

3.2 Experiment

As a scattering sample, we study a thin layer of spray-painted ZnO nanoparticles [54] of thickness 32 μm, that was fabricated and also studied by van Putten [129] (picture of the sample is in Figure 3.1(a)). An SEM image of the constituent particles is shown in Figure 3.1(b). We use the optical setup described in chapter 2 to collect speckle statistics data. Linearly polarized, monochromatic light is focused on the ZnO slab using the high numerical aperture (NA = 0.85) focusing objective. The reflected light from the sample is detected with a camera in cross-polarized state with respect to the input. Thus, only the multiple scattered light is detected and specular reflection is avoided. We collect speckle images at different frequencies in the NIR range. A speckle pattern is detected as a camera image which we further investigate to study speckle statistics.

For this experiment, we use three different NIR monochromatic sources with different linewidths and two different cameras with different noise levels listed below.

Sources:

1. Fianium supercontinuum filtered with monochromator, $\Delta\lambda = 0.6 \pm 0.1$ nm, coherence length $l_c \approx 1$ to 2 mm.

[1] The reason for choosing this source is the magnificent tuning range that greatly exceeds most commercial tunable lasers.

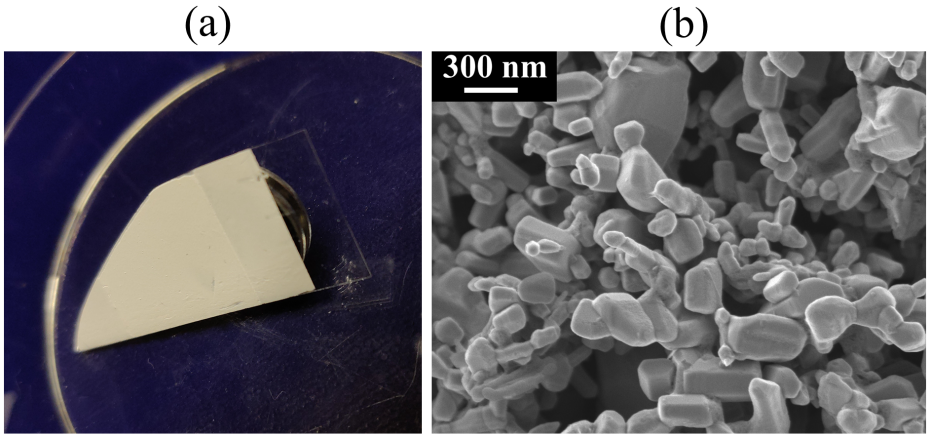

Figure 3.1: (a) The layer of ZnO sample studied here. It is spray- painted on a glass microscope cover slip. The sample is about 32 μm thick and appears fully white with visible light. (b) SEM image of the constituent particles of the sample. The ZnO particles are arbitrary in shape and size with average diameter of about 200 nm (figure courtesy: M. Goodwin). In ZnO nanoparticle formation, various shapes like hexagonal, cubic, spherical are common due to its molecular structure [128].

2. Tunable high resolution NIR laser (920 nm $< \lambda <$ 985 nm), $\Delta\lambda = 10^{-6}$ nm, coherence length $l_c \approx$ 1km (Toptica DLpro 11168)

3. DFB (distributed feedback) fiber coupled diode laser ($\lambda = 1550$ nm), $\Delta\lambda =$ 0.01 nm, coherence length $l_c \approx 200$ mm (Thorlabs S3FC1550).

Detectors:

A. Photonic Science InGaAs detector cooled shortwave infrared (SWIR) sensitive camera (950 nm $< \lambda <$ 1700 nm). High dark noise (64000 e^-/pix/sec) and low resolution (320 $\times$ 256 pixels, with individual pixel size 30 μm^2).

B. Allied Vision Si detector camera. Low dark noise (12.4 e^-/pix/sec) and high resolution (1388 $\times$ 1038 pixels with individual pixel size 6.45 μm^2), limited detection range in NIR ($\lambda <$ 1100nm).

The above numbering allows to refer to source-detector combinations used in the measurements, for example **1A** or **2B**, etc.

3.3 Speckle patterns and speckle statistics

The recorded speckle pattern in the camera image is shown in Figure 3.2(a) for a wavelength $\lambda = 950$ nm, using source-detector combination **1A**. The speckle pattern has a Lorentzian-like envelope due to the profile of the laser beam and the high NA objective that focuses it on the sample. Hence towards the outer

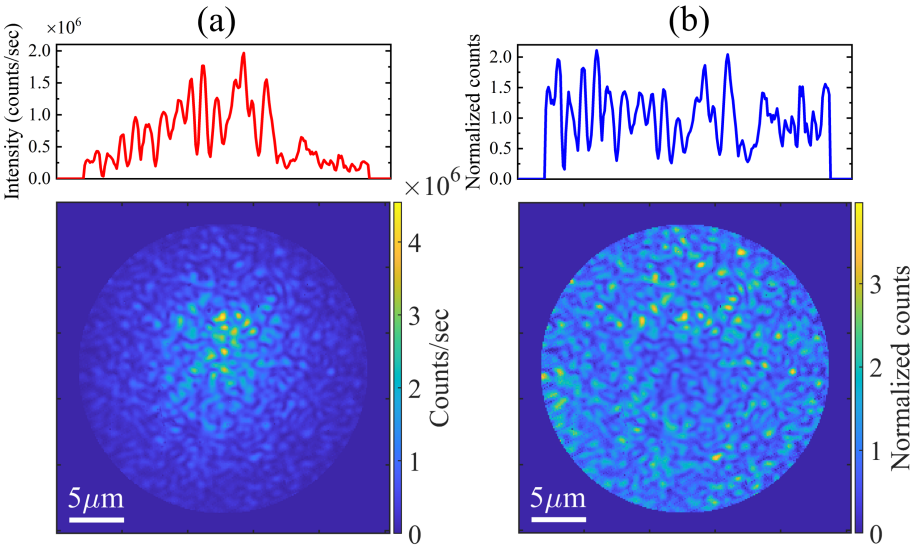

Figure 3.2: (a) Camera (InGaAs detector) image of a speckle pattern produced by light reflected from the disordered ZnO nanoparticles, when illuminated with wavelength $\lambda = 950$ nm, measured with source-detector **1A**. The speckle pattern has an underlying Lorentzian-like profile. On top, the intensity profile along one axis for one row of pixels is shown, which shows the presence of the Lorentzian-like envelope. (b) The normalized speckle pattern obtained by dividing the raw speckle pattern by the envelope obtained from averaging 30 independent speckle images to extract only the intensity fluctuations. The plot of the intensity profile above the image shows that the normalized speckle contains the intensity fluctuations without the Lorentzian background. The speckle images are cropped by a circular mask to avoid the instrumental artifacts near the edges of the camera.

area of the speckle image, signal to noise ratio is very low. Therefore, we record at least 30 independent speckle patterns by translating the sample and take an average of them to get the underlying envelope[2]. Then we divide the original image by the envelope to get a normalized speckle pattern that contains only the intensity fluctuation, as shown in Figure 3.2(b). From the intensity profile of the normalized speckles, it is observed that when we use the filtered supercontinuum source and detect with the InGaAs high noise camera, the intensity at the destructive interference is non-zero, which already reveals that the speckles are not fully developed. In Figure 3.3(a) and (b) we show two normalized speckle patterns measured at two different wavelengths 950 nm and 1550 nm, respectively, measured with source-detector **1A**. It is clear from the speckle patterns and the 1D speckle profiles above them that the size of individual speckles is smaller at wavelength $\lambda = 950$ nm than those at wavelength $\lambda = 1550$ nm, due to the

[2]See Appendix 3.B for checking how many independent patterns are ideal for a smooth envelope

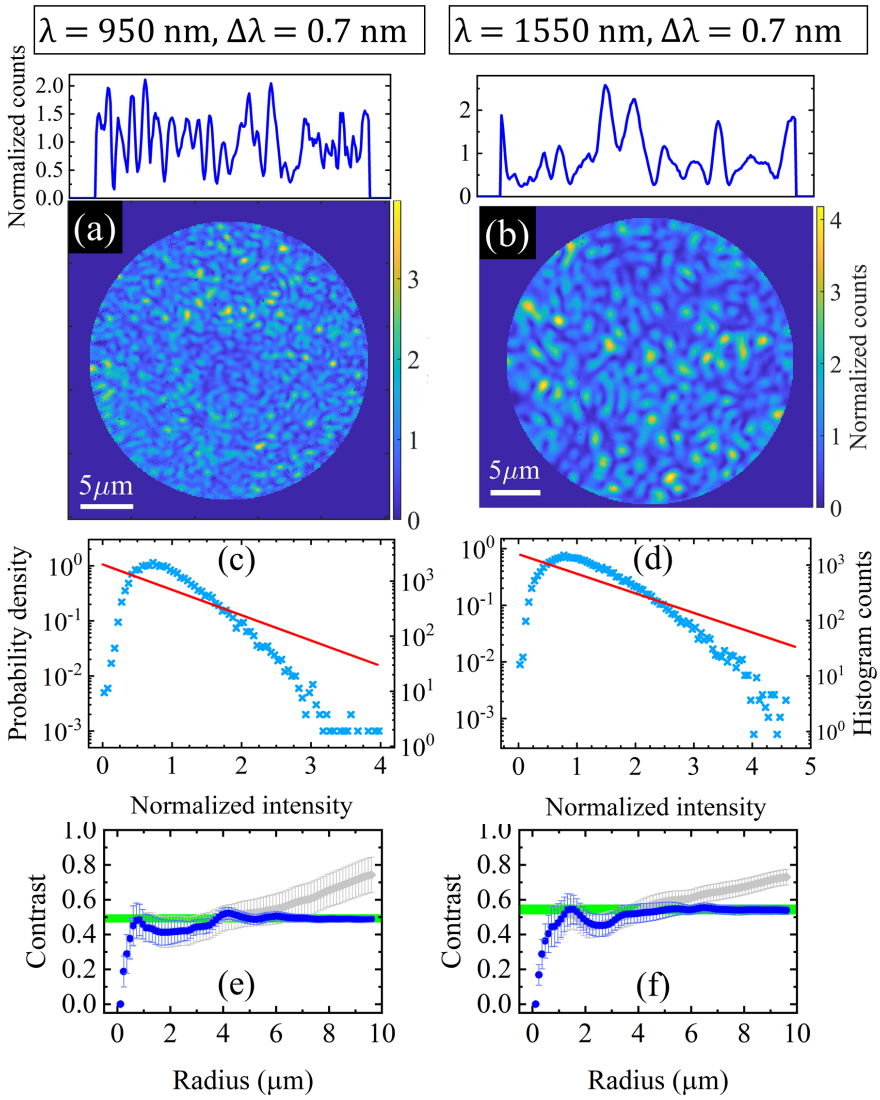

Figure 3.3: (a),(b) Camera images of speckle patterns measured with source-detector **1A** at wavelengths mentioned on the top. The intensity cross-sections are plotted above each image. (c),(d)Corresponding intensity distributions of the speckle patterns (blue crosses). The exponential probability density function expected from the intensities is plotted as the red lines. (e),(f)plot of speckle contrast versus radius of a circular area on the camera. At large radius, the contrast value converges for the normalized speckle pattern (blue dots) to $C = 0.49 \pm 0.02$ at 950 nm and $C = 0.54 \pm 0.03$ at 1550 nm. The converged contrast value is highlighted with the green strip. For the original speckle pattern with the envelope, the contrast increases with radius (grey diamond) as background effects become more dominant.

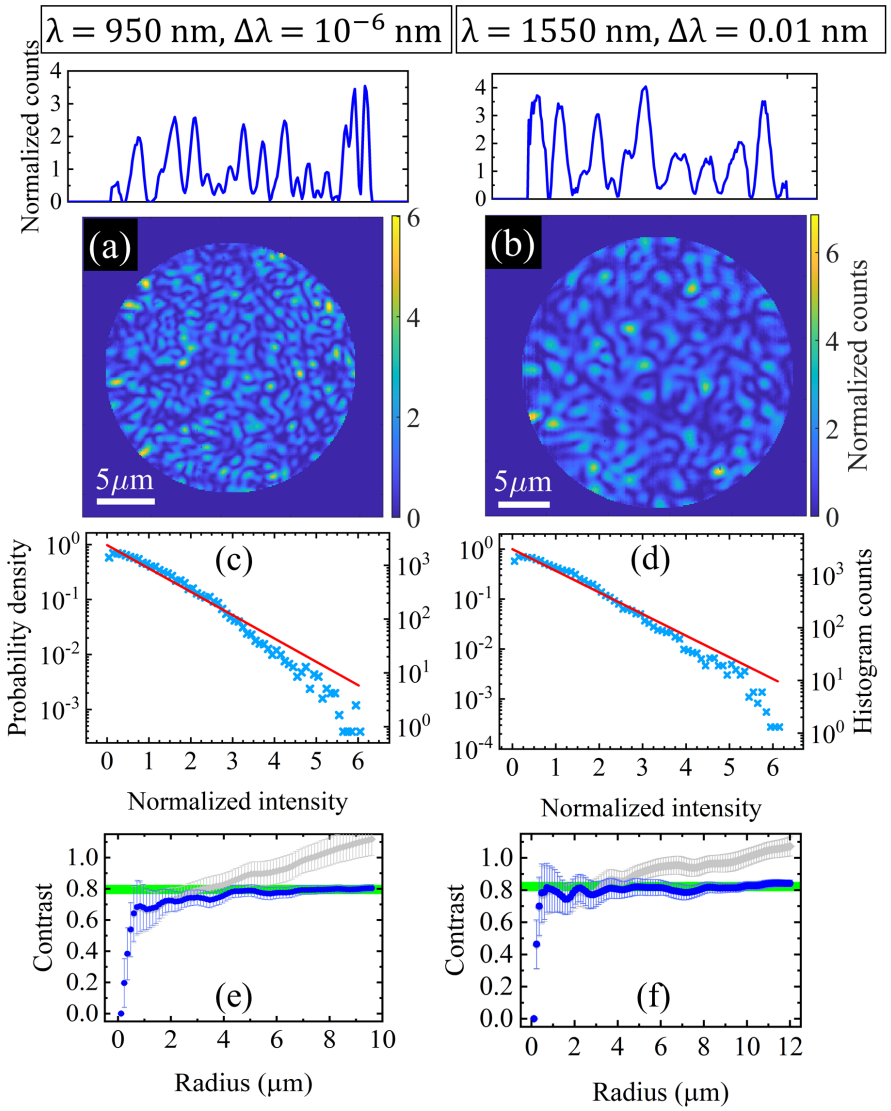

Figure 3.4: (a),(b) Camera images of speckle patterns measured with source detector **2A** and **3A** with wavelengths mentioned on the top. The intensity profiles are plotted above each image. (c),(d)Corresponding intensity distributions of the speckle patterns (blue crosses). The exponential probability density function expected from the intensities is plotted as the red lines. (e),(f)plot of speckle contrast versus radius of a circular area on the camera. At high radius, the contrast value converges for the normalized speckle pattern (blue circles) to $C = 0.78 \pm 0.03$ at 950 nm and $C = 0.82 \pm 0.03$ at 1550 nm. The converged contrast value is highlighted with the green strip. For the original speckle pattern with the envelope, the contrast increases with radius (grey diamond) as background effects become more dominant.

diffraction limit of the imaging system.

We plot the intensity distributions of the normalized speckle patterns for two wavelengths *viz.* 950 nm and 1550 nm, as shown in Figure 3.3(c) and (d). The respective speckle patterns are shown in Figures 3.3(a) and (b). For comparison, we also compute the expected probability density distribution for fully developed speckle from our data using equation 3.1. It is observed that the intensity distributions deviate from the expected exponential function in these cases. The deviation is primarily due to the lowest intensities of the speckle pattern being > 0. Therefore, there is a Gaussian-like profile near low intensities, which is a signature of smeared speckle patterns [35].

Next to the intensity distributions, we also compute the speckle contrast. For a correct estimation of speckle contrast, a sufficient number of speckles needs to be accounted for. The number of speckles N can be counted as either one speckle spot in N independent speckle patterns, or N speckle spots within the same speckle pattern. Here we use the latter case, *i.e.*, compute contrast between different speckle spots within the same speckle pattern. When N is sufficiently large, the value of speckle contrast converges to the real contrast for that speckle pattern. Therefore, to check if N is enough within each speckle pattern, we take different areas on the speckle pattern and compute the contrast among the speckles within that area. We start with a circular area of radius R in the middle of the speckle patterns and compute the contrast as started in equation 3.2 within the area of the circle with radius R. As we increase the radius, the number of speckles within the area also increases. In Figures 3.3(e) and (f) we plot the computed contrast of the corresponding speckles as a function of radius, while the error bars are the standard deviations of contrast computed for many independent speckle patterns using the same source and detector. We see that for the normalized speckles at higher radii $R > 4$ μm, the contrast converges to a steady value, and error bars become smaller, which we assign as the contrast for that speckle pattern. Here again, we see the need for speckle normalizing, as it is seen from the contrast values for the original speckle pattern diverge and have large error bars, as background dominates at higher radii. For **1A** case, we find speckle contrast $C = 0.49 \pm 0.02$ at 950 nm and $C = 0.54 \pm 0.03$ at 1550 nm, which are much less than the expected $C = 1$ for the type of scattering sample under study.

To investigate whether the low contrast of speckles is due to the comparatively broad linewidth of our filtered supercontinuum source, we do the same measurements using the narrow linewidth sources listed above, with combinations **2A** and **3A**. We tune the wavelength of the narrow bandwidth NIR laser (source **2**) to $\lambda = 950$ nm and record speckle images in reflection from the same sample. Similarly, we perform the same experimental steps using the 1550 nm narrow linewidth diode laser (source **3**). In both cases, the intensity minima of the speckle spots are closer to zero. Indeed, the intensity distributions for the narrow linewidth sources are closer to the expected exponential for fully developed speckle (see Figure 3.4), as compared to those for the broad bandidth source. The speckle contrast in this case are $C = 0.78 \pm 0.03$ at 950 nm and $C = 0.82 \pm 0.03$ at 1550 nm. Using narrow linewidth sources increases speckle

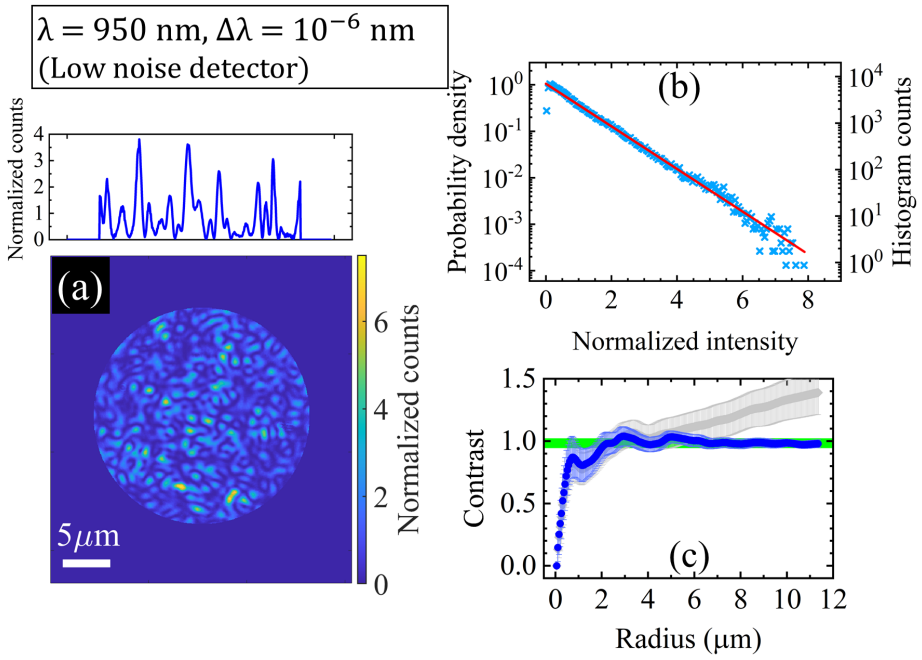

Figure 3.5: (a) Camera (Si detector) image of a speckle pattern produced by the narrow linewidth source wavelength 950 nm, measured with source-detector **2B**. The intensity profile is plotted above the images. (b) Corresponding intensity distribution of the speckle pattern (blue crosses). The exponential probability density function obtained from the intensities is plotted as the red line. (c) plot of speckle contrast versus radius of a circular area on the camera. At high radius, the contrast value converges for the normalized speckle pattern (blue dots) to $C = 0.98 \pm 0.03$, while for the original speckle pattern with the envelope, the contrast increases with radius (grey diamond data points) as background effects are more dominant.

contrast closer to $C \to 1$, yet there is another factor that is limiting the speckle contrast and causing deviation from exponential statistics, as discussed below.

The second experimental factor that affects speckle contrast in our experimental setup is the detector. The InGaAs detector has a high thermally generated dark current. Subtraction of background (images taken by blocking all light) removes the mean background offset but does not remove all the random fluctuations. Therefore, we use a second camera, namely the Si detector to study speckle statistics of ZnO. In addition to lower dark current, the Si detector also has higher imaging resolution. In this work, we do not quantify the effect of the larger pixel size of the InGaAs detector, as the size of speckle spots (about 120 μm diameter at wavelength 950 nm) are approximately 4 pixels wide, which is greater than the 2 pixels necessary for discounting the nyquist noise arising from pixellation of the speckle pattern [130, 131]. Since the Si detector is not NIR

sensitive above 1100 nm, we record speckle patterns at 950 nm using the narrow linewidth source, for comparison with previous cases (3.5(a)). In this case, we now have the 'perfect' experimental situation to yield the expected fully-developed speckle pattern from our sample. The intensity distribution shown in Figure 3.5(b) follows the exponential function perfectly, with the highest speckle contrast of $C = 0.98 \pm 0.03$.

3.4 Conclusion

Our observations verify that fully-developed speckles are produced by the ZnO sample when a narrow linewidth source is used and the detector has very low noise level. The deviation from exponential for the speckle intensity distributions and a low speckle contrast indicates the effect of source and detector on measurements. In the following chapters for our broadband NIR experiments, we have to compensate the narrow linewidth with the comparatively broader width source as we need a wide range of wavelengths compatible with Silicon photonics where absorption is negligible. Also, the coherence length of our source is still longer than the effective length scales in the sample that we study. Similarly, we have to compensate the low noise camera with the high noise InGaAs detector to detect the broad range. The investigations presented in this chapter thus quantify the effect of source linewidth and detector noise in measurements.

Appendix 3

3.A Speckle averaging

In this appendix, smeared, low contrast speckle patterns are investigated that are constructed by adding multiple independent fully-developed speckle patterns. We use the theory derived in chapter 3 of Ref. [35]. As can be guessed, the intensity statistics of speckle pattern obtained from adding N independent patterns follow different behavior than the standard exponential distribution for fully developed speckles and is given by

$$p_s(I_s) = \sum_{n=1}^{N} \frac{\bar{I}_n^{(N-2)}}{\prod_{p=1,p\neq n}^{N}(\bar{I}_n - \bar{I}_p)} e^{-\frac{I_s}{\bar{I}_n}}, \tag{3.3}$$

where p and n denote index of independent speckles and I_s are the intensities of the added speckle patterns. We consider the case of $N = 2$, for two independent spekle patterns with intensities I_1 and I_2, where the distribution is simplified to the following expression:

$$p_s(I_s) = \left(\frac{1}{\bar{I}_1 - \bar{I}_2}\right)\left(e^{-\frac{I_s}{\bar{I}_1}} - e^{-\frac{I_s}{\bar{I}_2}}\right), \tag{3.4}$$

where $I_s = I_1 + I_2$.

The speckle contrast of the added pattern depends on the average intensities of the individual speckle patterns and the ratio between them,

$$C_s = \frac{\sigma_s}{I_s} = \frac{\sqrt{\bar{I}_1^2 + \bar{I}_2^2}}{\bar{I}_1 + \bar{I}_2} = \frac{\sqrt{1+r^2}}{1+r}, \tag{3.5}$$

where $r = \dfrac{\bar{I}_2}{\bar{I}_1}$. Therefore, it is possible to estimate speckle contrast of the summed speckles when the average intensities of the constituent individual patterns are known. When the average intensities are equal for each pattern, then the expression for speckle contrast reduces to

$$C_s = \frac{1}{\sqrt{N}}. \tag{3.6}$$

So when $N = 2$, the contrast is expected to be $\dfrac{1}{\sqrt{2}} = 0.7071$, which is only applicable when the individual speckles are fully developed.

As an example, we pick two speckle patterns recorded by moving the sample far along the focal plane in order for the speckle patterns to be independent of each other. We use the low noise camera and narrow linewidth source (combination **2B**) so that we start with fully developed speckles. Then we add the two patterns as shown in the top row of Figure 3.6. The resulting pattern is comparatively

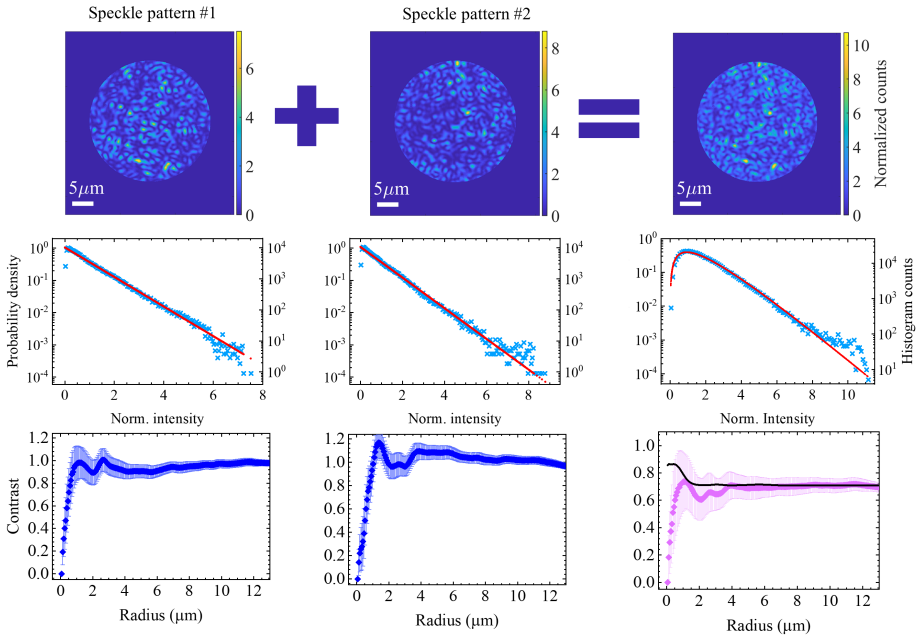

Figure 3.6: Top: Camera (Si detector) images of two independent speckle patterns produced by the narrow linewidth source wavelength 950 nm (source-detector **2B**), added to obtained a summed speckle image. Mid: Corresponding intensities of the speckle patterns (light blue crosses) follow the expected exponential distribution, while that of the summed deviate from it. The exponential probability density function obtained from the intensities is plotted as the red lines. For the summed speckle pattern, the probability function obtained from equation (3.4), and matches well with the data. Bottom: Plots of speckle contrast versus radius of a circular area on the camera. At high radius, the contrast value converges for the normalized speckle pattern (blue dots) to $C_1 = 0.98 \pm 0.03$, $C_2 = 1.01 \pm 0.02$ while for the summed speckle pattern the contrast is lower $C_1 = 0.704 \pm 0.05$. The contrast computed using equation (3.5) is plotted as the solid black curve.

smeared than the individual patterns. The intensity distribution of the resulting pattern has similar shape as those in Figure 3.3, although in these two cases the reason of deviation from exponential behavior are different. We then compute the distribution using relation (3.4) with individual and the sum of intensities of the measured speckle patterns as input. The resulting curve match well with the intensity distribution of the summed speckles. From the usual method, we find a contrast value of $C_s = 0.704 \pm 0.05$, which agrees well with the expected value, since in our case, $r = 1.04$. Taking this ratio into account, we compute the contrast using equation (3.5) and find a good match with contrast computed for the summed speckle pattern as seen in Figure 3.6.

3.B Number of independent speckle patterns for a smooth envelope

As N increases, contrast would decrease until we get a uniform, fully diffused pattern with 0 contrast. The number of individual speckle patterns needed to be recorded to obtain a smooth envelope can be estimated near the limit $C_s \to 0$. In our case we took $N = 30$ independent patterns which results in an envelope with average contrast of $C_s = 0.18$. Since the envelope is not smooth enough for normalizing the speckle patterns, a 2D Gaussian smoothing kernel filter of standard deviation 5 was applied to the summed speckle image. Ideally N should be as large as possible in case of fully developed independent speckle patterns. Although, in case of partially developed independent speckles of low contrast as in Figure 3.3, N can be much smaller. We propose that in this case the contrast of average speckle pattern will scale as

$$C_s \equiv \frac{C_i}{\sqrt{N}}, \tag{3.7}$$

where C_i is the average contrast of the independent speckles.

Chapter 4

Broadband wavefront shaping and speckle correlation in disordered media

Wavefront shaping (WFS) is now a known method to enhance wave intensity inside or behind a multiple scattering medium. We perform WFS over a broad range in the NIR frequencies including all the telecom bands to focus light behind a scattering medium. We first verify that the optical thickness of the medium determines the frequency width over which an optimized phase pattern works, which is also given by the first order speckle correlation function. We finally show that by decreasing the sample thickness within the limit of multiple scattering, the frequency bandwidth of the optimization can be tuned to as large as tens of THz in the NIR range.

4.1 Introduction

Light undergoes multiple scattering when encountered with a strongly scattering medium. The resulting speckle pattern is the result of a random phasor sum of many different light paths inside the sample, see Figure 4.1(a). By modulating the phase of the incoming beam, a focus behind scattering media can be created, which is the technique called wavefront shaping (WFS), first proposed and demonstrated by COPS scientists Vellekoop and Mosk [45]. WFS is now a well-known technique in optics that has been extensively used in many fields like super-resolution imaging [46, 47], microscopy [48], endoscopy [49, 50], and

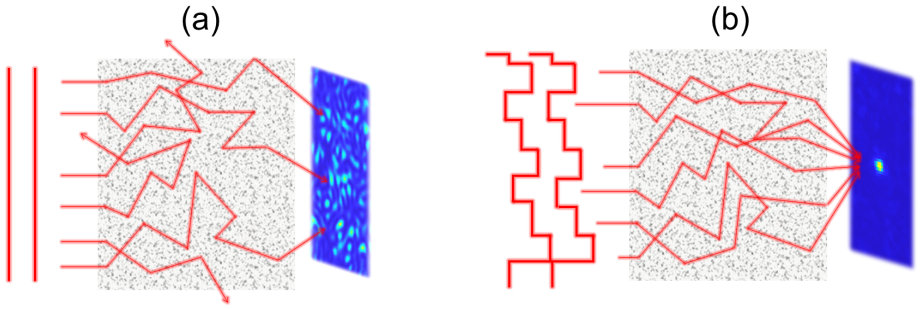

Figure 4.1: (a) Coherent plane waves impinge on a multiply scattering medium. Light undergoes random walks through various scattering centers in the medium until finally exits the medium in any arbitrary directions. A speckle pattern is formed at the exiting side (in this case in transmission). (b) The phase wavefront of the incident light is optimized spatially so that all of the transmitted channels end up at a specific target on the output side – the phenomenon of wavefront shaping to focus light behind scattering media.

cryptography [51, 52] . In WFS, the phases of the input wavefront are adjusted so that after undergoing multiple scattering all the light constructively interferes at a desired target, as shown in 4.1(b). This optimization, however, is dependent on the frequency of the input light. Since with WFS, a scattering medium is turned into a focusing lens, obtaining WFS optimization over a wide spectral range would give us aberration-free broadband light focusing, which is very useful in imaging and microscopy applications. Also, in industrial applications such as directing light for optical communication such as Light Fidelity (LiFi) systems [132–134], it is desirable to have controlled light steering over a broad spectral range.

For WFS over a broad spectral range, generally, the optimization has to be done for each frequency in that range. Such processes could be tedious and take a lot of computer memory. If the optimization works for a certain bandwidth, the number of optimization steps can be reduced significantly. Therefore, if one is interested in wavefront shaping over a very broad range, it is desirable to have a broad bandwidth over which the same optimized pattern is functional and thus requires a few optimization steps to cover a large frequency range. One way to estimate the bandwidth of the wavefront without wavefront shaping is to find the frequency speckle correlation function for the medium [135]. In disordered media, speckles are correlated when the frequency is changed over a certain range, called the speckle correlation [136–138]. In experiments, the speckle correlation is estimated by measuring the correlation between speckles at a certain center frequency and speckles produced when the frequency is detuned over a range in either direction, using the same input beam profile. The speckle short-range correlation $C^{(1)}$ is an exponentially decreasing function with detuning frequency [139–141]. The speckle correlation depends on sample parameters like thickness

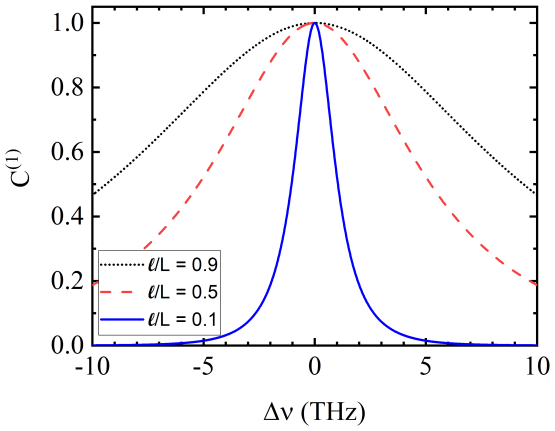

Figure 4.2: The correlation function $C^{(1)}$ as defined in equation 4.1 versus detuning frequency $\Delta\nu$, for three different inverse optical thickness ℓ/L of the sample. For optically thinner samples, the correlation peak is wider compared to thicker samples. The values are calculated for center frequency $\nu_c = 193$ THz ($\lambda_c = 1550$ nm), and sample thickness $L = 10$ μm.

(L), photon mean-free path (ℓ) and the effective refractive index of the medium (n_{eff}). For a scattering medium without absorption, the frequency-dependent short-range analytic correlation function is given by [140–142]

$$C^{(1)}(\Delta\nu) = \frac{4\pi L^2 \dfrac{\Delta\nu}{D}}{\cosh\left(L\sqrt{\dfrac{4\pi\Delta\nu}{D}}\right) - \cos\left(L\sqrt{\dfrac{4\pi\Delta\nu}{D}}\right)}, \tag{4.1}$$

where D is the diffusion coefficient that depends on the velocity of light in the sample and the mean free path:

$$D = \frac{c_0}{n_{\text{eff}}}\frac{\ell}{3}, \tag{4.2}$$

where c_0 is the velocity of light in vacuum. Using the expression 4.1 of speckle correlation function, unknown sample parameters like the diffusion constant and transport mean-free path can be estimated from experimental observations. $C^{(1)}$ effectively depends on the optical thickness of the medium, which is defined by the ratio of the sample thickness to the transport mean-free path. The curves of $C^{(1)}$ versus $\Delta\nu$ calculated for three different optical thicknesses are shown in Figure 4.2.

In this chapter, we perform wavefront shaping to produce a focus on the transmitted signal of a disordered, strongly scattering medium across a broad frequency range in the NIR. We show that the optimized phase pattern for a certain frequency is valid for a wide frequency range around the center frequency.

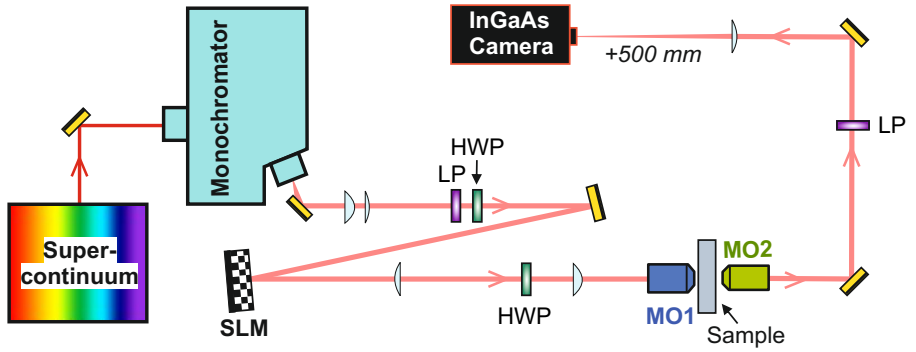

Figure 4.3: The experimental setup for performing wavefront shaping over a broad range of frequencies in NIR to focus light behind a scattering sample. The setup is an edited, simpler version of the one described in chapter 2 Figure 2.6.

The frequency correlation between speckle patterns formed by unoptimized wavefronts follow the same trend as the WFS target intensity with frequency detuning. We find the transport mean-free path of the sample in the near-infrared (NIR) range including the telecom bands by comparing the correlation function with theory. We also analytically investigate tuning of the frequency correlation width when changing the optical thickness of the sample and show that the correlation bandwidth and hence the optimization bandwidth can be increased to as wide as tens of THz.

4.2 Sample and experiment

We use an ensemble of disordered zinc oxide (ZnO) nanoparticles spray-painted on a standard glass microscope coverslip, with an average particle diameter of 200 nm (see Figure 3.1). The disordered ZnO slab has a thickness of $L = 32 \pm 1$ μm and a transport mean free path $\ell = 0.6 \pm 0.2$ μm at wavelength 532 nm, obtained from total transmission measurements [129].

For this experiment, a small alteration[1] of the experimental setup shown in Figure 2.6 was done. The full setup to do the experiment of this chapter is shown in Figure 4.3. We only collect the crossed polarized signal to detect the multiply scattered light by the medium and avoid ballistic light. For details, see appendix 4.A at the end of this chapter.

A frequency from the supercontinuum source is set by the monochromator and the spectrally filtered light incidents on the reflective spatial light modulator

[1]The microscope objective MO2 was moved to collect transmitted signal instead of lateral scattered signal.

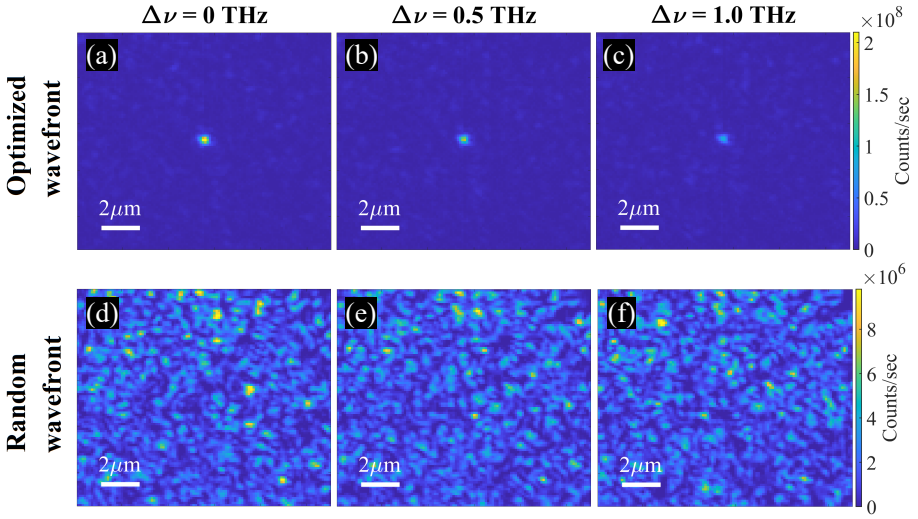

Figure 4.4: (a) Wavefront shaped focus on the transmission of the sample. The SLM pattern was optimized at the center frequency $\Delta\nu = 0$, that corresponds $\nu_c = 221.5$ THz or wavelength $\lambda_c = 1350$ nm. An intensity enhancement of about $100\times$ is achieved at the target location. The images obtained by further detuning the frequency by $\Delta\nu = 0.5$ THz and $\Delta\nu = 1$ THz and keeping the same optimized pattern are shown in (b) and (c) respectively. (d) Speckle pattern produced by a random wavefront set on the SLM with the same size of superpixels and center frequency. (e,f) The same random phase pattern is kept on the SLM and speckle patterns are recorded on the camera while detuning the center frequency by $\Delta\nu = 0.5$ THz and $\Delta\nu = 1$ THz.

(SLM). The reflected, phase-modulated wavefront from the SLM is then focused onto the sample surface through the first objective MO1. The second objective MO2 collects the scattered, transmitted light and thereafter the light is directed to the InGaAs NIR detector camera, as shown in Figure 4.3. We choose 32×32 pixels size of superpixels on the SLM. A target spot of a few pixels is chosen on the camera where we want to have wavefront-shaped focus. Then, using the intensity at the target spot as the feedback, the phase of each superpixel is changed from 0 to 2π, and the pixel is assigned the phase value where intensity is the maximum. This procedure is applied to all the pixels in the chosen area of the SLM, and the desired focus is obtained for the selected frequency of light. The procedure is repeated for several frequencies across a broad spectral range in the NIR from the extended E-band to the long-wavelength L-band of the telecom ranges.

4.3 Results and discussion

4.3.1 Broadband wavefront shaping

After optimization of the input wavefront, we get a focus on the transmission of the ZnO sample, shown in Figure 4.4(a). At the target spot, we obtain an intensity enhancement of about $\eta = 100\times$. Before the optimization, the output transmission signal is a speckle pattern shown in Figure 4.4(d). All data shown in Figure 4.4 are for center frequency $\nu_c = 221.5$ THz or wavelength $\lambda_c = 1350$ nm, which is in the E band of the extended telecom ranges. Next, we move to analyze the spectral range over which the same optimized pattern would produce a focus behind the sample.

Once we have the optimized phase pattern, we detune the frequency of the incident light systematically up to several THz, while keeping the same phase pattern on the SLM. For the case of center frequency $\nu_c = 221.5$ THz, we show in Figure 4.4(b) and (c) two camera images of the transmitted signal when the frequency was detuned to $\Delta\nu = 0.5$ THz and $\Delta\nu = 1$ THz, respectively. It is clearly observed that the optimized wavefront at ν_c still produces a focus at the same target spot, with decreasing intensity as $\Delta\nu$ increases. Therefore, the graph of intensity versus $\Delta\nu$ gives the spectral bandwidth over which a WFS optimized pattern works. We plot the data in Figure 4.6 (blue pentagons), where the bandwidth is expressed as the full width at half maximum (FWHM) of the peak, in this case, $\delta\nu = 1.3$ THz. This observation also shows that the frequency width of the optimized pattern is not limited by the linewidth of our source, as the linewidth is much narrower (≈ 0.2 THz) than the frequency width of the focus intensity.

The optimization to produce a focus is then repeated for 6 different center frequencies ν_c over a broad range. The same procedure of frequency detuning is also applied to each case and the intensity at the target spot is plotted as a function of the absolute frequency in the top panel of Figure 4.5. In the bottom panel of Figure 4.5, the FWHM bandwidths of each peak are plotted against the same abscissa. The bandwidth with respect to frequency decreases, which agrees with earlier observations in the visible range [143].

4.3.2 Speckle correlation

A random phase pattern is set on the SLM and the transmitted speckle pattern is recorded, shown in Figure 4.4(d). To find the frequency correlation of the speckle pattern, we detune the frequency away from the center frequency, this time keeping the same random phase pattern on the SLM, and record camera images of the speckle patterns on the transmission. Then we find the correlation between the speckle patterns at ν_c and at $\nu_c + \Delta\nu$. The correlation values thus obtained are plotted in Figure 4.6 versus $\Delta\nu$ as the red crosses. The speckle correlation matches very well with the target intensity plot for WFS, agreeing with previous observations [135]. To check how well our data match the expected correlation function for the sample, we compute the correlation using equation 4.1 as a function of frequency detuning using known sample parameters. We fit

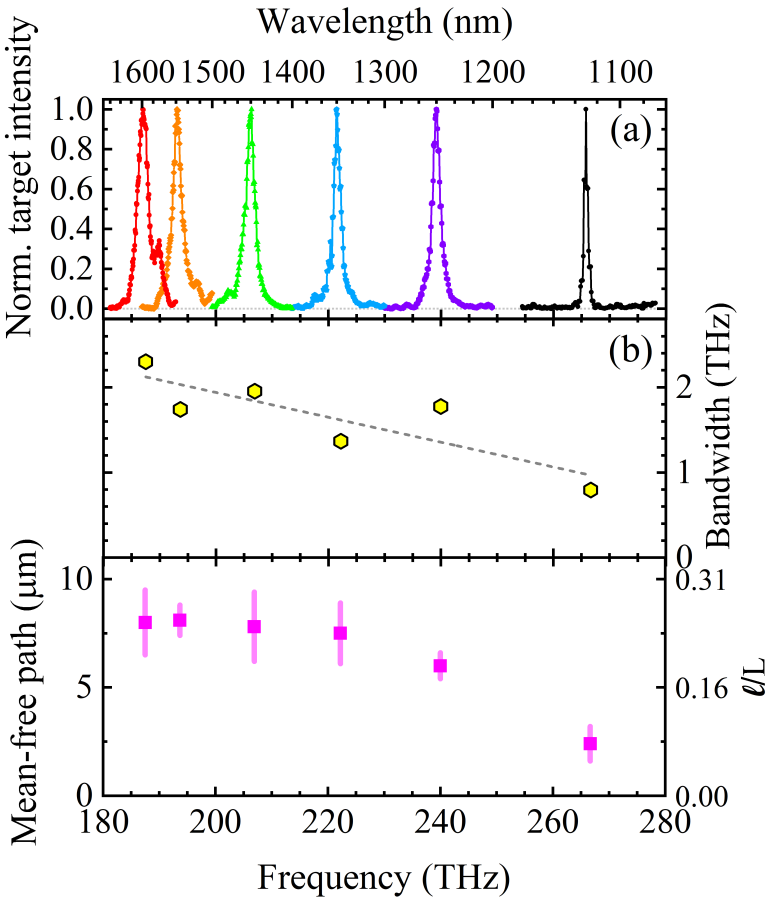

Figure 4.5: (a) Intensity at the target spot when the input phase of the wavefront was optimized independently for 6 different center frequencies ν_c (corresponding to each intensity maxima) over a broad range in the NIR. Each peak has a certain bandwidth, that defines the bandwidth over which the same optimized pattern successfully produces a focus. The 6 different colors correspond to 6 different optimized patterns for each of the center frequencies. (b) The bandwidths of the 6 peaks are taken as the FWHM's as a function of frequency. The grey dashed line is a linear fit through the data to visualize the overall declining bandwidth with frequency. (c) Transport mean-free paths extracted from speckle correlation function fitted for every center frequency where data was measured.

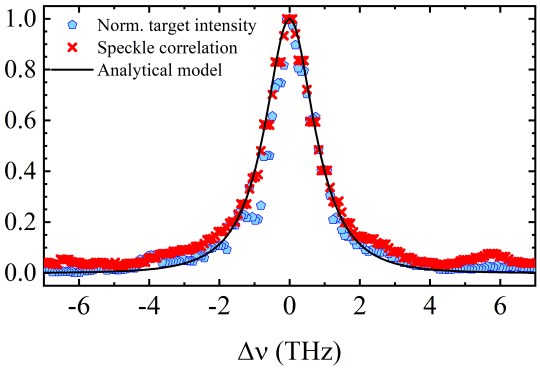

Figure 4.6: The correlation between a speckle pattern produced at $\Delta\nu = 0$, where $\nu_c = 221.5$ THz by a random wavefront and those produced at $\Delta\nu \neq 0$ produced by the same phase pattern, versus $\Delta\nu$ (red crosses). The analytical model of the speckle correlation function using sample parameters agrees very well with the experimental data (solid black line) with mean-free path $\ell = 7.5$ μm. The normalized intensity at the target spot after wavefront shaping agrees very well with the speckle correlation function (blue pentagons).

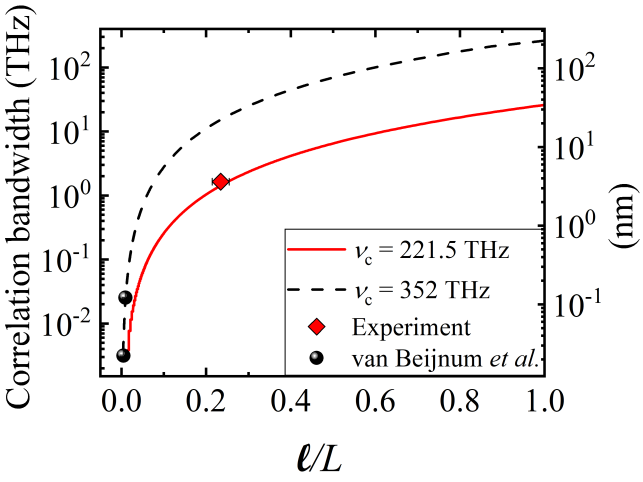

Figure 4.7: The bandwidth of the correlation curve measured as the full width at half maxima (FWHM) of the $C^{(1)}$ correlation peak versus the inverse optical thickness of the medium, ℓ/L. The solid curve is obtained from the correlation model computed for $\ell = 7.5$ μm and at center frequency $\nu_c = 221.5$ THz (or $\lambda_c = 1350$ nm). The red diamond is the experimental data point obtained for the same center frequency and mean-free path, which agrees well with the model. For comparison, we plot the experimental data from van Beijnum *et al.* [135] as the black spheres. The dashed curve is obtained from the correlation model for a similar sample and center frequency computed for $\ell = 0.7$ μm and at center frequency $\nu_c = 352$ THz (or $\lambda_c = 852$ nm).

equation (4.1) to our data and find the transport mean free path to be $\ell = 7.5 \pm 0.7$ μm at $\lambda = 1350$ nm, as shown in Figure 4.6. The value of the mean-free path is consistent with those estimated from enhanced backscattering spectroscopy and total transmission measurements of similar samples in Refs. [144, 145]. The known input parameters used here are the sample thickness $L = 32 \pm 1$ μm and the effective refractive index $n_{\text{eff}} = 1.4 \pm 0.1$. Similarly, we extract mean-free paths for other frequencies measured and plot them in Figure 4.5(c).

Next, we investigate how to tune the bandwidth of the speckle correlation, which effectively determines the bandwidth over which the WFS optimized pattern is functional to produce focus behind scattering media. Since the correlation bandwidth directly gives the WFS bandwidth, we investigate how broad width can be achieved by tuning sample parameters. Using equation 4.1, the correlation function is computed while sample thickness varies from $L = \ell$ to $L = 60\ell$, while keeping ℓ constant. Here we use the sample parameters for ℓn_{eff} and center frequency 221.5 THz. Then from the correlation peaks, the FWHM's are extracted as the correlation bandwidth and plotted versus the inverse of the optical thickness ℓ/L in Figure 4.7.

When the sample is optically thick, the correlation bandwidth is very narrow and it increases as the sample becomes optically thinner. Hence, as long as scattering is dominant in the medium, the optical thickness can be tuned to obtain the desired bandwidth. The data point obtained from our experiment is plotted in the same graph, which agrees very well with the analytical curve for effective index 1.5. To check consistency of our calculation and experiment, we plot the two data points from van Beijnum *et al.* [135], where a different center frequency and much thicker samples were used. Therefore, we do another calculation for correlation functions using these parameters ($\ell = 0.7$ μm and $\nu_c = 352$ THz) and compute bandwidth for varying optical thickness. In this case, we vary the sample thickness from $L = \ell$ to $L = 280\ell$, to include the experimental range. The data points match very well with the model and show the consistent dependency of correlation bandwidth with the optical thickness.

4.4 Conclusion and outlook

We performed optical phase-only WFS at various frequencies across the NIR range to focus behind a slab of an ensemble of ZnO scattering nanoparticles. The transport mean-free paths at these different frequencies are extracted for the ZnO sample of thickness 32 μm. The frequency bandwidth of the WFS focus matches with the expected correlation bandwidth of speckle patterns produced by detuning the center frequency. The observation of the wide frequency bandwidth of the correlation and hence the optimized pattern is not limited by the linewidth of our source, since the correlation width is much wider ($\delta\nu > 1$ THz) than the source linewidth (0.2 THz). We have shown that the frequency bandwidth of the speckle correlation function can be modified by changing the optical thickness of the sample. The correlation bandwidth, and hence the WFS bandwidth can be as large as tens of THz within the multiple scattering limit $\ell < L$. We

observe a comparatively faster increase of correlation bandwidth with decreasing sample thickness when light with higher frequency is used. Although, there is a limit up to how thin the sample should be, and that is the scattering limit. For very thin samples ($\ell/L \to 1$), most of the light passes through the sample without scattering as ballistic transmission. Hence wide correlation bandwidth in that regime is caused by the high correlation between the unaltered input and output wavefronts. In experiments for such cases, cross polarized detection is necessary to avoid the ballistic light, and collect only the multiple scattered light. Therefore it is always required to check, depending on application, how much light is scattered considering geometry of the sample and shape of the incident beam. In future, we would like to measure samples with varying optical thickness to check the experimental limit of the correlation bandwidth.

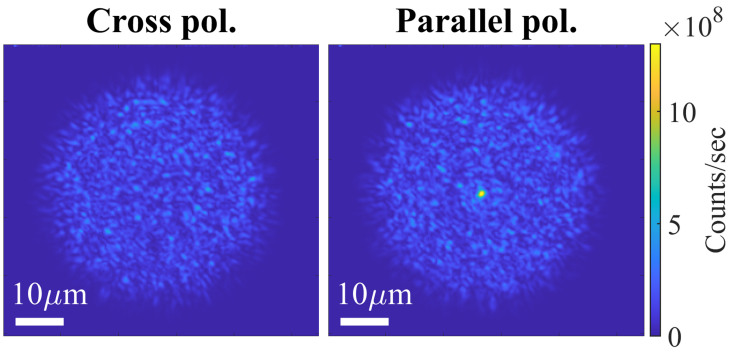

Figure 4.8: Speckle images on the transmission of the sample with linearly polarized incident light with plane wavefronts. The detection is done at two orthogonal polarization states, *viz.* cross and parallel with respect to input, as mentioned on the titles.

Appendix 4

4.A Cross and parallel polarized detection of the transmitted light

The incident light on the sample is linearly polarized, and first we check the transmitted signal both in cross and parallel polarized states with respect to the input. In cross polarized state, only multiple scattered light is detected as initial polarization gets scrambled by many scattering events in the medium [6, 33, 34]. If there is ballistic light, i.e. light that transmits through the medium without getting scattered, the polarization of the input state would still be maintained. Hence, in parallel polarized state, ballistic components (if there is any) can be detected. We show two images in Figure 4.8 for the two types of orthogonal polarization detections. In cross polarization, a speckle pattern of the multiple scattered light is formed as shown in the left image of Figure 4.8. Since we used plane wave input, for parallel polarized detection, it is observed that there is a considerable amount of intensity (about 10× more than the rest) near the center of the speckle pattern at the location of the input focus. This observation shows that our sample is in the multiple scattering regime, while a small fraction of light escapes without scattering, making the sample not fully opaque. Hence, to ensure that we only measure the multiple scattered light, in all measurements we use cross polarized detection.

Chapter 5

Experimental probe of a 3D photonic band gap

The identification of a complete three-dimensional (3D) photonic band gap in real crystals typically employs theoretical or numerical models that invoke idealized crystal structures. Such an approach is prone to false positives (gap wrongly assigned) or false negatives (gap missed). Therefore, we propose a purely experimental probe of the 3D photonic band gap that pertains to any class of photonic crystals. We collect reflectivity spectra with a large aperture on exemplary3D inverse woodpile structures that consist of two perpendicular nanopore arrays etched in silicon. We observe intense reflectivity peaks ($R > 90\%$) typical of high-quality crystals with broad stopbands. A resulting parametric plot of s-polarized versus p-polarized stopband width is linear ("y=x"), a characteristic of a 3D photonic band gap, as confirmed by simulations. By scanning the focus across the crystal we track the polarization-resolved stopbands versus the volume fraction of high-index material and obtain many more parametric data to confirm that the high-NA stopband corresponds to the photonic band gap. This practical probe is model-free and provides fast feedback on the advanced nanofabrication needed for 3D photonic crystals and stimulates practical applications of band gaps in 3D silicon nanophotonics and photonic integrated circuits, photovoltaics, cavity QED, and quantum information processing.

The content of this chapter has been published in: M. Adhikary, R. Uppu, C. A. M. Harteveld, D. A. Grishina, and W. L. Vos, *Experimental probe of a complete 3D photonic band gap,* Opt. Express **28**:2683-2698 (2020).

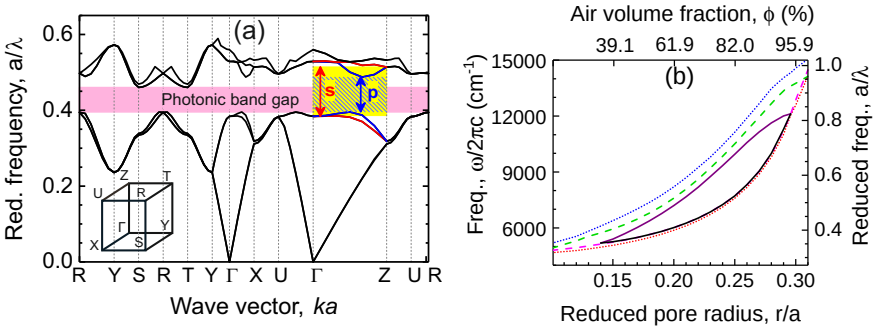

Figure 5.1: (a) Band structures calculated for an inverse woodpile photonic crystal for $r/a = 0.19$ and relative permittivity $\varepsilon_{Si} = 11.68$. The abscissa is the wave vector in the 1st Brillouin zone (see inset). The experimentally relevant ΓZ high-symmetry direction is enlarged for clarity. The ΓZ stop gaps for s and p-polarized light are indicated by the yellow and hatched bars, respectively. The p-polarized bands are shown in blue and s bands in red [111]. The pink bar is the 3D photonic band gap. Band structure calculated by R. Nair. (b) The ΓZ stop gaps and 3D photonic band gap as a function of the reduced pore radius r/a, with the corresponding air volume fraction as the top abscissa. The solid curves are the edges of the 3D band gap. The ΓZ stop gap edges are shown as the blue and red dotted curves (p-polarization) and the green and magenta dashed curves (s-polarization). The left ordinate is for a lattice parameter $a = 680$ nm.

5.1 Introduction

Completely controlling the emission and the propagation of light simultaneously in all three dimensions (3D) remains a major outstanding target in the field of Nanophotonics [19, 20, 25, 146, 147]. Particularly promising tools for this purpose are 3D photonic crystals with spatially periodic variations of the refractive index commensurate with optical wavelengths. The photon dispersion relations inside such crystals are organized in bands, analogous to electron bands in solids [57, 148] see, for example, Figure 5.1(a). When light waves inside a crystal are Bragg diffracted, directional energy gaps – known as stop gaps – arise for the relevant incident wavevector. When the stop gaps have a common overlap range for all wavevectors and all polarizations, the 3D nanostructure has a photonic band gap.

Thanks to extensive efforts in nanotechnology, great strides have been made in the fabrication of 3D nanostructures that interact strongly with light such that they possess a 3D complete photonic band gap [66, 149–151]. Remarkably, however, it remains a considerable challenge to decide firstly whether a 3D nanostructure has a *bona fide* photonic band gap functionality or not, and secondly to assess how broad such a band gap is, which is critical for the robustness of the functionality. It is natural to try to probe the photonic band gap via its influence on the DOS and LDOS by means of emission spectra or time-resolved emission dynamics of emitters embedded inside the photonic crystal [114, 152–154]. However, such experiments are rather difficult for several practical reasons,

that notably involve the emitter's quantum efficiency [155], the choice of a suitable reference system [156], and finite-size effects [157].

Alternatively, the presence of a gap in the density of states may be probed by transmission or reflectivity [116, 118, 158–171]. In such an experiment, a peak in reflectivity or a trough in transmission identifies a stopband in the real and finite

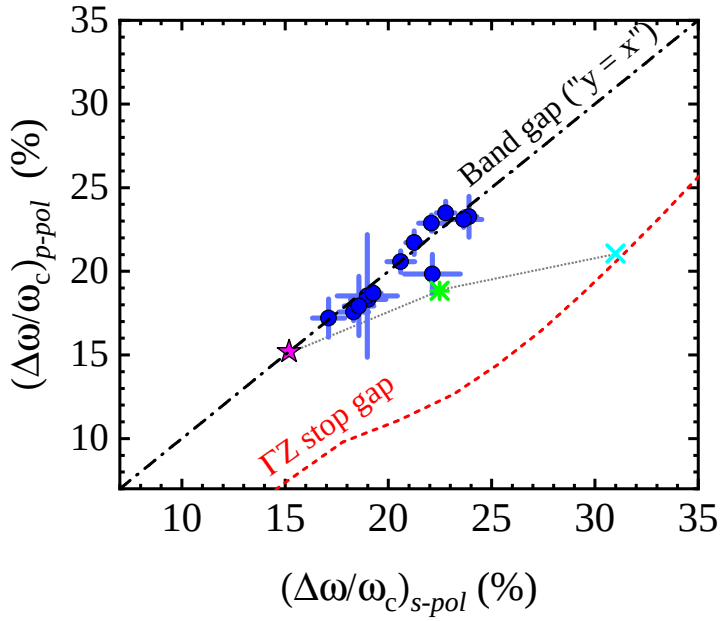

Figure 5.2: Parametric plot of relative stopband width for p-polarization versus relative stopband width for s-polarization measured with NA = 0.85 at the same position on crystals with a range of volume fractions (blue circles). Black dashed-dotted line is the linear "y=x" dependence characteristic of the 3D photonic band gap. The red dashed curve pertains to the ΓZ stop gap, as obtained from band structures. The cyan cross and green asterisk are numerical results for normal incidence (NA = 0) and angle-averaged (NA = 0.65) stopbands for $r/a = 0.19$, respectively, and the magenta star is the band gap width simulated for a finite-thickness crystal with $r/a = 0.19$ that are connected by the gray dotted line as a guide to the eye [111].

crystal that is interpreted with a directional stop gap in the dispersion relations. By studying the 3D crystal over a sufficiently large solid angle, one expects to see a signature of a 3D photonic band gap. While reflectivity and transmission are readily measured, such probes suffer from two main limitations. One technical impediment is when a reflectivity or transmission experiment samples a too small angular range to safely assign a gap, whereas a broader range would reveal band overlap. The second class of impediments includes possible artifacts related to uncoupled modes [172, 173], fabrication imperfections, or unavoidable random disorder, all of which may lead either to erroneously assigned band gaps ('false positive') or to overlooked gaps ('false negative'). To date, these issues are

addressed by supplementing reflectivity or transmission experiments with theoretical or numerical results and deciding the presence of a band gap and its width from such results. Theory or numerical simulations, however, always require a model for the photonic crystal's structure and the building blocks inside the unit cell. Such a model is necessarily an idealization of the real crystal structure and thus misses essential features. For instance, crystal models are often taken to be infinitely extended and thus lack an interface that fundamentally determines reflectivity or transmission features [111]. Or unavoidable disorder is not considered, whereas a certain degree of disorder may completely close a band gap [174]. Or the crystal structure model lacks random stacking (occurring in self-organized structures) which affects the presence and width of a band gap [175]. Thus, when the ideal model differs from the real structure, the optical functionality of the crystal differs from the expected design for reasons that are far from trivial to identify [176]. Therefore, the goal of this chapter is to find a purely experimental identification of a photonic band gap that is robust to artifacts as it avoids the need for modeling.

To arrive at a purely experimental probe of the band gap, we exploit the fact that a 3D photonic band gap is a common gap for both polarizations at all wave vectors in the Brillouin zone simultaneously, *cf.*, Figure 5.1(a). In an experimental situation, sampling as many wave vectors as possible corresponds to sampling an as large as possible numerical aperture NA, in which case the observed stopband widths for s and p-polarized light will be equal. Hence, in a parametric plot of the p-polarized stopband width versus the s-stopband width, the resulting data point is on the straight line ("y = x") through the origin, as illustrated in Figure 5.2. Conversely, in the limit of a very small aperture (NA $\downarrow$ 0) one samples a gap for only one wave vector, such as the high-symmetry ΓZ stop gap shown in Figure 5.2. Since directional stop gaps are polarization sensitive, as is apparent from Figure 5.1, in the parametric plot in Figure 5.2 the corresponding data clearly deviate from linear behavior. Therefore, the proposed probe of a 3D photonic band gap consists of the following three steps:

1. Measure polarization-resolved reflectivity with a high numerical aperture;

2. Parametrically plot the widths of the s versus the p-polarized stopbands;

3. Verify how close the measured result approaches the band gap limit.

In this chapter, we experimentally realize such a probe. In addition we add a 4th point, namely, we track the stopband widths versus volume fraction to obtain many parametric data points that all agree with the band gap expectation. In the process, our method is validated by the very good agreement between stop band widths measured as a function of volume fraction and theoretical results for the photonic band gap. Our purely experimental approach is robust and pertains to any crystal structure, including inverse opals and direct woodpiles, as well as aperiodic band gap structures [177], since no *a priori* assumption is made about the sample structure or any other property.

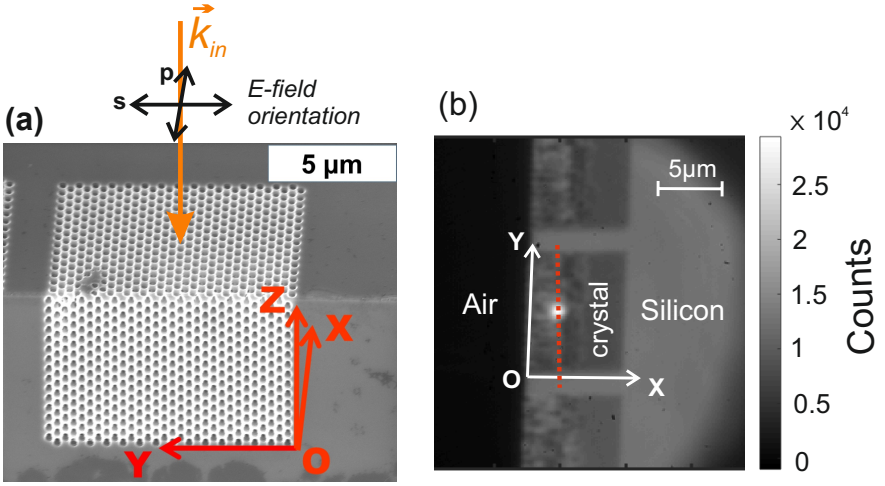

Figure 5.3: (a) Scanning electron microscopy (SEM) image of the edge of the silicon beam with a cubic 3D inverse woodpile crystal in perspective view. The crystal has lattice parameters $a = 680$ nm in the Y-direction, and c in the X and Z-directions with $c = a/\sqrt{2}$. Top: The incident light cone is centered around the wave vector $\mathbf{k}_{\text{in}}$ in the ΓZ direction. The polarization is shown: light is p-polarized when the incident E-field is parallel to the X-directed pores, and s-polarized when the incident E-field is perpendicular to the X-directed pores. (b) Image of the xy-surface of one of the 3D inverse woodpile crystals taken with the IR camera in the optical setup with near infrared LED illumination, with two partly visible neighboring crystals below and above. The bright spot on the crystal is the focus of the incident light from the supercontinuum source filtered by the monochromator. The dotted red line shows the position scan of the focus across the crystal as shown in Figure 5.5.

5.2 Sample and experiment

5.2.1 3D photonic crystals

We study 3D inverse woodpile photonic crystals made of silicon described in chapter 2. A calculated band struture of a perfect infinite crystal is shown in Figure 5.1 (a). In our experiments, the axis of the incident light cone is centered on the ΓZ high symmetry direction of the crystals. Figure 5.1(a) shows that several bands have s or p-polarized character following the assignment of Devashish *et al.* [111]. This Bloch mode polarization indicates the mode symmetry properties while being excited with either s or p-polarized light incident from a high-symmetry direction (here the Z-direction). Figure 5.1(a) also shows that the relative bandwidth of the ΓZ stop gap, gauged as the gap width $\Delta\omega$ to mid-gap ω_c ratio, is wider for s-polarized light ($\Delta\omega/\omega_c = 36.5\%$) than for p-polarized light ($\Delta\omega/\omega_c = 27.6\%$), which is reasonable since in the former case the electric field is perpendicular to the first layer of pores so that light scatters more strongly from this layer. For the diamond-like inverse woodpile structure, the ΓZ high-symmetry direction is equivalent to the ΓX high-symmetry direction, and

thus also their opposite counterparts *viz.* $-\Gamma Z$ and $-\Gamma X$ [111, 118].

In our experiments, the axis of the incident light cone is centered on the ΓZ high symmetry direction. Figure 5.1(a) shows that several bands have s or p-polarized character following the assignment of Devashish *et al.* [111]. This Bloch-mode-polarization assignment indicates the mode symmetry properties while being excited with either s or p-polarized light incident from a high-symmetry direction (here the Z-direction). Figure 5.1(a) also shows that the relative bandwidth of the ΓZ stop gap, gauged as the gap width $\Delta\omega$ to mid-gap ω_c ratio, is wider for s-polarized light ($\Delta\omega/\omega_c = 36.5\%$) than for p-polarized light ($\Delta\omega/\omega_c = 27.6\%$), which is reasonable since in the former case the electric field is perpendicular to the first layer of pores so that light scatters more strongly from this layer. For the diamond-like inverse woodpile structure, the ΓZ high-symmetry direction is equivalent to the ΓX high-symmetry direction, and thus also their opposite counterparts *viz.* $-\Gamma Z$ and $-\Gamma X$ [111, 118].

Figure 5.1(b) shows the ΓZ stop gaps for s and p polarization as a function of pore radius r/a, as well as the photonic band gap [118]. An increasing pore radius corresponds to an increasing air volume fraction, hence to a decreasing effective refractive index. All gap centers shift to higher frequencies which makes sense, since a gap center frequency ω_c is equal to $\omega_c = \frac{c_0}{n_{\text{eff}}}.k_{\text{BZ}}.G$ [18, 66], with c_0 the speed of light (not to be confused with the lattice parameter c), n_{eff} the effective refractive index of the photonic crystal [178], and G a structure factor [57]. The 3D photonic band gap exists within the broad range $0.14 < r/a < 0.29$ with a maximum width at $r/a = 0.245$, as reported earlier [107, 109]. When comparing the stop gaps and the 3D photonic band gap, we note that all lower edges nearly overlap, which is robust as a function of pore radius (r/a), and which is a convenient yet coincidental feature of inverse woodpile crystals that we exploit to validate the volume fraction that we determine by optical means.

5.2.2 Experiment

The reflectivity measurements are done by sending and collecting tunable broadband light through a high numerical aperture NA = 0.85 objective lens (see Chapter 2 for details). The NA corresponds to a large collection solid angle of 0.95π sr. All reflectivity measurements are done for two orthogonal polarization states of the incident light, namely s (electric field transverse to X-directed pores) and p (electric field parallel to X-directed pores), as defined in Figure 5.3(a). To verify the reproducibility of our experiments (both the fabrication methods and the optical measurements), we include in this chapter data obtained with an older setup on an older silicon bar. Since several crystals on this bar have been characterized by traceless X-ray tomography [176], the results on these crystals validate the optical method described below to determine the pore radius.

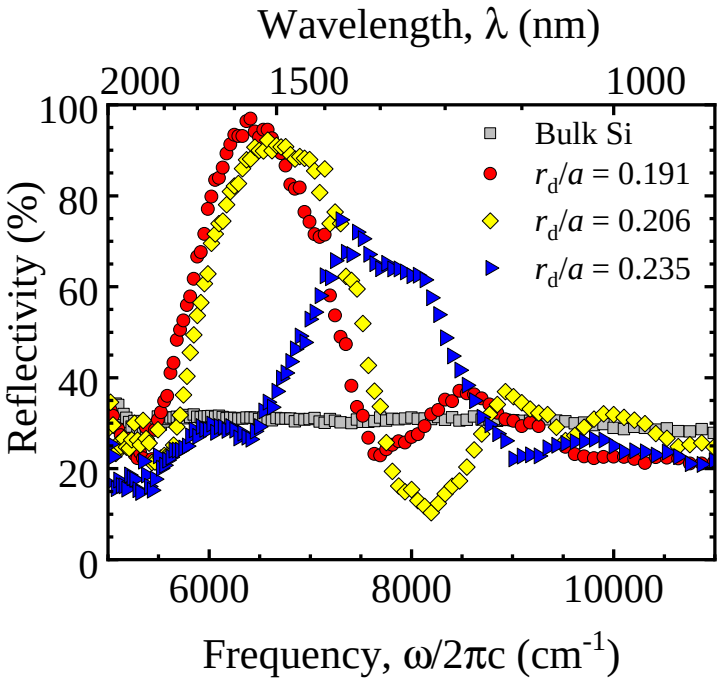

Figure 5.4: Reflectivity spectra of three different 3D photonic crystals with three designed pore radii $r_d = 130, 140$ and 160 nm ($r_d/a = 0.191, 0.206, 0.235$) (red circles, yellow diamonds and blue triangles, respectively). The stopbands appear at different frequency ranges. The gray squares represent reflectivity from bulk Si on the beam away from the crystals.

5.3 Results

5.3.1 Reflectivity and stopband

Figure 5.4 shows reflectivity spectra measured on three 3D crystals with different designed pore radii $r_d = 130, 140, 160$ nm, as well as on the Si substrate. The constant reflectivity $R = 30.6 \pm 1.3\%$ of the substrate agrees well with the Fresnel reflectivity of 31% expected for bulk silicon at normal incidence [179]. Intense reflectivity peaks with maxima of $R_m = 96\%$ and 94% are measured on the crystals with pore radii $r_d = 130$ nm and 140 nm, respectively. A slightly lower maximum reflectivity of 70% observed for the $r_d = 160$ nm crystal is caused by the Si etching process that seems to produce smoother pores at smaller radii. Our observations are consistent with recent numerical results that perfect silicon inverse woodpile crystals with a thickness of only three unit cells reflect 99% of the incident light [111]. Our results are also consistent with 95% reflectivity measured by Euser *et al.* on a direct silicon woodpile that was only one unit cell thick [180]. We surmise that the current maximum reflectivity are higher than those of [112, 118] due to improved nanofabrication and improved optics.

The reflectivity peaks correspond to the stopband and are associated with the main ΓZ stop gap centered near $a/\lambda = 0.45$ in Figure 5.1(a). Figure 5.4 also shows that the center of the stopband shifts to higher frequencies with increasing pore radius, which qualitatively agrees with the calculated behavior shown in Figure 5.1(b).

The stopband width is taken as the full width at half maximum (FWHM) of the reflectivity peak, as it gives a robust measure of the stopband [181]. The baseline of the peak is taken as the minimum reflectivity in the long-wavelength limit at frequencies below the stopband, with the standard deviation in this frequency range as the error margin. Similarly, the maximum reflectivity is taken as the mean in a narrow frequency range around the peak, with the standard deviation in this range taken as the error margin. The errors are propagated into the estimates of the edges at half maximum of the peak.

5.3.2 Position-dependent stopband

It is well-known from structural studies such as scanning electron microscopy on cleaved crystals [101] and from non-destructive X-ray tomography [176] that the radius of etched nanopores varies slightly around the designed value with depth inside the crystal due to the nature of the etching process [101]. By comparing the lower edge of the measured stopband with the calculated stop gap (*cf.* Figure 5.1(b)), we obtain an estimate of the local average pore radius r at the position X, Y, Z of the optical focus: $r(X, Y, Z)$. In this comparison we profit from the feature in the band structures of inverse woodpile crystals that the lower edges of both the band gap and of the stop gap are nearly the same, hence the determination is robust to the interpretation which gap is probed.

For the three spectra in Figure 5.4, we derive the pore radii to be $r/a = 0.190 \pm 0.001, 0.195 \pm 0.001,$ and 0.228 ± 0.002, respectively, which agrees very well with the design ($r_d/a = 0.191,\ 0.206,\ 0.235$), where the small differences are

attributed to the depth-dependent pore radius discussed above. Note that these radii are estimated only on the probing location on the crystal, where the errors depend on steepness of the lower edge of the stopband. We note that since the probing direction is perpendicular to the X-directed pores in the crystals, the derived pore radii are effectively those of the pores that run in the X-direction.

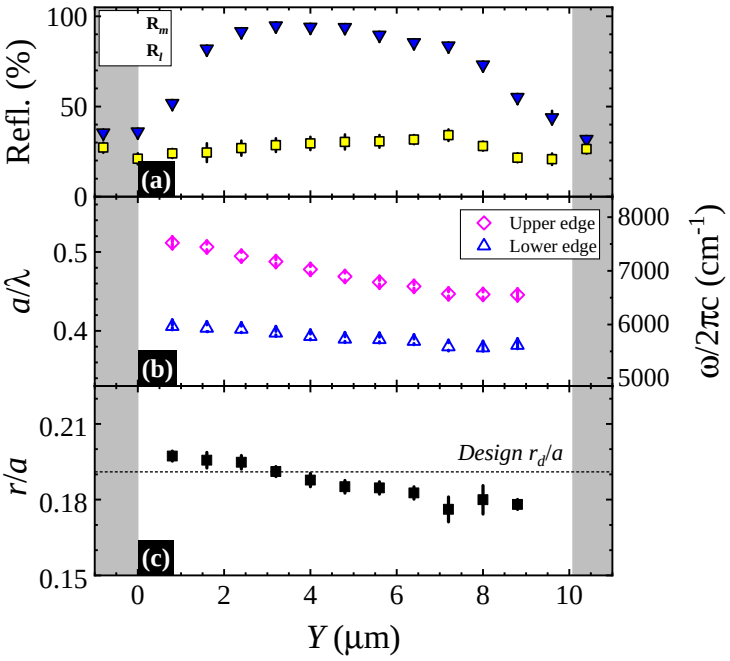

Figure 5.5: Reflectivity measured as a function of Y-position on a crystal with design pore radius $r_d = 130$ nm (or $r_d/a = 0.191$), measured with p-polarized light. (a) Maximum peak reflectivity (R_m) and minimum reflectivity below the stopband (R_l). (b) Upper edges (magenta diamonds) and lower edges (blue triangles) of the stopband obtained from the half heights of the reflectivity peaks. The right ordinate is absolute frequency for a lattice parameter $a = 680$ nm. (c) Relative radii r/a derived by comparing the lower edge of the stopband with data shown in Figure 5.1(b). The grey areas at $Y < 0$ μm and $Y > 10$ μm indicate bulk silicon outside the crystal with a constant reflectivity near 31%.

Next, we collect reflectivity spectra while scanning the focus across the crystal surface. Since we then effectively scan the pore radius r, we expect to scan the stopband in response. As an example, Figure 5.5 shows the results of a Y-scan across one of our crystals with design pore radius $r_d = 130$ nm ($r_d/a = 0.191$). The position scan of the focus across the crystal is shown as the red dashed line in the camera image shown in Figure 5.3(b). While scanning the Y-position, a slight excursion occurred in the X-direction from $x = 2.8$ μm to 3.2 μm due to imperfect alignment of the silicon beam axis with the vertical axis of the translation stage. From each collected spectrum, we derive the peak

reflectivity R_m and the minimum reflectivity below the stopband R_l as shown in Figure 5.5(a). Inside the crystal there is substantial difference between R_m (up to $R_m = 94.8\%$) and R_l, hence the crystal's reflectivity peaks are well-developed. Near the crystal edges ($Y = 0$ μm and 10 μm) the difference between R_m and R_l rapidly decreases and both tend to about 31% since the focused light here is reflected by bulk silicon.

Figure 5.5(b) shows the edges of the measured stopband as a function of Y. Between $Y = 0$ μm and 10 μm the lower edge shifts down from 5950 to 5550 cm^{-1} and the upper edge shifts down from 7550 to 6550 cm^{-1}. In other words, both the center frequency of the stopband and its width decrease with increasing Y as a result of the variation of the pore radii with position. The redshift of the stopband frequencies is likely caused by the small excursion along X, since the radius of the X-directed pores decreases with increasing X. Additionally, the pore radius might have an inhomogeneity along the Y direction, since we observe similar consistent shift of the stopband on other crystals measured on the same silicon beam, see for example Figure 7.5.

By comparing the measured lower edges in Figure 5.5(b) with the theoretical gap maps shown in Figure 5.1(b), we derive the local pore radius $r(X, Y, Z)$ in the crystal that is plotted versus Y-position in Figure 5.5(c). The resulting $r(X, Y, Z)/a$ is seen to vary from 0.197 to 0.176 about the design pore radius $r_d/a = 0.191$. Therefore, we can now combine all position-dependent data to make maps of stopband centers and stopband widths as a function of the pore radius.

5.3.3 Gap map from experiments

We have applied the procedures described in sections 5.3.2 and 5.3.1 to reflectivity measured on many crystals and we also collected spectra during Y-scans on two crystals to verify the consistency of all observations. From all collected reflectivity spectra, both s and p polarized, the lower and upper stopband edges are extracted, and are mapped as a function of r/a in Figure 5.6. The lower edge data form a continuous trace from reduced frequency $a/\lambda = 0.38$ at $r/a = 0.17$ to $a/\lambda = 0.50$ at $r/a = 0.245$. The data match well with the theory, which is obvious since we used the lower edge to estimate r/a from the measured spectra.

The upper edge data form a continuous trace from reduced frequency $a/\lambda = 0.42$ at $r/a = 0.17$ to $a/\lambda = 0.64$ at $r/a = 0.245$. It is remarkable that the upper edge data for both s and p-polarized light mutually agree very well, especially for pore radii $r/a > 0.21$. This observation implies that the measured stopband is representative of the 3D photonic band gap that is polarization insensitive, as opposed to a directional stop gap that is polarization sensitive.

In comparison to theory, at pore radii $r/a < 0.21$ the upper edges are in between the theoretical upper edges of the band gap and the p-polarized edge of the directional stop gap. At larger radii ($r/a > 0.21$), all measured upper edge data are near the theoretical upper band gap edge and differ from the stopband edges. This observation adds support to the notion that the structure-dependent stopbands represent the 3D photonic band gap, rather than a directional stop

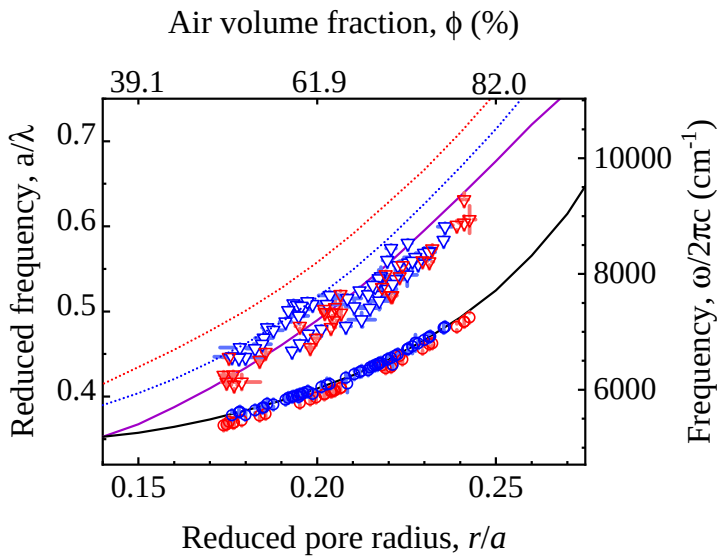

Figure 5.6: Evolution of the stopband edges versus pore radius. The red and blue triangles represent upper edge of the stopband for s and p-polarized light respectively. The red and blue circles represent the lower edge of the stopband for s and p polarized light. The stopband edges are inferred from the reflectivity peak measured on 11 crystals. The solid lines indicate the edges of the photonic band gap. The upper edge of the ΓZ stop gap for s and p polarized light are plotted as the red and blue dotted curves, respectively. The right ordinate is absolute frequency for a lattice parameter $a = 680$ nm.

gap.

We plot in Figs. 5.7(a) and 5.7(b) the relative stopband width (gap to mid-gap ratio) as a function of r/a as derived from the lower edges. The large number of data in Figure 5.7(a) shows that the width of the s-polarized stopband increases up to $r/a = 0.2$ before saturating up to $r/a = 0.24$. The s-polarized data for an older Si beam agree well with our data, except for an outlier at $r/a = 0.24$. For these older crystals, the pore size r/a was obtained from a direct structure-determining method, namely X-ray tomography [176]. Consequently, the good agreement with the newer crystals whose pore radii are determined from the stop band edge validates the optical determination of the pore radii. Moreover, since the optical experiments on the older crystals employed a different setup, the good agreement indicates that both the old and the new reflectivity spectra are representative, even though the old setup yields lower maximum reflectivity. All data are close to the theoretical prediction for the width of the 3D photonic band gap and lie distinctly below the theoretical width of the stop gap.

Figure 5.7(a) also shows results of s-polarized reflectivity simulated for a *finite* inverse woodpile crystal with $r/a = 0.19$ [111], namely of a directional stopband, of an angle-averaged stopband (for a range of angles relevant for a reflecting

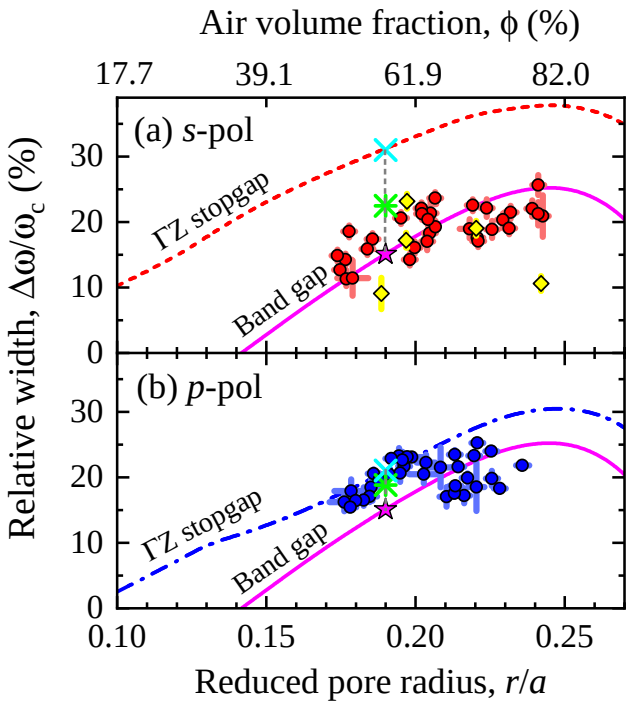

Figure 5.7: Measured relative stopband width (gap width to midgap, $\Delta\omega/\omega_c$) versus r/a for (a) s-polarized (red circles), (b) p-polarized (blue circles) input light. Yellow diamonds in (a) are data from an older Si beam. The cyan crosses, green asterisks, and magenta stars are numerical results for normal incidence, angle-averaged stopband, and complete band gap at $r/a = 0.19$, respectively for both polarizations [111]. The dashed red and dash dotted blue curves represent the width of the ΓZ stop gap obtained from band structures for s and p polarized light, respectively. The magenta solid curve is the 3D photonic band gap from band structures.

objective with $NA = 0.65$), and of an omnidirectional band gap. With increasing aperture, the simulated stopband becomes narrower. From the comparison, it is apparent that our data match best with the width of the 3D photonic band gap.

Figure 5.7(b) shows the p-polarized stopband widths versus pore radius. At pore radii $r/a < 0.21$, the stopband widths are in between the theoretical bandwidths of either the directional stopgap or the omnidirectional band gap. At larger radii ($r/a > 0.21$), the measured stopband widths match better with the theoretical width of the band gap than with the stop gap width. From p-polarized finite-crystal simulations done at $r/a = 0.19$ [111], we conclude that the bandwidths of the directional stop gap, of the angle-averaged stopgap, and of the band gap are near to each other, hence it is difficult given the variations in our data to discriminate between either feature. Considering the s and p-polarized stopband widths jointly, we again find a much better agreement with the 3D photonic band

gap than with the directional stop gap.

The conclusions from Figs. 5.6 and 5.7 are based on the agreement between measurements on one hand, and simulations and theory on the other hand. The latter invokes an idealized structural model, for instance, pores as infinite perfect cylinders which neglect pore tapering, or roughness. Therefore, these conclusions do not represent a purely experimental probe of a 3D band gap.

5.3.4 Experimental probe of the photonic band gap

At this point, we are in a position to complete the model-free experimental probe of a 3D photonic band gap, consisting of the (3+1) step plan outlined in section 5.1. Up to here, we have discussed the collection of polarization-resolved reflectivity spectra using a large NA (step #1). Next, we parametrically plot the width of the measured *p*-polarized stopband versus the width of the *s*-polarized stopband that is shown in Figure 5.2 (step #2). In order to avoid systematic errors due to the position-dependence of the stopbands, we select data where spectra were measured for both polarizations on the same position on a crystal.

Figure 5.2 shows that for *s*-polarized stopband widths between $\Delta\omega/\omega_c = 17\%$ and 24%, the corresponding *p*-polarized stopband width increases linearly, and also from 17% to 24%. Such a strictly linear increase agrees with the expectations for a 3D photonic band gap even without modeling, since a 3D band gap entails a forbidden gap for *both polarizations simultaneously* [20] (steps #3 and #4). In the case of the alternative hypothesis that the measured stopbands correspond to directional ΓZ stop gaps, the parametric trend would be nonlinear and clearly differ from the diagonal. Since this trend obviously does not match with our data, we reject this hypothesis.

In order to validate our proposed method, we discuss results obtained from numerical simulations on a finite-size inverse woodpile photonic crystal by Devashish *et al.* [111]. The simulations were done for inverse woodpiles made from silicon with a pore radius $r/a = 0.19$, and the incidence angle was varied over a wide range. Several situations were simulated, namely single-direction incidence from a high-symmetry direction (ΓX or ΓZ) with effectively zero numerical aperture (NA = 0). Secondly, simulations were done for incidence over a large range of angles corresponding to a reflecting objective with NA= 0.65 (see [117, 118]). Thirdly, the 3D photonic band gap was studied. The simulations reveal that when the NA is increased, the corresponding data move towards the diagonal. Figure 5.2 shows that the data point for the directional stop gap agrees very well with the stop gap curve and is far from the diagonal band gap line. The data point simulated for the NA= 0.65 objective is in between the stop gap and the band gap curves, as expected since these curves effectively represent low and high NA. Finally, the data point for the band gap agrees well with the band gap prediction and not at all with the stop gap curve. Therefore, the numerical aperture $NA = 0.85$ used here is apparently sufficient to probe the omnidirectional photonic band gap.

5.4 Discussion

It is widely agreed that the fabrication of 3D nanostructures necessary for photonic band gap physics is challenging [17, 159–161]. Consequently, since the detailed 3D nanostructure critically determines the band gap functionality, it is important to have a non-destructive verification of the functionality. We propose that the practical band gap probe method presented here fills a gap by providing relatively fast feedback on a newly fabricated band gap material. In a holistic approach, one would not only verify the functionality but also the 3D band gap material since the latter usually aids the understanding of the functionality, especially in complex situations where the function differs from the designed one. While studying the detailed 3D structure of a nanostructure is non-trivial, successful methods have been reported using X-ray techniques, notably small-angle X-ray scattering [182–184], X-ray ptychography [185], or traceless X-ray tomography [176].

The optical analysis discussed in section 5.3.2 provides a relatively straightforward and non-destructive way to study details of the 3D band gap material, whereas in section 5.3.4 we present a purely experimental probe of the 3D photonic band gap without the need to idealize the crystals as is traditionally done in numerical simulations. Since this experimental probe is independent of the crystal structure, it is readily applicable to other types of 3D photonic band gap materials such as inverse opals, direct woodpiles, and even to non-periodic materials [75, 159, 177]

So far, the optical analysis discussed in section 5.3.2 was specific to the inverse woodpile structure studied here [105]. In order to generalize our analysis to other classes of photonic band gap crystals, such as inverse opals, direct woodpiles, and even non-periodic ones [177], it is useful to realize that a varying pore size in an inverse woodpile structure corresponds to the tuning of the filling fraction and thus of the effective refractive index [178], both of which pertain to all other classes of photonic band gap structures. Both the filling fraction and the effective index are readily generalized to other 3D photonic band gap crystals. For instance, in inverse opals the filling fraction of the high-index backbone is known to vary with preparation conditions [183], hence this can be used as a tuning knob. In direct woodpile crystals, the filling fraction is notably tuned by varying the width of the high-index nanorods [75, 159], and similarly in hyperuniform structures [177]. It is therefore that the top abscissae in Figs. 5.6, 5.7, and 5.1(b) have been generalized to the effective refractive index. Therefore, the stopband width versus the effective index (as in Figure 5.7) or the p-polarized stopband width versus the s-polarized one also pertain as probes to other classes of band gap structures, and thus serve as experimental probes of the 3D photonic band gap in such other structures.

We foresee that a practical probe of 3D photonic band gaps will boost their applications in several innovative fields. For instance, recent efforts by the Tokyo and Kyoto teams have demonstrated the use of 3D photonic band gap crystals as platforms for 3D photonic integrated circuits [75, 186]. In the field of photovoltaics that is of considerable societal interest, the use of 3D photonic band gap

crystals is increasingly studied to enhance the collection efficiency by means of various kinds of photon management [68, 69, 187]. A robust band gap is necessary to realize embedded point or line defects in a 3D photonic crystal to effectively control emission and 3D waveguiding applications [74, 163]. It is an essential feature of a 3D photonic band gap crystal to have a gap in the density of states, which in turn corresponds to the density of vacuum fluctuations. Therefore, quantum devices embedded inside a 3D band gap crystal are effectively shielded from quantum noise [78], including quantum gates that manipulate qubits for quantum information processing.

5.5 Conclusion

In this chapter, we present a purely experimental probe of the 3D band gap in real three-dimensional (3D) photonic crystals, without the need for theoretical or numerical modeling that invokes idealized and even infinite photonic crystals. As an exemplary structure, we study 3D inverse woodpile crystals made from silicon. For the probe, we exploit the fact that a 3D photonic band gap is a common gap for both polarizations at all wave vectors in the Brillouin zone simultaneously. The band-gap probe consists of three main steps: 1) measure polarization-resolved reflectivity with a high numerical aperture; 2) parametrically plot the widths of the *s* versus the *p*-polarized stopbands; 3) verify how close the measured result approaches the band gap limit. In addition, a 4th point describes how to track the stopband widths versus volume fraction to obtain many parametric data points that all agree with the band gap expectation.

In an experimental situation, sampling as many wave vectors as possible corresponds to sampling an as large as possible numerical aperture NA, in which case the observed stopband widths for *s* and *p*-polarized light will be equal. Hence, in a parametric plot of the *p*-polarized stopband width versus the *s*-stopband width, the resulting data point is on the straight line ("y = x") through the origin.

In the process, we have collected position and polarization-resolved reflectivity spectra of multiple crystals with different design parameters with a large numerical aperture and observed intense reflectivity peaks with maxima exceeding 90% corresponding to broad (up to 24%) stopbands, typical of high-quality crystals. We have produced a gap map for the experimental stopband width versus pore radius, which agrees much better with the predicted 3D photonic band gap than with a directional stop gap. From a parametric plot of *s*-polarized versus *p*-polarized stopband width, we obtain a strictly linear dependence, in agreement with the 3D band gap and at variance with the directional stop gap. This parametric plot is a purely experimental probe of the 3D band gap and can be readily applied to other types of 3D photonic band gap crystals. Such a practical probe provides a fast evaluation of the advanced nanofabrication required for 3D photonic crystals. Moreover, the fast probe of 3D band gaps will stimulate practical applications of band gaps, notably in 3D silicon nanophotonics and photonic integrated circuits, photovoltaics, cavity QED, and quantum information processing.

Appendix 5

5.A Variation of pore size with depth

In this appendix, the detailed experimental analysis of estimating the local pore radii of the crystals is presented.

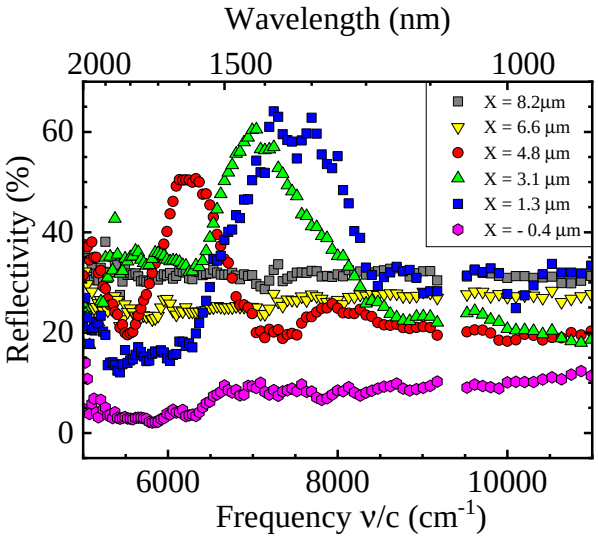

Figure 5.8: Reflectivity spectra for several X-positions indicated on the legend for the 3D structure with design pore radius $R_d/a = 0.235$. The stopband appears at different frequency ranges at different spatial positions, indicating non-uniformity of the crystal.

Figure 5.4 shows that the center of the stop band blue shifts with increasing pore radius. This frequency shift of the stop band qualitatively agrees with the behavior of the calculated stop gap shown in Figure 5.1(b). By comparing the lower edge of the measured stop band with that of the calculated stopgap, we estimate the pore radii of the three crystals to be $R/a = 0.190 \pm 0.001, 0.195 \pm 0.001,$ and 0.228 ± 0.002, respectively, which agrees very well with the design $R_d/a = 0.190, 0.205,$ and 0.235.

We first investigate how spatially uniform the crystal is, by means of position-resolved reflectivity measurements. For this purpose, we perform reflectivity measurements along one of the etching direction of the pores on a crystal with $R_d/a = 0.235$. The focus of the light beam is scanned in the X-direction across the crystal from the crystal- air edge until it reaches the bulk silicon on the other side of the crystal. At every $\Delta X = 0.22$ μm step, a reflectivity spectrum is recorded. Thus we collected 40 spectra across and beyond the 8 μm wide crystal. A small selection of representative spectra are shown in Figure 5.8. Near the edge of the crystal the overall reflectivity is very low, without any peak. The size of the focus is about 2 μm and therefore, when $X < 2$ μm, the light leaks

by the edge of the crystal resulting in a lower overall reflectivity. Interestingly, depending on the position, the stop band appears at different ranges of wave numbers. This observation immediately implies that the fabricated crystals are not uniform. The shifting of stop band with position can be used to reveal the source of non-uniformity of the crystal. According to the results reported in Ref. [109], the fabrication deviation that significantly influences the photonic band gap is tapering of the pore radius. Therefore we can relate the stop band to the possible variation of pore radius inside the crystal. Next we proceed for a detailed investigation of the stop band as a function of position to have a better understanding of the fabricated crystals.

Since the etch mask used to fabricate the pores in silicon is well defined, the lattice constants are reliable with the design values. But the radii and uniformity of the pores with depth can vary depending on the etching process and time. In this experiment, the X-directed pores are perpendicular to the direction of measurement, while the Z-directed pores are along the direction of measurement. Therefore, while performing position dependent measurements as a function of X, the optical response of the crystal is primarily influenced by the X-directed pores. Hence to explain the position dependent behavior of the crystal, we relate the change in the observed stop band to change in radius of the pores along X.

From the reflectivity spectra taken at different X positions, we obtain the relative widths of the stop band as the ratio of the FWHM of the reflectivity peak and its center frequency ($\Delta\omega/\omega_c$), shown in Figure 5.9(a). In Figure 5.9(b), the maximum reflectivity (R_m) and the average reflectivity below the stop band (R_l) are plotted as a function of X. R_l essentially gives the Fresnel reflectivity in the low-frequency limit due to the effective refractive index of the porous silicon crystal. The X values in the abscissa indicate the position of the center of the focus on the crystal surface, with a focus diameter less than 2 μm.

We distinguish several X ranges on the crystal according to the trend of the stopband width with X. In region **I** (0 μm $< X <$ 1.5 μm) the stop band width is broad and nearly constant. In this region, the focal spot is not entirely on the crystal and part of the light is lost due to leakage around the crystal edge. Hence the overall reflectivity increases as X increases. In region **II** (1.5 μm $< X <$ 3.2 μm), stop band is consistent and broad with high maximum reflectivity. In this region R_l still increases with X which indicates increase of the effective index, possibly due to a small change in radius of the pores. In region **III** (3.2 μm $< X <$ 6.3 μm) the stop band narrows steadily with X, which implies that the pore radius gradually decreases in this region. But there is still a high number of 3D unit cells that provide the high maximum reflectivity until around $X = 5$ μm. In region **IV** (6.3 μm $< X <$ 7.1 μm) the stop band is extremely narrow ($< 5\%$) and closes at $X > 7$ μm. R_m decreases and R_l increases, and they merge after the gap closes since there is no more photonic structure along the measurement direction. In region **V** (7.1 μm $< X <$ 8 μm) the stop band vanishes which implies that the X-directed pores ends there and hence the crystal is no longer three dimensional. R_m and R_l have the same value in this region. The lower reflectivity value in this region with respect to that of the bulk silicon is because the pores along the Z-direction make the effective index less than that

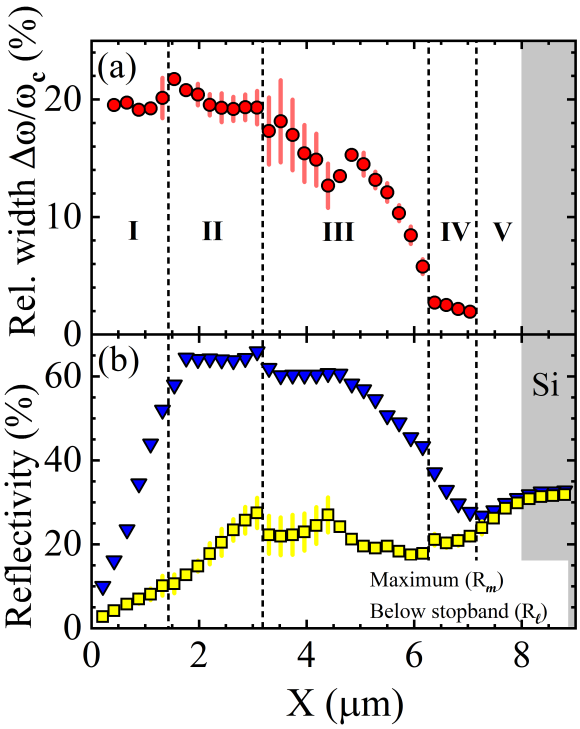

Figure 5.9: (a) The relative width of the stopband inferred from reflectivity spectra as a function of X. (b) The measured maximum reflectivity of the stop band and the minimum reflectivity below the low frequency edge of the stop band as function of X. The vertical dashed lines separate regions on the crystal according to the position of the 2μm focal spot on the surface.

of bulk silicon. At about $X = 8$ μm the bulk silicon starts which can be identified from the overall constant reflectivity of 30%.

From the above observations, we can abstract a model of the uniformity and quality of the photonic crystal. To quantify the quality of the crystal as a function of position, we define reflectivity contrast ΔR as

$$\Delta R \equiv \frac{R_m - R_l}{R_m + R_l} \tag{5.1}$$

Figure 5.10 shows the reflectivity contrast versus the corresponding stop band width measured at the different locations along X on the crystal. The symbols of four different colors correspond to data from the regions **I**, **II**, **III** and **IV**. This plot clearly distinguishes data points from different parts of the crystal, which can be directly linked to the uniformity and quality of the photonic crystal. From this figure, it can be stated that a broad stop band also corresponds to a high reflectivity in the stop band. It is remarkable to note that only from the optical

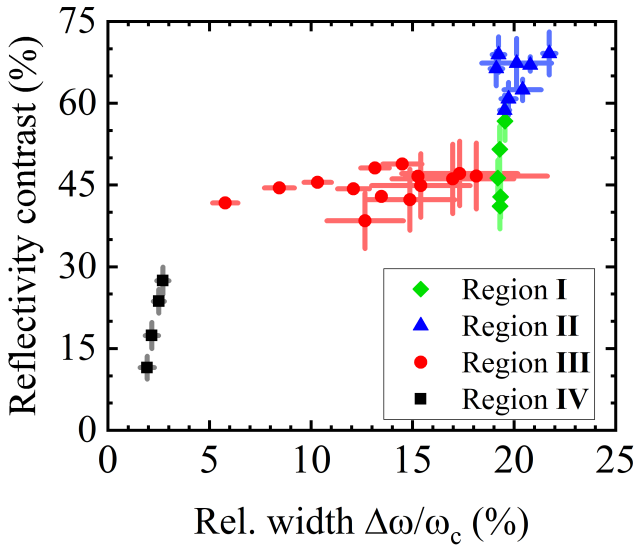

Figure 5.10: Maximum reflectivity R_m with low-frequency reflectivity R_l subtracted, and normalized to the average reflectivity versus the relative bandwidth. The different symbols correspond to data points from different regions on the crystal as mentioned in Figure 5.9.

response of the crystal, we now know that the X-directed pores are fairly uniform near the edge of the crystal, and start to get tapered beyond 3 μm. In this optical setup, the best photonic behavior of the crystal is realized in region **II**, given by the blue triangles in Figure 5.10. Region **II** is uniform, highly reflecting with a broad stop band and therefore is our area of interest to perform more reflectivity measurements.

Chapter 6

Spatially shaping waves to penetrate deep inside a forbidden gap

It is well known that waves with frequencies within the forbidden gap inside a crystal are transported only over a limited distance - the Bragg length - before being reflected by Bragg interference. Here, we demonstrate how to send waves much deeper into crystals in an exemplary study of light in two-dimensional silicon photonic crystals. By spatially shaping the wavefronts, the internal energy density probed via the laterally scattered intensity is enhanced at a tunable distance away from the front surface. The intensity is up to $100\times$ enhanced compared to random wavefronts, and extends as far as $8\times$ the Bragg length, which agrees with an extended mesoscopic model. We thus report a novel control knob for mesoscopic wave transport that also pertains to other kinds of waves.

6.1 Introduction

Completely controlling wave transport is a key challenge that is essential for a large variety of applications. For instance, classical transport of acoustic waves has enabled sensing, ultrasound imaging and navigation [188, 189]. In the quantum regime, control over electron and spin transport has led to major advances

The content of this chapter has been published in: R. Uppu, M. Adhikary, C. A.M. Harteveld, and W. L. Vos, *Spatially Shaping Waves to Penetrate Deep inside a Forbidden Gap,* Phys. Rev. Lett. **126**:177402 (2021) *and* K. Wright, Physics 14, s53 (2021)

in the operation of nanoelectronic devices [190–192]. In photonics, control over light transport has been exploited both in the classical and quantum domain, which has led to rapid advances in science and technology such as solar cells, quantum light sources, optical memories, and micro to nanoscale storage cavities [70, 193–197].

An important tool in wave control is to exploit gap formation as a result of periodic and aperiodic symmetry. The long-range periodic order leads to a band structure in the dispersion relations of the waves. Forbidden frequency ranges, stop gaps, emerge in the band structure as a result of interference between the incident waves and Bragg diffracted waves [198, 199]. Bragg interference causes incident waves with a frequency in the stop gap to be exponentially attenuated, with a characteristic length scale called the Bragg length L_B, as is shown in Figure 6.1. The existence of gaps has led to exciting applications such as control of spontaneous emission, efficient light harvesting devices, and biosensing [200, 201].

Real crystals feature unavoidable disorder resulting in broken symmetry due to, *e.g.*, thermal motion and phonons in atomic crystals at finite temperature, quantum motion down to zero temperature, or unavoidable structural disorder in assembled photonic or phononic structures [202]. The disorder gives rise to new channels for wave transport due to the multiple scattering, which is typically uncontrolled and thus detrimental for the applications mentioned above. In a specific realization of a crystal, the microscopic configuration of disorder is fixed [203] and hence the disorder-induced channels do not in themselves offer new control. In disordered media without gaps, however, it is known that spatially shaping the phases of incident waves serves to set interferences between channels that represent new control: wavefront shaping [55, 204, 205].

Therefore, in this chapter, we set out to demonstrate the tunable control of wave transport in real crystals. By spatially shaping the incident wavefronts as illustrated in Figure 6.1, we steer the waves with frequencies within a gap to any desired location deep inside the crystal. The waves reach a remarkable depth of no less than $8 \times L_B$ with more than $30\times$ intensity enhancement. Remarkably, the shaped intensity at $5 \times L_B$ in the crystal is even $10\times$ higher than the incident intensity I_0 in *absence of wave shaping*, instead of being Bragg attenuated as is usual in periodic media. In our approach, we employ wavefront shaping of light in photonic crystals that can be readily extended to electrons and acoustic waves, where analogous techniques have been demonstrated [206, 207].

Our results stand out from the literature on wavefront shaping and disordered media in the following aspects:

1. In photonic crystals, the energy density distribution within the crystal is completely fixed by the Bragg length. Our introduction of wavefront shaping radically modifies this distribution that increases the depth to which light can be steered, thereby increasing the functional volume of the crystal (see Figure 1.4). Modifying the energy density distribution is also new compared to disordered media that lack frequency gaps.

2. In disordered media, the intensity inside the medium after wavefront shaping is everywhere less than at the front surface before wavefront shaping.

Here, we strikingly observe that upon wavefront shaping to a location inside the crystal, the intensity within the photonic crystal is even greater than at the front surface measured for an uncontrolled wavefront.

3. We identify that Bragg interference - typical of periodic media including quasicrystals - take on a novel role in mesoscopic physics that of reducing the number of channels for wave transport.

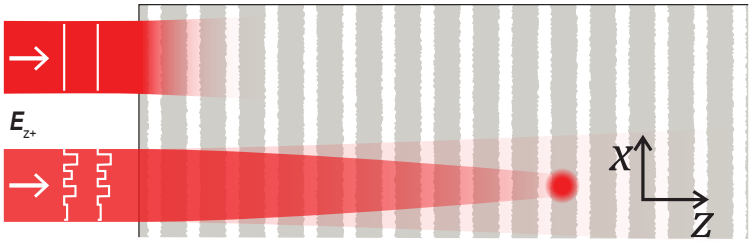

Figure 6.1: Schematic of wave transport in a 2D photonic crystal consisting of pores with unavoidable disorder. At frequencies in the gap, light is quickly Bragg attenuated; by shaping the wavefronts, light is transported much deeper into the crystal.

6.2 Experiment

As exemplary waves, we study the propagation of light in two-dimensional (2D) photonic crystals that consist of large periodic arrays of pores etched in a silicon wafer [100, 103], see Figure 6.2(a). The pores are made by CMOS-compatible methods, employing deep reactive ion etching through an etch mask. The lateral yz-extent of the 2D crystal is 10×10 mm^2 at the center of the wafer, much larger than the expected Bragg and scattering length scales. The fabricated pores are about 6 μm deep, sufficient for the focus to easily fit within the crystal, see Figures 2.1(b) and 6.3. The wafers are cleaved in the xy-plane to expose the 2D photonic crystal to the incident light along the ΓK high-symmetry direction [103].

We use the versatile experimental setup described in chapter 2 to perform optical wavefront shaping on silicon nanostructures. In the optical setup, the wavefront of the spectrally filtered collimated beam is programmed employing a phase-only reflective spatial light modulator SLM, see Figure 6.3. The wavefront-programmed light is imaged to the back focal plane of the large numerical aperture ($NA = 0.85$) infrared apochromatic objective lens M1. The light reflected from the crystal is collected by the same objective. The laterally scattered light from the yz-plane of the crystal is collected using a long working distance apochromatic objective M2 ($NA = 0.42$). Light collected by either M1 or M2 can be imaged to an InGaAs camera for aligning the incident beam. The inset in Figure 6.3 shows the image captured in reflection, where the air, photonic crystal, and the unstructured silicon regions can be clearly separated. The bright spot in the center of the photonic crystal is the focused laser beam when a constant

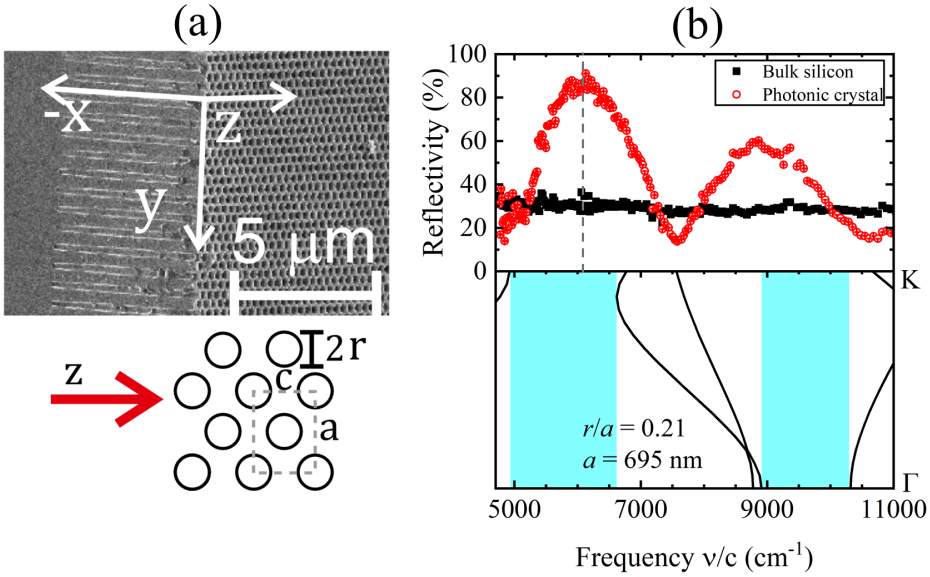

Figure 6.2: (a) Top: scanning electron microscope image of a two-dimensional (2D) photonic crystal. The lower half shows the 2D array of pores in the yz-plane, and the upper half shows the xy cleavage plane with 6 μm deep pores (see 5 μm scale bar). Bottom: yz-plane with the centered rectangular crystal with lattice parameters $a = 695$ nm and $c = a/\sqrt{2}$. The pores have a diameter $2r = 290$ nm (or $r/a = 0.21$). Light is incident in the z-direction, corresponding to the ΓK high-symmetry direction, see Figure 2.1(c). (b) Reflectivity measured on the photonic crystal (open circles) for TE-polarized light, compared to a reference of a silicon wafer (filled squares). The prominent photonic crystal reflectivity peaks match well with the stop gaps in the calculated band structures, highlighted by cyan. The measured stopbands are broader than the calculated stop gaps likely because the intermediate bands have unusual dispersion that typically causes high reflectivity [173]. The dashed line highlights the frequency near the gap center where many steering experiments were performed.

phase ($\phi = 0$) was programmed on the SLM. Given the large pore depth (8 μm) of the nanopores of the photonic crystal, several diffraction-limited spots fit within a given incident area on the crystal. Therefore, in contrast to earlier wavefront shaping on 2D disordered waveguides that utilized one-dimensional wavefront shaping [208–210], we illuminate a circular area ($d = 8$ μm, see Figure 6.3).

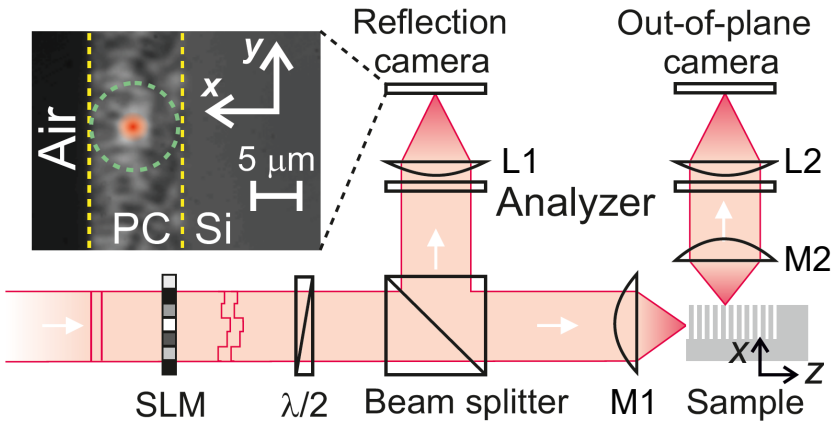

Figure 6.3: The same setup shown in Figure 2.6, highlighting the necessary parts for this chapter. Linearly polarized light from a tunable source is directed via a spatial light modulator (SLM) onto the sample through microscope objective M1. The incident polarization is tuned using the half-wave plate ($\lambda/2$). Light reflected by the crystal is imaged onto an infrared camera using the same objective and lens L1 (f= 500 mm). A long working distance objective (M2) images the laterally scattered light onto an infrared camera using lens L2 (f = 500 mm). Broadband linear polarizers are used to analyze the reflected and the laterally scattered light. The inset shows the image taken on the camera in reflection. The bright spot in the center (highlighted in red) is the focused coherent light with a uniform phase pattern on the SLM.

6.3 Results

6.3.1 Broadband reflectivity

Reflectivity from the 2D crystal was measured following the procedures described in chapter 2. TE-polarized reflectivity spectra shown in Figure 6.2(b) reveal two prominent peaks that are identified to correspond to two stop gaps in the calculated band structures. We estimate the Bragg lengths for both gaps from the photonic strength S using the relation $L_B = \lambda/(\pi S)$ [211], where the strength is defined to be $S \equiv \Delta\nu/\nu$ [18]. In the two stop bands at the center frequencies $\nu/c = 6250$ cm^{-1} and 9000 cm^{-1}, respectively, the photonic strength is $S = 0.25$ and 0.19, respectively, corresponding to Bragg lengths $L_B = 2.0$ μm that are nearly the same for both stop gaps [212, 213].

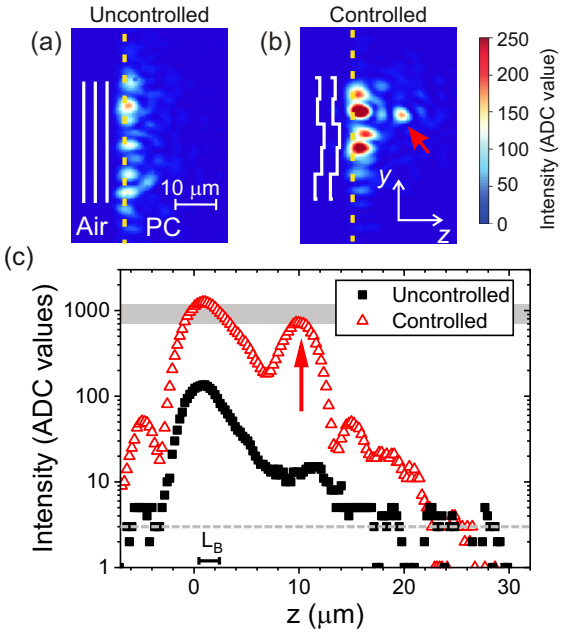

Figure 6.4: Camera images of the laterally scattered light ($\nu/c = 6250$ cm^{-1}) with (a) an uncontrolled and (b) the controlled wavefront. The red arrow points to the target location for steering the light, which exhibits as a bright spot. (c) The integrated intensity in a 5 pixel high (yz-plane) strip around the target location shows a clear increase in the intensity at the target depth of 10 μm. The dashed grey line indicates the detector's dark counts. The grey band is the intensity expected at z = 10 μm upon wavefront shaping as predicted by our model.

6.3.2 Wavefront shaping inside the photonic gap

To demonstrate controlled transport of waves, we tune the frequency of the incident light to the center of the first stop gap at $\nu/c = 6250$ cm^{-1} ($\lambda = 1600$ nm). The SLM was initialized with a phase pattern of 340 segments (each grouped from 32×32 pixels) within the beam diameter, each assigned a random phase within $[0, 2\pi)$. The size of the segment was chosen to limit the illuminated area on the xy-plane of the sample to be confined within the photonic crystal. The image of the laterally scattered light collected using M is shown in Figure 6.4(a), which shows a rapid decay of light into the crystal. The input edge of the crystal is clearly discernible as the bright speckles (also marked by the dashed line).

We target a spot at a depth of 10 μm - or $5 \times L_B$ - in the crystal and sequentially change the phase of each segment on the SLM to maximize the intensity at the chosen spot. Figure 6.4(b) shows the image of the laterally scattered light at the end of the iteration over all the segments. A distinct and bright focus is clearly observed at the targeted location, thereby demonstrating the first ever steering of waves inside a crystal, far beyond the Bragg length. Figure 6.4(c)

shows the intensity around the targeted spot before and after steering the light, which shows $\approx 100\times$ higher intensity with controlled transport.

In literature, it is common to characterize the quality of wavefront shaping by an enhancement E_W that gauges the intensity increase at the target position [214, 215]. The enhancement is commonly defined as $E_W \equiv I_{opt}/\langle I_r \rangle$, where I_{opt} is the optimized intensity in the target spot and $\langle I_r \rangle$ is the intensity at the same spot that was ensemble-averaged over 100 random incident wavefront patterns. The intensity of the laterally scattered light is proportional to the energy density of the light that has scattered to a depth z in the crystal. The enhancement at the target location inside the crystal is substantial, namely $E_W = 65 \pm 5$. Remarkably, in Figure 6.4 we observe that the intensity at the target spot (depth $z_{opt} = 5 \times L_B$) *after steering* is even $10\times$ greater than the intensity at the front surface ($z = 0$) *before steering* (that is, light incident with an unoptimized wavefront), in contrast to traditional Bragg attenuation of waves inside any periodic medium. The enhancements observed here are a key highlight of the steering of the waves, which takes advantage of the multiple scattering of waves in the crystal due to the unavoidable deviations from perfect periodicity [79]. The multiple scattering of waves gives rise to new channels for wave transport within the crystal even inside the stop gap (that pertains to Bloch waves). By spatially shaping the phases of the incident waves with the feedback defined by the energy density deep inside the crystal, we selectively enhance the coupling of incident energy to the transport channels associated with multiple scattering. This selective coupling of energy into multiple scattering transport channels results in the penetration of waves deeper inside the crystal. This remarkable increase in intensity at the optimized position leading to an increase in the internal energy density is in contrast to all prior wavefront shaping experiments in random media, which highlights the new physics of light transport unveiled here.

6.4 Discussion

Using wavefront shaping, we explore the achievable depth inside the photonic crystal at which the intensity could be enhanced. Intuitively, this depth depends on surface losses and the incident energy density on the front surface, since the energy density decays exponentially with depth, thereby reducing the number of transport channels. Figure 6.5 shows the depth-dependent intensity enhancement E_W at the center of the stop gap (at $\nu/\mathrm{c} = 6250\ \mathrm{cm}^{-1}$). The error bars represent standard deviations of E_W measured at 8 different spatial locations along y at the same depth z. An enhancement E_W in excess of 80 was achieved at depths up to 10 μm, corresponding to $5 \times L_B$. At a depth of more than $8 \times L_B$, the measured enhancement is $E_W = 20$. We postulate that the decreasing enhancement E_W with depth arises from surface losses that prevent the waves from reaching greater depths in the photonic crystal.

To interpret the intensity enhancement deep inside the crystal, we propose a new model that extends mesoscopic physics typical of disordered media[1] [205,

[1] Also analogy to the communication channels is described by Miller [216].

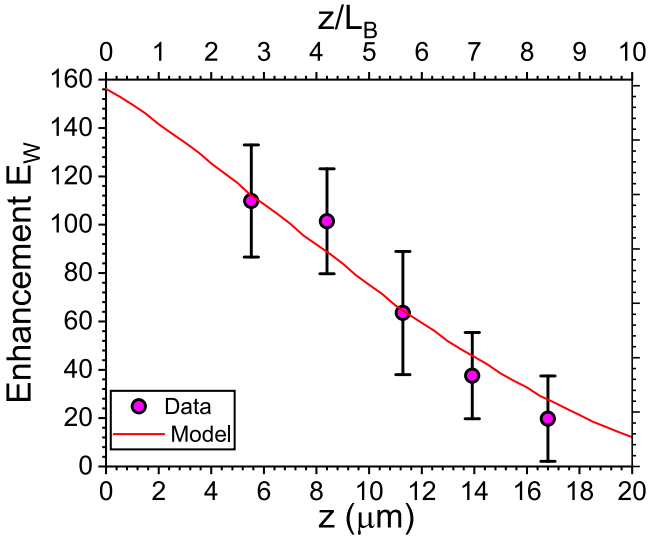

Figure 6.5: Measured wavefront shaping enhancement E_W versus penetration depth z into the crystal at a frequency at the center of the stop gap $\nu/c = 6250$ cm^{-1}. The calculated enhancement in a system with a synergistic interplay of the Bragg interference and random multiple scattering in a real photonic crystal agrees well with the measurements.

217] to periodic crystals[2]. The disorder-assisted multiple scattering of light inside the crystal is described using a transmission matrix T over the N transport channels. The transmission matrix T can be decomposed as

$$T = UDV^{\dagger} \tag{6.1}$$

where U and V are unitary matrices of size $N \times N$ and D is a diagonal matrix with values τ drawn from the Dorokhov-Mello-Pereyra-Kumar (DMPK) distribution.

The reflectivity measurements of the photonic crystal, *cf.* Figure 6.2(b), were used to extract the fraction of light transmitted into the crystal. We neglect the material absorption of waves within the crystal given the near-zero absorption coefficient of silicon in the telecom wavelength range. The wavefront shaping enhancement E_W is proportional to the largest eigenvalue of the matrix T, with the proportionality constant set by the wavefront shaping method [55]. Typically, the local energy density within a disordered slab decreases approximately linearly with depth inside the slab. In contrast, we observe from Figure 6.4(c) that the local energy density decays exponentially with depth inside the crystal. We interpret this exponential attenuation to arise from the Bragg interference at frequencies within the stop gap. The Bragg interference results in a reduction of the number of transport channels with increasing depth inside the crystal, where disorder induced scattering becomes dominant. This allows us to extend

[2]The details of the model can be found in Appendix 6.C of this chapter.

mesoscopic transport models developed for disordered media in the presence of absorption [218, 219] to periodic systems.

Mathematically, the reduction in the number of transport channels is modeled as a truncation of the transmission matrix T, *i.e.*, a reduced matrix size $M < N$. The reduced number of channels M with increasing depth in the crystal is modeled as

$$M(z) = N(1 - \alpha z) \tag{6.2}$$

where α is an amplitude attenuation constant [220]. The depth-dependent enhancement $E_W(z)$ is the maximum eigenvalue of the truncated transmission matrix. At a given α and N, we employ a numerical algorithm to generate an ensemble of random transmission matrices and compute the depth-dependent enhancement E_W. The fit to the measured enhancement E_W is shown in Figure 6.5 with $\alpha = (0.05 \pm 0.002)\ \mu\text{m}^{-1}$ and $N = 300$, and is seen to agree very well with the data. To put our model in perspective, the number of control parameters (segments) on the SLM is $N_{exp} = 340$, which agrees remarkably well with the number of channels in the model. The deviation could arise from the non-uniform intensity incident at each segment of the SLM due to the Gaussian profile of the incident beam. From an independent measurement of the attenuation within the crystal, we extract the intensity extinction length $\ell_{\text{ext}} = 6.5 \pm 0.2\ \mu\text{m}$ (see appendix of this chapter) arising from the multiple scattering of waves. The intensity attenuation length and the amplitude attenuation constant are related as $\ell_{\text{ext}} = 1/\sqrt{\alpha}$. From the fit to E_W in Figure 6.5, we estimate $\ell_{\text{ext}} = 4.9 \pm 0.5\ \mu\text{m}$, which is smaller than the measured value. The underestimation of ℓ_{ext} is expected as the model effectively accounts for the attenuation due to the Bragg interference and multiple scattering of waves within the crystal, while the measured value is primarily due to the multiple scattering of waves. We note that ℓ_{ext} extracted from the model fits is greater than the Bragg length, as the disordered-induced transport within the crystal is polarization-averaged, whereas the Bragg length pertains strictly to TE-polarized light.

6.5 Summary and conclusion

In summary, we have demonstrated controllable enhancement of wave propagation at much greater depths than a Bragg length, even at frequencies within a band gap [221]. We take advantage of transport channels that are introduced in the crystal by unavoidable disorder, and address these by spatially shaping the wavefronts. The large depth to which waves are enhanced, even within a gap, broadens the range of applications feasible with photonic band gap crystals, both 2D and 3D. From the outset, photonic band gaps have been pursued for their radical control over spontaneous emission [153, 222], lasing [195], shielding of vacuum noise for qubits [78], and for ultimate 3D waveguiding [74, 186]. Based on our observations and modeling, we project that studies with embedded emitters could resolve the density of states around the gap of the real crystal [80, 223]. Furthermore, light can be reconfigurably steered to resonant and functional features, including Anderson localized states [9] or 'Cartesian' light states [97], that

are otherwise hidden inside a complete 2D or 3D photonic band gap.

Recently, combinations of gaps and tailored disorder are enjoying a fast-growing attention [224], notably in phononic and photonic quasicrystals [225], and hyperuniform [177, 226] and bio-mimetic structures [227]. It is intriguing to speculate whether our crystals may reveal extremal transmission near a Dirac point and pseudo-diffuse behavior as predicted by Sepkhanov *et al.* on 2D crystals [228]. Therefore our results open new avenues to increased wave control in many different classes of metamaterials [229, 230].

Appendix 6

In this appendix, we discuss how we determine the extinction length in the 2D photonic crystals. We first discuss the spatial resolution of the setup that is an important ingredient in the estimation of the extinction length. In part 6.C, we describe the derived model for wavefront shaping enhancement in periodic structures with random disorder.

6.A Spatial resolution of the laterally scattered light

Structural disorder is known to result in a new length scale for wave transport called the extinction length ℓ_{ext} that statistically quantifies the strength of the disorder [212, 213]. The extinction length of light in the two-dimensional silicon photonic crystal was characterized by imaging the $yz-$plane of the sample on a InGaAs camera with an effective optical magnification of 125×. A constant phase of 0 rad was displayed on the SLM to focus the light on the sample to a diffraction-limited spot. The images of the laterally scattered light were captured at regular intervals (in 2 nm wavelength steps) as the frequency of the incident light was tuned from 6100 cm^{-1} to 10000 cm^{-1}. The intensity images were integrated along the height, corresponding to the $y-$axis. This depth-dependent intensity inside the crystal exhibits an exponential decay convolved with a Gaussian instrument response function, which determines the optical resolution.

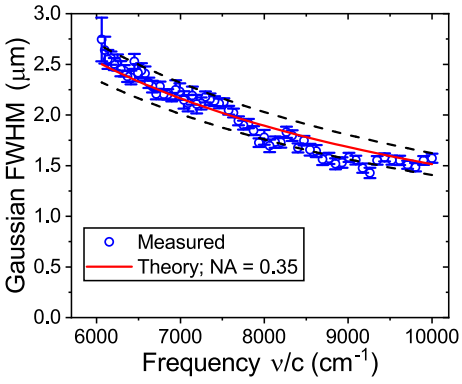

Figure 6.6: The estimated Gaussian full width at half-maximum (FWHM) using the lateral-scattered images captured using the camera is shown versus input light frequency. We model the measurements to extract the collection aperture of the setup to be NA = 0.35. The dashed curves are the 95% confidence interval of the model.

Since the precise estimation of the resolution of the lateral scattering imaging setup is important in correctly estimating the extinction length, we first turn to this issue. The peak at the input edge of the photonic crystal was modeled with a Gaussian to extract the resolution. Figure 6.6 shows the Gaussian full-width at half-maximum (FWHM) extracted from the fit. We extract the numerical aperture for the collection arm to be NA = 0.35, which compares well with the nominal collection objective aperture NA = 0.42. It is reasonable that the effective aperture is slightly less than the nominal one, in view of some shadowing

by the focusing objective at the input plane (the xy-plane).

6.B Extinction length of light in two-dimensional photonic crystals

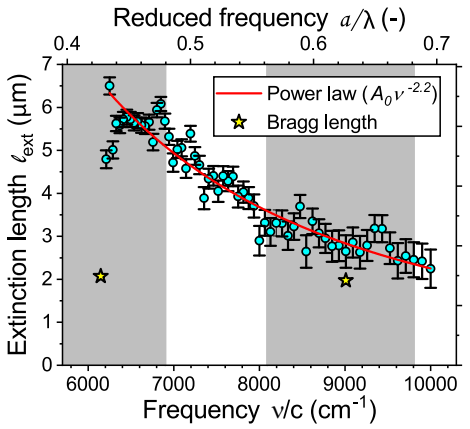

Figure 6.7: The estimated extinction length $\ell_{ext\perp}$ of TE-polarized light propagating inside the 2D photonic crystal is plotted over a range of frequencies. The frequency-dependence of the extinction length closely follows earlier theoretical predictions of a power-law dependence with an exponent of -2.2. The gray shaded regions correspond to the measured stop gaps. The Bragg lengths L_B as estimated from the photonic strength S are marked as stars at the centers of the stop gaps.

Using the data from Figure 6.6, we are now in a position to deconvolve the laterally scattered light with the corresponding Gaussian function. We illuminate the crystal with TE-polarized light and capture images of the laterally-scattered light with an analyser crossed with the incident polarization. The cross-polarized measurement configuration enables us to isolate the multiple scattered light as Bragg reflectance from the crystal is sensitive to the polarization [103]. The deconvolved data were matched to a single exponential model to extract the extinction length $\ell_{ext\perp}$. The subscript $\perp$ indicates that we collect laterally-scattered light that is cross-polarized to the incident. In contrast, if we collect only the co-polarized laterally-scattered light, the extracted extinction length is dominated by the Bragg length of the crystal. Figure 6.7 shows the extracted $\ell_{ext\perp}$ (circles) as a function of frequency for TE-polarized light incident on the photonic crystal. The error bars correspond to the 95% confidence bound of the fitted extinction length. The extinction length decreases with increasing frequency, as expected, from about $\ell_{ext\perp} = 6$ μm at the lowest frequencies in the first order stop band to about $\ell_{ext\perp} = 2.5$ μm at the highest frequency beyond the second stop band.

To put these observations in perspective, we compare to theoretical work. Koenderink *et al.* predicted a power-law dependence of the extinction length on the frequency [79]. For two-dimensional photonic crystals made of infinite long cylinders, the predicted dependence outside the stop gap is $\ell_{ext} = A_0\nu^{-2.2}$, where A_0 is a scaling parameter that depends on the degree and nature of the disorder. We adjusted only the scaling parameter to the measured data in Figure 6.7 and observe that the power-law dependence on frequency agrees very well with the measurements. The observed deviation at low frequencies in the first stop gap is

attributed to our choice of limiting the model to a single exponential to describe the intensity inside the crystal. Even in the cross-polarized collection, Bragg interference inside the stop gap leads to additional extinction of light with the Bragg length L_B as the characteristic length scale, depicted as star markers in Figure 6.7. The two length scales arising from multiple scattering and Bragg length would thus require a bi-exponential model to the intensity attenuation within the crystal, which is at this time difficult to significantly model, given the limited dynamic range and signal-to-noise ratio of the data. At frequencies in the range of the second stop gap, the Bragg length is close to the extinction length, and thus it is not sensible to try to fit the data with a bi-exponential model.

The error bars of the enhancements E_W in Figure 6.5 have nearly equal size, independent of the absolute magnitude of the enhancement. We surmise that the enhancement E_W is Gaussian distributed, typical of independent observations, with a standard deviation given by the observed error bar. Conversely, the enhancement does not match with Poisson statistics, where the error bar would grow with magnitude.

6.C Model of WFS enhancement in the 2D crystal

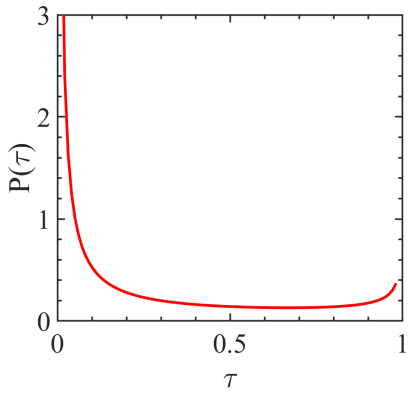

Figure 6.8: Probability density function of transmissions τ obtained from the DMPK theory for average transmission $\langle\tau\rangle = 0.1$ within the photonic gap.

To calculate the transmission matrix T using equation 6.1, we first construct two random unitary matrices U and V by the following method: An $N \times N$ matrix is constructed with complex random variables drawn from a Gaussian distribution. The resulting matrix is then processed by the QR decomposition method to calculate the eigenvalues [231–233]. Then, U and $V^\dagger$ matrices are constructed out of the eigenvalues.

From reflectivity spectra of the crystal, we obtain an average transmission of 10% in the photonic gap. Assuming the transmission inside the photonic gap is due to unavoidable fabrication disorder in the crystal, the transmission values τ are extracted from the DMPK distribution for average transmission of 10% corresponding to up to 90% reflectivity. Originally developed for scaling in the transport of electrons in multimode wires, the DMPK distribution is often used in photonics to describe transmission eigenvalues in disordered photonic media [217, 234–237]. The prob-

ability density from this distribution is expressed as,

$$P_{\mathrm{DMPK}}(\tau) = \frac{\langle\tau\rangle}{(2\tau\sqrt{1-\tau})} \tag{6.3}$$

where $\langle\tau\rangle$ is the mean transmission. The DMPK distribution of transmission for this case is plotted in figure 6.8. The distribution of average transmission $\langle\tau\rangle = 0.1$ shows that most of the transmission values are between 0 and 1, with divergences at $\tau = 0$ and at $\tau = 1$. Using this distribution, we construct a diagonal matrix D using the values of τ from the distribution.

Once we have constructed U, D, and $V^{\dagger}$, we calculate the T-matrix using equation 6.1. The maximum eigenvalue of T corresponds to the maximum possible transmission that channel can accommodate. This means that the maximum possible intensity that can be achieved by WFS is proportional to the maximum of the transmission eigenvalues. As depth z is increased, there are less transmission channels due to surface losses and Bragg interference and therefore, the transmission matrix is truncated using the relation 6.2. Thus, the maximum achievable enhancement from WFS is extracted from the maximum transmission eigenvalue and the number of channels at that depth, and is given by,

$$E_w(z) = \frac{\pi}{4} M(z) T_{\max}, \tag{6.4}$$

where the proportionality constant of $\pi/4$ is used since we use a phase-only WFS algorithm [55]. The attenuation constant α and the number of channels N is estimated by comparing the model with the experimental data, see appendix 6.B.

Chapter 7

Observation of light propagation through a three-dimensional cavity superlattice in a photonic band gap

We experimentally investigate a novel form of light transport in a three-dimensional (3D) photonic band gap. Such light transport is functionalized by the presence of a coupled network of cavities embedded in a photonic band gap crystal with superperiodicity, also called as a superlattice of cavities. We make 3D photonic crystals that possess a 3D band gap in the telecom wavelengths, with an embedded array of point defects. In broadband reflectivity and scattering experiments, we find features that correspond to cavity superlattice modes obtained from band-structure calculations.

7.1 Introduction

It is well-known that fruitful analogies exist between the physics of photons, and the physics of electrons, spins, phonons, and other wave phenomena in condensed matter [22, 25, 31, 212, 238, 239]. A famous example is the analogy between a 3D photonic band gap in a photonic crystal and the electronic band gap in a semiconductor like silicon [20, 57, 240]. The periodic arrangement of high and low index materials in the length scale of the wavelength of light in three dimensions leads to destructive interference of a certain range of wavelength resulting in

the so-called photonic band gap. An analogous energy gap for electrons exists between the conduction states and valence or ground states of semiconductors, known as the electronic band gap.

In semiconductors, electrons with excess energy, for example, those with high thermal energy, in the valence bands overcome the electronic band gap and jump to the conduction band. Doping the semiconductor material by impurity atoms is used to control the conductivity of semiconductors. Thus, a phase transition between conducting and insulating states is achieved in semiconductors by modifying or perturbing their internal structure. Doping of semiconductors with n-type or p-type impurities introduces additional energy levels at bottom of the conduction band or top of the valence band, which are known as donor or acceptor levels [241–244]. Such levels contribute to the controlled conductivity of semiconductors at room temperature. Bound and resonant states within the semiconductor band gap have been also reported [242, 245]. Within the photonic band gap of a photonic crystal, the density of states vanishes, and the crystal is 'insulating', meaning there are no propagating modes. Additional states are introduced inside the photonic band gap by introducing defects, similar to impurity states in semiconductors. It has been known that defects created by adding or removing high index material from a photonic crystal also give rise to additional states within the band gap, called "donor" or "acceptor" modes, respectively [93]. Defect states in 3D photonic crystals lead to many possible applications such as optical nanocavities [246], waveguides [74, 92], miniature lasers [88, 247, 248], and cavity quantum electrodynamics [249, 250]. In this chapter, we present the experimental demonstration of a novel type of light transport in 3D photonic crystals modified with donor-like point defects.

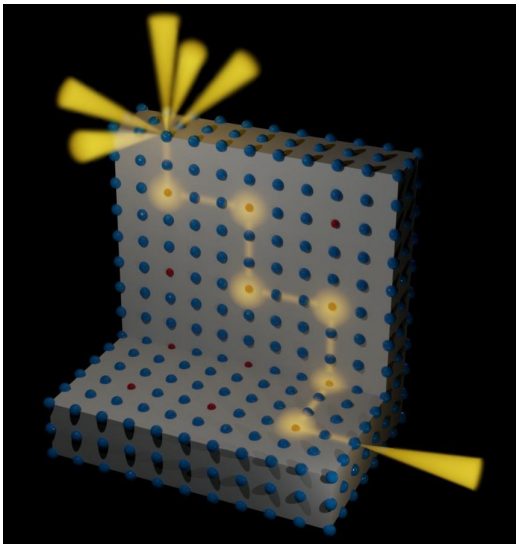

Figure 7.1: An artistic impression of light hopping from one cavity to the neighboring one, as a result of cavity coupling in a superlattice. Light with frequency supported by the superlattice modes incidents on one cavity on the surface (bottom right), takes a certain path through the 3D cavity network and exits the structure from another perpendicular surface (top left) Illustration made by M. Kozon.

An array of point defects in a 3D photonic band gap crystal leads to a network of 3D cavities. When cavities are placed close enough to each other, overlap of their wave functions results in inter-cavity coupling. While light propagation takes place by hopping from one resonant cavity

to another, the underlying photonic band gap shields the cavities from vacuum noise [80]. In 1D, a well-known phenomenon is a CROW (coupled resonator optical waveguide), where an optical resonator is placed in the vicinity of other similar resonators, and light hops from one resonator to another as a result of evanescent coupling [94]. Bayindir *et al.* [95] demonstrated such an array of 1D coupled cavities embedded in a 3D microwave photonic crystal by measuring transmission. Interesting results on 2D arrays of coupled cavities in photonic crystals were presented by Altug *et al.* [96, 251]. However, a superlattice containing 3D cavities in a 3D band gap has not yet been studied experimentally to our knowledge. A recent study has investigated 3D superlattice of cavities embedded in a 3D photonic band gap crystal and demonstrated directional dependence of inter-cavity coupling. The coupling is observed to be stronger along the high-symmetry Cartesian directions and hence the name "Cartesian light" for such unconventional light propagation [97]. Along the Cartesian directions, photons propagate through the band gap crystal by hopping across neighboring cavities as illustrated in the artistic impression in Figure 7.1.

In experimental situations, a signature of cavity resonance in photonic crystals is usually measured through reflection and transmission experiments. In such experiments, one searches for narrow troughs within the reflectivity peak or narrow peaks within the transmission trough that corresponds to the band gap. In the case of 3D superlattice of cavities, light propagation takes place also in the lateral direction in addition to reflection and transmission directions. Hence to search for 3D signature of the cavities, it is more convincing to detect the light that exits the crystal from the lateral direction. In real photonic crystals, both intentional point defects and unavoidable structural disorder [79] contribute to scattering of light. Thus, reflectivity or the laterally transmitted spectra are perturbed due to presence of defects. The challenge in experimental situations is to identify the cavity scattering from a background of random scattered signal, also known as speckle, due to disorder. We measure broadband reflectivity in near infrared range of photonic crystals modified with a superlattice of point defects that act as cavities. The spectra of light scattered in the lateral direction with respect to the incident direction is also measured, which effectively captures part of 3D scattered light by the crystals. From combined position-resolved measurements on two crystals with different spacings between defects, we establish the first-ever experimental detection of coupled and uncoupled cavity modes in a 3D photonic crystal modified with resonant cavities.

7.2 Experiment

We study 3D photonic band gap crystals with periodically repeated point defects that form 3D cavity superlattices that were described in detail in section 2.1.3 of chapter 2. Figure 7.2 shows a scanning electron microscopy (SEM) image of a fabricated inverse woodpile crystal with an array of defects, a cavity superlattice (SL5). The direction of light incident on the crystal and the various directions of light exiting from the crystal are shown with the red arrows.

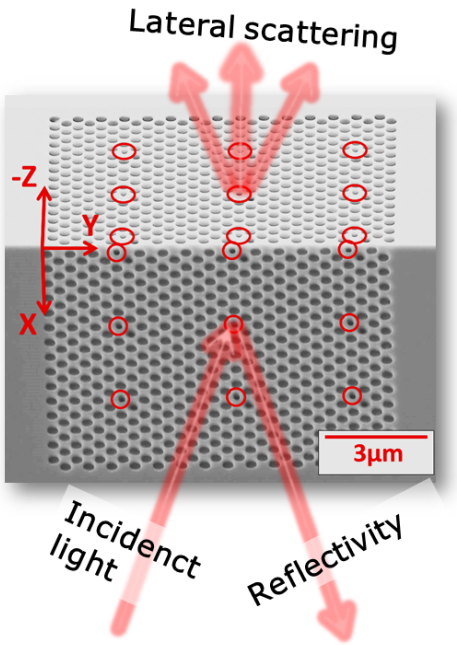

Figure 7.2: Scanning electron micrograph of a superperiodic cavity superlattice embedded in a 3D photonic band gap crystal made of silicon by our group, viewed in the (X,Z)-direction. The inverse woodpile crystal has lattice constants $a = 0.68$ μm in the Y-direction and $c = 0.48$ μm in the X, Z-directions. The designed pore radius is $r = 0.16$ μm for the main nanopores and $r' = r/2 = 0.08$ μm for the defect pores. The superlattice of the point defects has the unit cell with dimensions $5c, 5a, 5c$. The excess silicon at the intersections of these defect pores inside the material form point defects which constitute the superlattice of 3D cavities.

To study the cavity superlattices, we use the setup (see Figure 6.3) described in detail in chapter 2 that simultaneously collects both broadband specular reflectivity to probe the underlying band gap and specular cavity scattering, and light scattered laterally by the cavities in non-specular directions in the NIR range, compatible with silicon. The diameter of the focus is about 1.5 μm at full-width at half maximum, which is smaller than the distance between two neighboring cavities of the crystals. Therefore, in spatial scans across the crystal surface, we probe both on the cavities and away from them. Specularly reflected light is collected by the same objective and directed to an extended range ($0.9 - 2.6$ μm) InGaAs photodiode (PD1), where analyzer A1 is set parallel to the incident polarization. At the same time, the light scattered from the crystal in the lateral $-$X-direction is collected by a second objective and detected by a second InGaAs photodiode (PD2). The analyzer A2 is set perpendicular to the input polarization to collect only the scattered light and suppress incident light or single-scattered light. Separately, we collect spectra from a clean gold mirror to serve as the

reflectivity reference. Spectra collected from a 45°-inclined gold-coated prism surface at 90° serve as the reference for the lateral scattering spectra. On every measurement, we collect a pair of broadband reflectivity and scattering spectra simultaneously in the frequency range 5300 cm^{-1} to 11000 cm^{-1}.

7.3 Results

7.3.1 Probe with *s*-polarized light

Reflectivity and lateral scattering spectra

By moving the sample stage in the Y-direction, the focus is scanned across the crystals with a step size of ≈ 0.4 μm, resulting in about 30 reflectivity and scattering spectra. Figure 7.3 shows two representative reflectivity and lateral scattering spectra, and band structures of superlattice SL5 for two main situations, namely when light is focused onto a defect (a,c), and away from a defect (b,d) [1]. Since the separation between two defects ($\Delta Y = 3.4$ μm) is larger than both the Bragg length ($L_B = 0.2$ μm [111]) and the input beam diameter ($d = 1.5$ μm), it is reasonable that light focused at positions in between defects hardly probes the defects. Therefore spectra collected with the incident beam focused in between cavities effectively correspond to probing the underlying band gap crystal. In each case, we observe an intense and broad reflectivity peak that corresponds to the 3D band gap of the crystal, see also chapter 5. It is remarkable that the introduction of a 3D cavity superlattice in the photonic crystal does not close the band gap, hence potential superlattice modes are confined in the 3D band gap.

To identify reflectivity features in Figure 7.3(a), we plot for comparison the band structure calculated for an infinite inverse woodpile crystal with a superlattice of defects in Figure 7.3(c) with the same frequency range. The band structures were calculated for pore radii corresponding to those obtained at the probing location, with the method from chapter 5 and Ref. [110] [2]. The band structure shows that the cavity superlattice sustains two types of bands inside the 3D band gap, namely flat bands typical of Cartesian light, and dispersive bands in the upper half of the band gap. Recently, an ongoing computational study in our group has shown that lower-dimensional localized modes also exist in such a system, along the line defects created by the defect pores in the crystal and these modes are part of the dispersive bands [252]. Due to the dispersive bands, the band gap of the cavity superlattice structure (see Figure 7.3(a)) is significantly narrower than the original band gap (see Figure 7.3(b)). This is clearly observed in the experimental spectra, where a broad trough near 7800 cm^{-1} coincides with the dispersive bands in the upper half of the original band gap. As a result, the reflectivity peak probed on the defect (see Figure 7.3(a)) is narrower than while

[1] In Figure 7.3(a) the incident focus is close to the middle defect pore on the xy surface, and in Figure 7.3(b) the incident focus is in between the middle and the right most defect pore on the xy surface at $X = 2.5$ μm.

[2] The reason for this procedure is that the pore radii vary across the sample surface, and also vary in depth. Therefore, at every probed location one has to determine a 'local pore radius'.

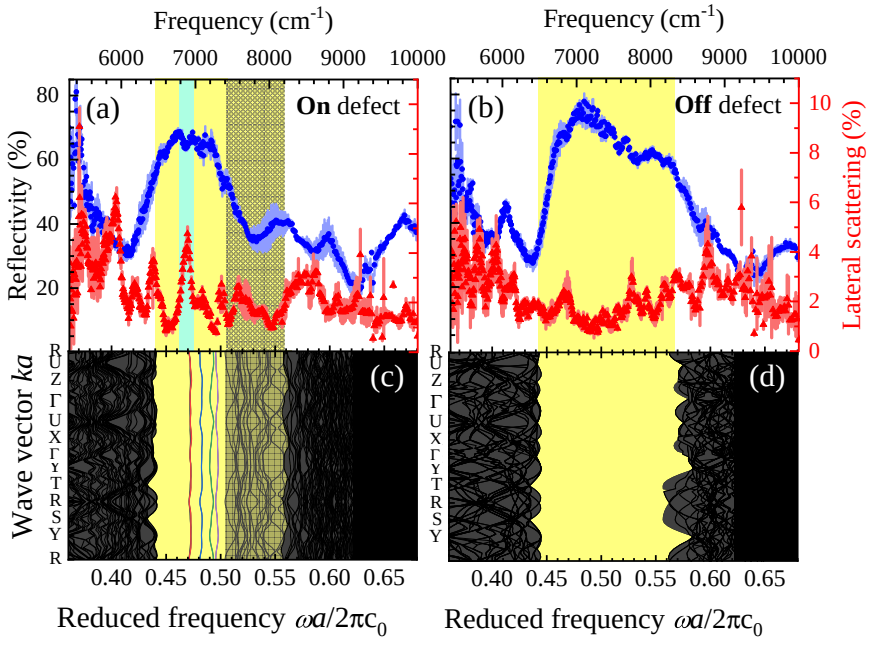

Figure 7.3: (a,b) Measured reflectivity (black dots) and lateral scattering (red triangles, right ordinate) spectra of the 3^3 cavity superlattice (SL5) on a defect and in between two defects (at $X = 2.5$ μm). These data were measured with *s*-polarized light, *i.e.*, E-field perpendicular to the X-directed pores. The broad reflectivity peaks correspond to the band gaps of the crystal at the relevant location, as indicated by the yellow regions that match very well with the theory. In (a), the lateral scattering peak at 6900 cm^{-1} within the band gap (cyan highlight) corresponds to a reflectivity trough and to a Cartesian band in the band structures. (c) Photonic band structure of a cavity superlattice in an infinite inverse woodpile photonic crystal, rotated for comparison with measured spectra below. The frequency and wave vector are reduced by the lattice parameter a. The dielectric constant is $\epsilon = 12.1$ typical of Si. The crystal pores have a relative radius $r/a = 0.22$ and the defect pores $r' = r/2$. The yellow region between $a/\lambda = 0.44$ and 0.502 is the 3D photonic band gap of the superlattice crystal, and the allowed bands outside the band gap are shown as dark grey shaded areas. The cavity superlattice sustains two types of bands inside the original band gap (see b): flat bands typical of Cartesian coupled-cavity resonances in the lower half of the band gap (colored bands), and other bands in the upper half of the band gap (black bands). (d) Photonic band structure of an inverse woodpile photonic crystal with $r/a = 0.22$ without cavities. The yellow region between $a/\lambda = 0.44$ and 0.56 is the photonic band gap. Band structures calculated by M. Kozon.

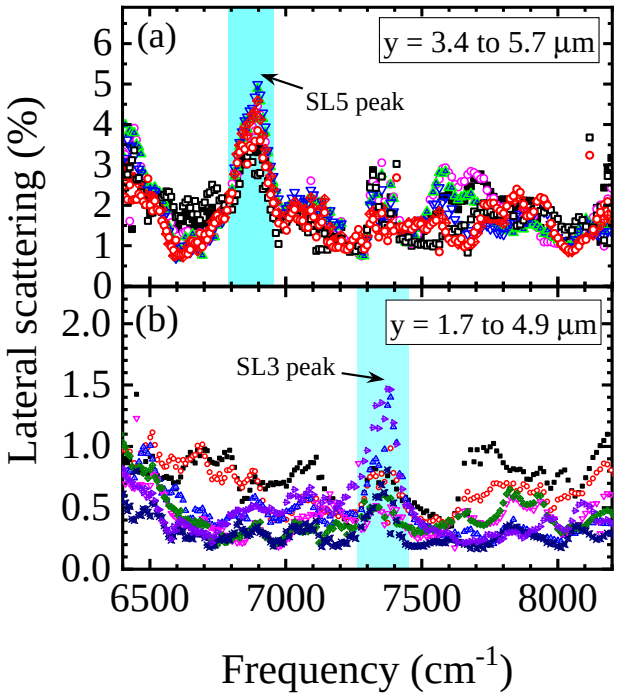

Figure 7.4: (a) Multiple lateral scattering spectra in the vicinity of a defect show the reproducible peak near 6900 cm^{-1} for superlattice SL5. (b) Multiple spectra across three defect pores, show a reproducible peak near 7386 cm^{-1} for superlattice SL3. The Y-positions of the spectra are given in the legends while the X-position is nearly constant (about 2.5μm). The frequency range shown covers roughly the original band gap of the crystal.

focusing away from the defects (see Figure 7.3(b)). The modulation of the upper edge of the measured gap versus position is clearly revealed in Figure 7.5, where the gap narrows at every defect pore. The center frequency and the width of the measured reflectivity stopband of the superlattice (Figs. 7.3(a,b)) agree very well with the theoretical band gap (Figs. 7.3(c,d), respectively), meaning that the fabricated nanostructure and its optical functionality match closely with the intended structure and the intended optical behavior. We also observe that when focusing on the defect, the maximum reflectivity (R_{max} = 68%, Figure 7.3(a)) is less than when focusing away from the defects (R_{max} = 74%, Figure 7.3(b)), which is intuitively reasonable since light incident on defects will also be scattered non-resonantly, thereby reducing the specular reflectivity. This observation reproduces at other cavity locations and also when scanning the incident light along the Y-direction (see Appendix of this chapter).

When focusing incident light on a defect (Figure 7.3(a)), the lateral scattering spectrum shows a distinct peak at 6900 cm^{-1} inside the band gap. The peak

corresponds to light that is scattered from the incident wave vectors to outgoing wave vectors that differ from the incident ones and their specular reflected counterparts. Therefore, one expects less light to be reflected, and indeed, the reflectivity spectrum reveals a corresponding trough in the same frequency band. Moreover, the scattering peak and the reflectivity trough match well with a Cartesian superlattice band in the band structures (Figure 7.3(b)). The observation of resonant features, both in (specular) reflectivity and in scattering confirm that the confinement of light in the superlattice is truly a 3D phenomenon as opposed to 1D confinement in a Fabry-Pérot cavity that is apparent in reflectivity or transmission only, but not in lateral scattering. We emphasize that the peak only correlates with incident light being focused onto a defect; when the incident light is focused in between defects the peak is absent, see Figure 7.3(b)). The sum of the reflectivity and the lateral scattering do not add to a total of 100% since our setup can only access part of the light scattered in the −X-direction into the air, whereas light scattered in the $(+X, \pm Y)$-directions escapes undetected. Since these scattered contributions propagate in the high-index Si substrate, it is conceivable that their contributions are considerably larger than the detected fraction in air, which may in turn be further attenuated by Fresnel reflectivity at the crystal-air interface.

To distinguish a potential superlattice peak from random speckle peaks that arise as a result of random and unavoidable structural variations [35, 253] we monitor the reproducibility of the peaks while scanning the illuminating spot across the sample surface. Therefore, we plot multiple lateral scattering spectra at different Y-positions near the defect pore (at $X = 2.5$ μm), as shown in Figure 7.4(a) and (b) for the superlattices SL5 and SL3, respectively. From this plot, we observe that the peak near 6900 cm^{-1} is reproduced at all positions near the defect pore, with gradually decreasing intensity as the focus moves away from the defect pore (more details in Figure 7.8 of Appendix 7.A). We also observe a second reproducing peak near 7386 cm^{-1}, which may be a second superlattice band. For the superlattice SL3 (Figure 7.4(b)), we also see a scattering peak near 7386 cm^{-1} that reproduces even across multiple defect pores. All other scattering peaks do not reproduce, hence they are uncorrelated speckles arising from unavoidable disorder of the crystal. Therefore, we conclude that all reproducing peaks are spectral features of the intentional superlattice of defects. We now turn our attention to address if these spectral features arise from coupled or individual cavities.

Distinguish superlattice coupled modes

Due to an inadvertent nanofabrication inhomogeneity of the underlying band gap crystals, we find from the position-dependent measurement that the band gaps shift across the crystals. Indeed, Figure 7.5(a,b) show that the band edges shift to lower frequencies while the superlattices are scanned from $Y = 0$ to 10 μm. In superlattice SL5 (Figure 7.5(a)), we observe near the 2nd defect pore a scattering peak centered at 6896 cm^{-1}. Scanning further to the 3rd defect pore, the scattering peak is replaced by another one at a lower frequency 6358 cm^{-1}.

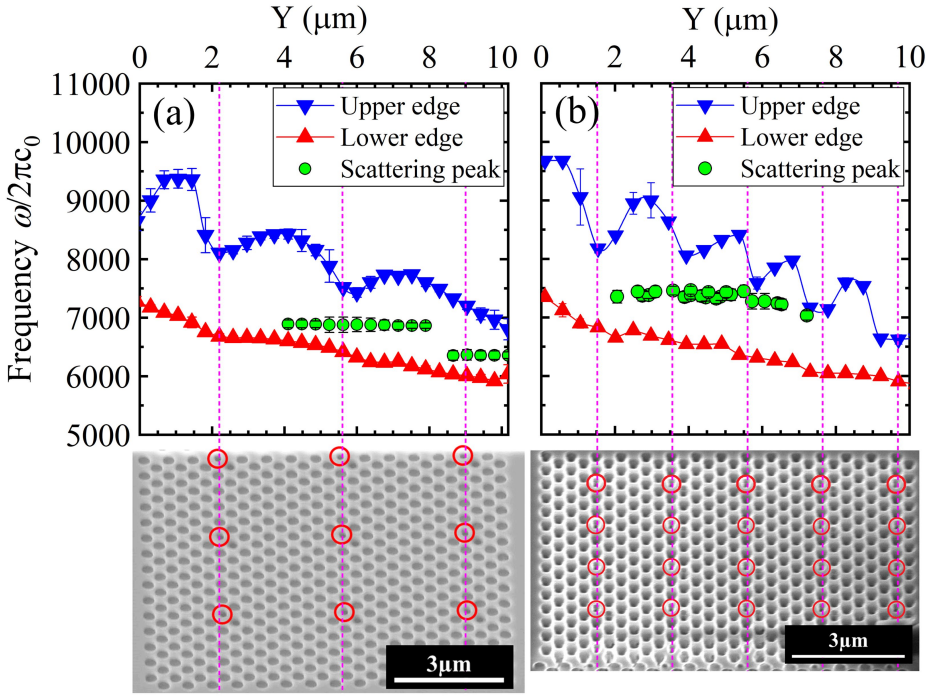

Figure 7.5: Lower edges (red upright triangles) and upper edges (blue downward triangles) of the position-dependent photonic gap versus Y, obtained from reflectivity measurements on two crystals with a cavity superlattice with different lattice spacings. Frequency of the peak inside the stopband obtained from lateral scattering measurements are shown by green circles on each panel. Below each plot the SEM image of the surface of the crystals is stitched with the same scale for reference for the reader. The magenta dashed lines trace the positions of the defect pores.

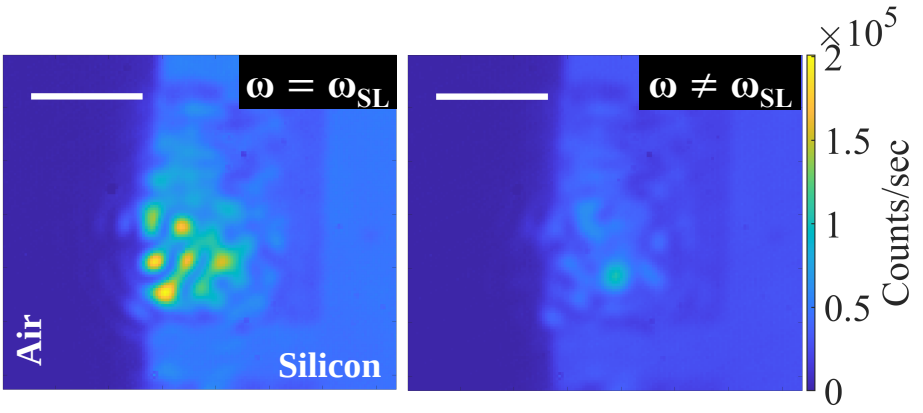

Figure 7.6: Camera images of the front surface of superlattice SL3 for cross-polarized light, taken at two different frequencies. Left: at $\omega = 7386$ cm^{-1} $= \omega_{\mathrm{SL}}$, *i.e.* at the center of the superlattice peak. Right: at 7174 cm^{-1}, outside the superlattice peak. The surface of the crystal is illuminated by a separate LED to reveal the rectangular xy crystal surface. On the top left of each figure, the white bar on the top left indicates a scale of 5 μm.

Since the peaks correspond to the intentional defects, they represent cavity peaks. Since the peaks differ for the different defects, they are uncoupled in the Y-direction.[3] Strikingly, in superlattice SL3 the scattering peak has the same center frequency (7386 cm^{-1}) when scanned across multiple cavities (Figure 7.5(b)). This implies that multiple cavities are coupled in the Y-direction, hence the peak represents a *bona fide* superlattice band typical of Cartesian light that hops through the superlattice [97]. To the best of our knowledge, this is the first experimental observation of a 3D superlattice band in a 3D band gap.

To visualize the hopping of light in the superlattice, we capture images of the front surface of SL3 while illuminating with different frequencies. We detect in the crossed polarization state to avoid light that is single scattered from the sample surface and select the light that has multiply scattered inside the crystal. So we expect to detect light scattered from embedded cavities as well as structural unavoidable disorder. We present images for two frequencies, at the center of the superlattice peak $\omega = \omega_{\mathrm{SL}}$ (= 7386 cm^{-1}), and outside the peak $\omega \neq \omega_{\mathrm{SL}}$ (= 7174 cm^{-1}), yet inside the original band gap. In both cases, we see a speckle pattern due to multiple scattering by the crystal. At $\omega = \omega_{SL}$, the light spreads over a large area, much larger than the incident spot. Intensity maxima near the defect pores are observed, as shown in the left image in Figure 7.6. Along the X-direction, the three intensity maxima are spaced equally apart. From the camera image, we find the average distance between the centers of two consecutive intensity maxima along X to be 1.50±0.06 μm. From the design of the crystal, the

[3] It is conceivable that the cavities are coupled in the (X,Z)-directions, but this awaits evidence later.

distance between two defect pores along X-direction is $c_{\mathrm{SL}} = 3c = 3 \times 0.48\ \mu\mathrm{m} = 1.44\ \mu\mathrm{m}$. This good agreement proves that in SL3, the superlattice frequency hops not only in Y, but also in X-direction, over at least 3 neighboring cavities. This observation firmly establishes that we observe light hopping in a 3D superlattice. In the latter case at $\omega \neq \omega_{\mathrm{SL}}$, the overall intensity of the scattered reflection is comparatively lower as shown in the right image of Figure 7.6 and we do not observe features similar to the previous case.

7.3.2 Probe with p-polarized light

On superlattice SL5, we also measure spectra with p-polarized incident light. In this case, a few noticeable differences compared to the s-polarized case were observed. In figure 7.7(a) and (b), we show the reflectivity and lateral scattering spectra measured and 2 locations, near and in between defects. The reflectivity peaks are wide even when measured near the defect pores, with broad and narrow troughs in them. In both cases, the lateral scattering spectra show a clear anticorrelation with reflectivity throughout almost the entire frequency range. We also detect an overall increase in the scattered intensity compared to the s-polarized case. The most interesting features in the scattered spectra are the intense peaks within the original band gap. The LS peak in figure 7.7(a) corresponds to the deep, narrow trough of the reflectivity inside the gap. The small error bars indicate that the peak is reproducible in the vicinity of the probed location. When we compare these spectra with the band structure, the LS peak in figure 7.7(a) corresponds to one or more flat superlattice bands. The other smaller peak near frequency 7700 cm^{-1} has large error bars, implying a non-reproducible signal implying a non-reproducible signal. In figure 7.7(b), there is a very intense LS peak within the gap, at a higher frequency. This peak, however, is sensitive to probing location, as the error bars are large and corresponds to the broad trough in reflectivity. This peak could be a superlattice mode, and it could also appear due to the 2D localized states along the line defects in the crystal that are included in the dispersive bands in the high-frequency side of the band gap. More theoretical understanding is required to explain these observations, as many experimental factors such as different types of disorder in the crystal cannot be taken into account in the band structure calculations[4]. The frequencies corresponding to both of the lateral scattering peaks in Figures 7.9(a) and 7.9(b) are different from those obtained from the s-polarized measurements, implying the polarization dependence of the various optical modes within the band gap, as seen in calculations by Devashish *et al.* [187].

[4]Calculating band structures and transport [187] that would include disorder will be a major enterprise to study realistic structures.

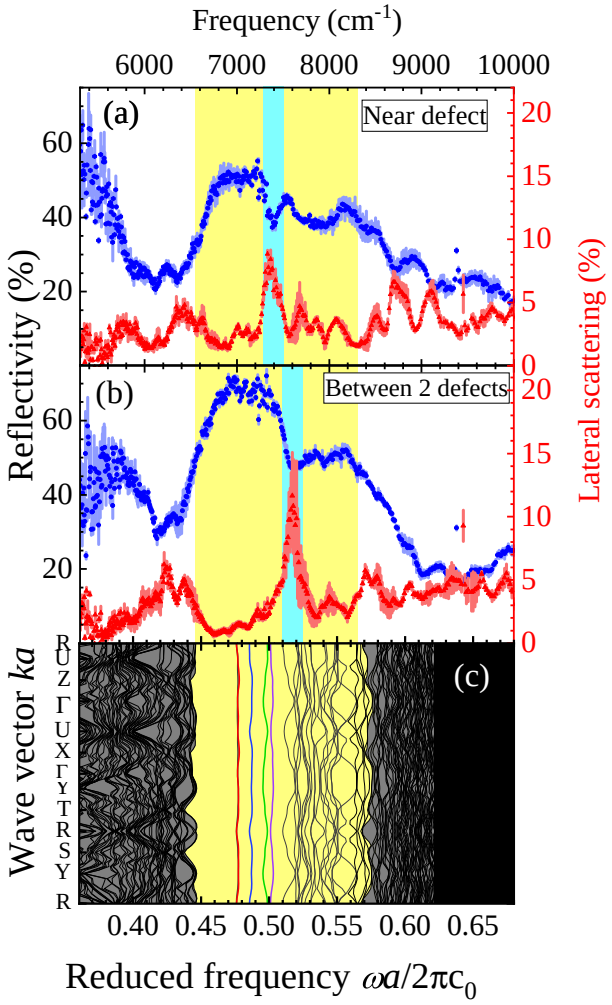

Figure 7.7: (a,b) Measured reflectivity (blue dots) and lateral scattering (red triangles, right ordinate) spectra of the 3^3 cavity superlattice (SL5) near a defect and in between two defects (at $X = 2.5$ μm). These data were measured with p-polarized light, *i.e.*, E-field parallel to the X-directed pores. The broad reflectivity peaks correspond to the band gaps of the crystal at the relevant location, as indicated by the yellow regions that match very well with the theory. In (a), the lateral scattering peak at 7400 cm^{-1} within the band gap (cyan highlight) corresponds to a reflectivity trough. (c) Photonic band structure of a cavity superlattice in an infinite inverse woodpile photonic crystal.

7.4 Discussion

7.4.1 Explanations on experimental features

We have observed many features from the reflectivity and scattering data measured on 3D photonic band gap crystals with a 3D superlattice of cavities. Such a band gap superlattice is new, and hence it is a challenge to interpret the experimental observations. In crystal fabrication, primarily we are limited by deviations of crystal parameters from the design. Hence, a straightforward comparison of the broadband spectra with band structures that are calculated for perfect, infinite crystals is insufficient. Our observation that the reflectivity peaks of the crystal with superlattice of cavities matches with the expected band gap is encouraging for further analysis. The challenging aspect is the interpretation of the various spectral features (troughs and peaks) observed in the reflectivity and lateral scattering measurements given their sensitivity to fabrication errors. For example, we always assume that the defect pores are half the diameter of the normal pores forming the photonic crystal. However, in reality, as all the pores are not perfect cylinders, it is unknown whether this relation holds for every part in the crystal. Moreover, the fabricated crystals have a finite size, which makes a direct comparison to infinite crystal lattice computations challenging. Hence, the comparison with band structures is not the final way of interpreting data. We intend to model structures with realistic features such as disorder and pore tapering and scallops within pores to interpret and predict experimental results more accurately.

Another important observation we make from our data is the frequency bandwidth of the intensity peak of the laterally scattered light or of the trough in reflectivity within the band gap. This bandwidth is related to the width of the superlattice mode. We observe that the measured frequency width is much wider ($\Delta\omega/\omega_{\mathrm{SL}} \approx 2\%$) than the maximum dispersion bandwidth of the isolated superlattice modes (maximum $\Delta\omega/\omega_{\mathrm{SL}} \approx 0.2\%$) in the band structure. We make the following possible explanations for this observation:

1. The frequency tuning resolution of our setup including the linewidth of the source is more than 0.2% (about 0.3%), hence is not sufficient to resolve the superlattice features. Therefore, it is relevant to repeat the experiments with a finely tunable laser source.

2. The signal that we measure is the result of coupling between different cavities in the crystal that have individual resonance linewidths. Since all cavities are not exactly the same due to fabrication deviations, the center frequency and linewidths of the individual cavities differ slightly, resulting in broader width of the coupled mode.

3. It is likely that disorder-induced scattering might be present at a frequency corresponding to superlattice mode, such scattering would result in speckles with a certain frequency correlation (similar as studies in chapter 4) that overlaps with the superlattice mode.

It has been shown that changing the distance between cavities leads to larger dispersion and thus more coupling [97]. This is probably the reason why we see little interaction of light with the cavities when we focus light in between two defects along Y-direction in the crystal SL5 (figure 7.3(b)). Hence, it is possible to tune the coupling between the cavities by decreasing the distance between neighboring strongly coupled cavities. Indeed, in SL3, we see that the same mode is excited at locations covering multiple cavities along Y. We also observe coupling along X-direction in this case from the scattered reflection image in figure 7.6.

7.4.2 Analogies with electronic band gap materials

An analogous system of defect bands in photonic band gap crystals are intermediate bands in defect-induced semiconductors that were recently reported even in naturally occurring materials [254–258]. Intermediate bands are partially occupied bands within the electronic band gap that are isolated from the valence and conduction bands. They are an extra step for the valence band electrons to jump to the conduction band. Such materials are used for increasing efficiency in solar cells, as additional lower-energy photons get absorbed due to the intermediate bands. While in the electronic case the defects are introduced in the form of different elements, either by diffusion or chemical processes, in photonic lattices, defects are usually formed by locally changing the refractive index. The fundamental difference between these two cases is the transport mechanism. Intermediate semiconductor bands increase energy absorption efficiency so that there is a higher transition of electron-holes across the band gap, thereby resulting in a higher conduction. When a higher voltage is applied across the semiconductor junction (or more photons in the case of solar cells), the conduction is increased. However, in photonic band gap with defect states, there is no such transition due to a lack of analogy with the bias voltage. Hence the type of light transport in the band gap occurs when there are line defects in the structure as in [74, 92] or multiple point defects or 3D cavities that are coupled to each other.

7.5 Conclusion and outlook

We have experimentally detected the signature of light propagation from a 3D array of cavities buried in a 3D photonic band gap. We measured spectra of laterally scattered light from 3D superlattices of cavities that show narrow peaks within the band gap, which correspond to superlattice modes. To the best of our knowledge, this is the first experimental detection of 3D coupled-cavity propagation in photonic band gap crystals. With polarization-resolved measurements, we also detect signature of possible 2D confinement in the crystals arising as a result of the line defects. Such a system is analogous to electronic band gap materials with intermediate bands within the band gap that facilitates charge transport. Since our superlattices are made of silicon by CMOS-compatible methods, they have the potential of integration into optoelectronic devices, where controlled light propagation in 3D is required. Also, such a band gap superlattice will be

very interesting to study the emission of light from active sources like quantum dots with emission within the band gap when placed inside the cavities. It provides great potential to realize strongly-coupled cavities, which is a platform for repulsive boson systems that have exciting physical properties including photonic phase transitions [259].

The phenomenon of Anderson localization of waves in 3D, where diffusion is absent in all directions, has not yet been observed experimentally for light. In Anderson localized state, wave functions are localized in a small region of space, with very short-range fields [9]. With 3D superlattice in photonic band gap, it might be possible to realize this effect experimentally by selectively placing 3D cavities within the band gap [10].

Appendix 7

7.A Position dependence of the spectral features

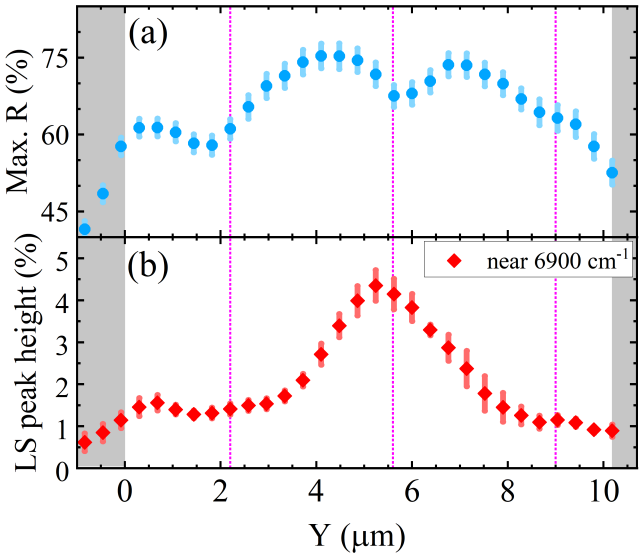

Figure 7.8: (a) Maximum value of the reflectivity peak, and (b) height of the scattering peak near frequency 6900 cm^{-1} as a function of Y at $X = 2.5\mu m$. The vertical magenta lines are the locations of the defect pores. The data are extracted from measurements using s-polarized incident light.

We extract all the important reflectivity and lateral scattering features as a function of Y from the systematic position-resolved measurements performed on SL5. In figure 7.8(a) and 7.9(a), the maximum reflectivity in the gap are plotted for s- and p-polarized incident light respectively, that clearly shows that it decreases exactly on the locations of the defect pores. Figure 7.8(b) shows the amplitude of the lateral scattering peak at 6900 cm^{-1} (the peak shown in figure 7.4(a)). The peak has maximum signal when the focus is aligned to a defect (vertical magenta line at $Y = 5.4$ μm) and decreases when the focus is scanned away. Here we observe that the mentioned LS peak is a local effect of the cavities near the defect pore at $Y = 5.4$ μm. On the sites of the other defect pores, this particular peak is not observed, possibly due to the inhomogeneity of the crystal along Y, and sensitivity of the cavity modes with polarization.

Interestingly, the LS peak obtained from p-polarized measurements are of different character. We find two dominating LS peaks at two different locations on the crystal. The first one at frequency 7360 cm^{-1} is the most intense near the defect pore at $Y = 2.1$ μm. Similar to the LS peak for s-polarized case, the intensity of this peak also decreases as Y drifts from the defect pore. We observe

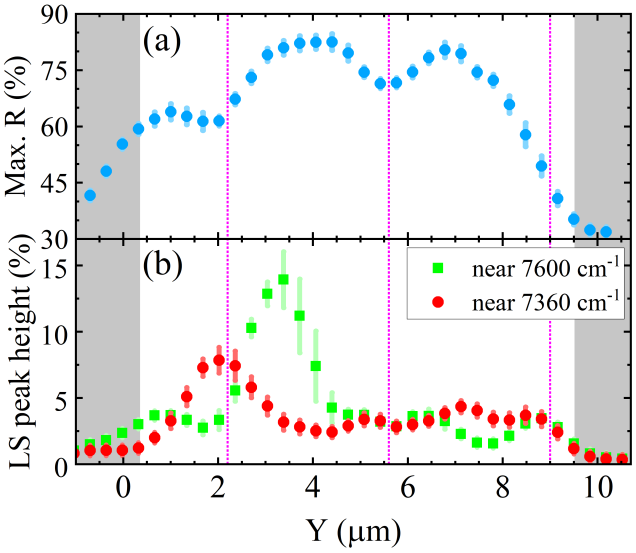

Figure 7.9: (a) Maximum value of the reflectivity peak, and (b) height of the scattering peak near frequency 7360 cm^{-1} and 7600 cm^{-1} as a function of Y at $X = 2.5\mu$m. The vertical magenta lines are the locations of the defect pores. The data are extracted from measurements using p-polarized incident light.

another interesting intense peak a bit further away (near $Y = 2.8$ μm) from the defect pore. The frequency of this peak is higher than the first one (7600 cm^{-1}) and lies very close to the dispersive bands in the higher frequency range withing the photonic gap. From the observations, we conclude that both these peaks are the result of intentional defects in the crystal. To understand their exact behavior we have to carry out detailed numerical models that account for the fabrication deviations.

Chapter 8

Summary and outlook

8.1 Summary

This thesis explores the possibilities of controlled light propagation in different nanophotonic media, namely: randomly scattering, periodic and super-periodic media. Various instances of these types of materials have been experimentally investigated for the different possible ways of (controlled) interaction of near-infrared (NIR) light with such materials. The ultimate goal is to build up completely new knowledge and expertise about the special mode of propagation of light in superperiodic systems. These special structures consist of a three-dimensional (3D) grid of coupled optical cavities. Such a configuration provides access to a form of light transport that has been known only in electronic systems. These special conditions can give access to never-before-seen phase transitions like Anderson localization. The structures are also CMOS compatible and functional in the telecom bands that are used for wireless communication. This gives the possibility to combine these structures in the future with other existing electro-optical components. Below is a summary of each chapter:

Ch. 2 This chapter provides a detailed overview of the experimental setup that is used in all subsequent chapters. With this setup, it is possible to measure broadband reflection, transmission as well as the lateral scattering of various optical media. Furthermore, a spatial light modulator (SLM) allows us to perform wavefront shaping to steer light. The specialty of the setup is to measure samples optically over a wide spectral range from 950 to 2000 nm, with a narrow spectral linewidth of 0.7 nm. All relevant technical details are covered and the limitations of the setup are explored. In addition, an overview is given of the CMOS-compatible optical samples measured in chapters 5, 6, and 7, namely 2D photonic crystals, 3D photonic crystals, and 3D super-periodic crystals.

Ch. 3 Optical speckles are produced when different light paths in a multiply scat-

tering medium interfere coherently. In experiments, speckles are affected by the interaction between light and the scattering material on the one hand, and also the properties of the light source and the detector. Typically, speckle is measured with a narrow-band light source because such source has a long coherence length. However, the setup described in chapter 2 has a comparatively broad linewidth than typical narrowband laser sources. The large linewidth reduces the temporal coherence of the light and thus influences the speckle statistics. In this chapter, we examine how this linewidth influences the speckle statistics using measurements on a sample consisting of ZnO nanoparticles. We show that the speckle statistic deviates from the expected exponential distribution. This deviation is due to both the light source and the high noise of the detector used. This conclusion has been validated with measurements with approximately monochromatic light sources and a detector with less noise. This quantifies the limitations of the setup and that the setup properties are sufficient for meaningful measurements described in the subsequent chapters.

Ch. 4 By changing the spatial phase of the wavefront of the incident light, is it possible to realize a focus behind a scattering medium. This process is known as wavefront shaping (WFS). Typically, the optimized wavefront is unique to the frequency of the incoming light, but there exists some correlation with optimized wavefronts for the neighboring frequencies. This is given by the speckle correlation function. In this chapter, we investigate for the entire range of telecom wavelengths the spectral width of this correlation. It follows that for weak scattering media it is possible to reach the spectral bandwidth of WFS to tens of THz (about 100 nm) in the NIR. These results indicate the opportunity to implement WFS with scattering media for focusing light over a very wide frequency range.

Ch. 5 3D photonic crystals with the inverse woodpile structure, fabricated by CMOS-compatible methods were studied and found to exhibit a complete photonic band gap, whose frequency range depends on the radius of nanopores and the lattice parameter. The crystals exhibit wide photonic band gaps in various ranges of the telecom bands. Up to 96% reflectivity within the band gap was measured, which is to our knowledge record the highest band gap reflectivity of 3D photonic crystals. Such high-quality band gap crystals are ideal for shielding active sources when placed inside and to confine defect modes within the band gap.

Ch. 6 We performed spectral measurement of reflectivity and lateral scattering from 2D photonic crystals that reveal the directional photonic gaps of such structures. Within the gap, where otherwise no Bloch modes are allowed, the disorder-induced scattered light within the gap was steered deep into the crystal far beyond the depth called Bragg length that is allowed conventionally by crystal diffraction. Wavefront shaping (WFS) of telecom light in the L-band (see Table 1.1) on 2D photonic crystals to send light as deep as 8× the Bragg length of the crystal.

Table 8.1: Interaction of light in various nanophotonic media + outlook

Arrangement	**Structure**	**DOS**	**Wave propagation**	**Length scale**	**WFS**
Random	ZnO	Continuous (no gap)	Multiple scattering, random walk	ℓ	Yes
2D periodic	2D photonic crystal	2D gap	Bloch (outside gap), no Bloch (in gap) + random walk	L_B + L_{ext}	Yes
3D periodic	3D photonic crystal	3D gap	Bloch (outside gap), no Bloch (in gap) + random walk	To find	Prelim.
3D superperiodic	3D photonic crystal with superlattice of defects	3D gap + defect bands	Bloch (outside gap), no Bloch + random walk + light hopping (in gap)	To find	Prelim.

Ch. 7 A structure of periodically placed coupled cavities embedded in a 3D photonic crystal forms a superperiodic photonic medium. Such a medium gives the possibility to make light 'hop' between the various neighboring cavities. This hopping takes place within the band gap of the underlying 3D crystal, where normally no light propagation is possible. Both broadband reflection and scattering measurements on such superperiodic media reveal the existence of these cavity modes inside the band gap of the 3D photonic crystals. This is the very first observation of a completely new form of light transport in a 3D super-periodic photonic crystal.

The experimental results of controlled light propagation within the photonic band gap described in this thesis have scopes to further extend and improve. Due to technical issues with crystal fabrication and a few limitations in the setup, we were unfortunately not able to investigate some more features. Therefore, in the next section, a few points are outlined that can be addressed for further research.

8.2 Outlook

In this thesis, we show the experimental results, along with modeling of field enhancement inside 2D photonic crystals by WFS. 2D crystals have directional photonic gaps, which means light escapes in other directions that allow propagating modes. This is not the case for 3D crystals since they possess a complete band gap irrespective of direction and polarization. Hence once the light is inside, in an ideal situation it would decay exponentially inside the crystal before escaping; or in presence of superlattice of cavities, the light would hop from cavity to cavity

and escape the structure. In 3D, we can in principle apply the same WFS procedure described in chapter 6 for 2D crystals by detecting the laterally scattered light. The method will be suitable for 3D superlattices since the aim of the superlattice is to transport the coupled-cavity modes through the crystal. Therefore, in experiments involving WFS in superlattices, we want the target location for intensity optimization to be outside the crystal. Optimizing the lateral scattering intensity of light with superlattice frequencies obtained by methods described in chapter 7 would increase light transport and coupling to certain directions of the superlattice. The preliminary work for WFS in 3D crystals has been done and exciting results are reported in the MSc thesis of T. Vreman [260].

In chapter 1, we provided in Table 1.2 the various nanophotonic media that are studied here and the density of states (DOS) and mode of light propagation in them. We investigated these parameters in various chapters in this thesis. The dominant length scale in periodic media, *i.e.* the Bragg length was explored for 2D crystals in chapter 6. Often real crystals have a more realistic decay length called extinction length due to disorder and finite-size effects. Similar Bragg length is also possible to estimate for the 3D crystals from the measured stopband [187], given as

$$L_B = \frac{2d}{\pi} \frac{\omega_c}{\Delta\omega}, \tag{8.1}$$

where d is the lattice spacing. However, due to the limited thickness of our 3D crystals (at most 5 μm due to limited pore depth from etching, see Figure 5.9), the extinction of light into the crystal is not easy to measure from lateral scattered light. For 3D superlattices, there are two types of length scales within the band gap: the Bragg length L_B at frequencies $\omega \neq \omega_{\mathrm{SL}}$ and L_{couple} at $\omega = \omega_{\mathrm{SL}}$, where superlattice coupled modes propagate deep inside the crystal. The latter type of length scale has not yet been explored.

The following ideas of measurement and analysis can be readily implemented:

- When a superlattice mode is identified from reflectivity and lateral scattering measurements, make reflected speckle images with cross-polarized detection at that frequency (ω_{SL}) as in Figure 7.6. Then move the focus around the same location to record multiple images, while keeping the frequency the same. The average of the speckle patterns should average out the intensity fluctuations of speckle arising from random disorder, making it easier to isolate signals from the cavities.

- The lateral scattering spectra usually contain many speckles that arise from random disorders. Some statistical analysis techniques can be implemented on such spectra. For example, intensity statistics of the spectra can be studied, similar to methods shown in chapter 3. Theoretically, the intensity statistics of speckle from random disorder should be closer to the standard exponential behavior while that of superlattice signature would deviate from it. Another possibility is to compute the autocorrelation, *i.e.,* the correlation between the signal and the frequency-shifted signal of the spectral intensity. As seen in Figure 8.1, the autocorrelation is less below

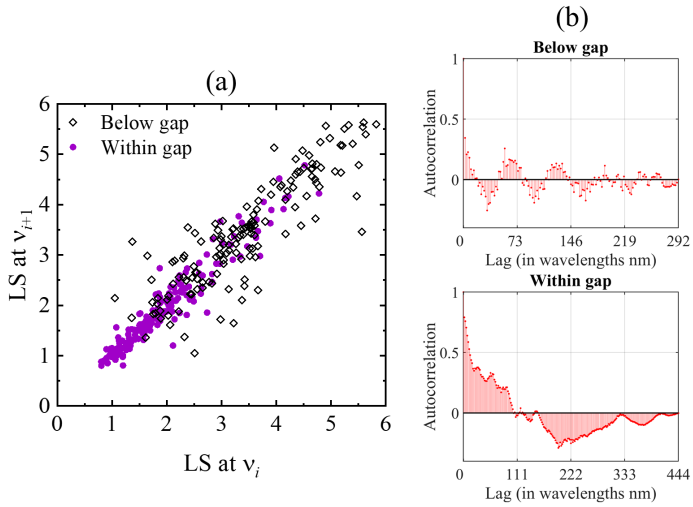

Figure 8.1: (a) A parametric plot of the laterally scattered intensity of crystal SL5 within and below the band gap with a lag in frequency corresponding to a wavelength of 2 nm. Below the gap, the intensity is more scattered and in gap there is more correlation. (b) A quantitative plot of the autocorrelation function below (top) and within (bottom) the gap. The x-axis is in wavelengths instead of frequency because the measurements were done with linear scale in wavelength.

compared to within the photonic gap[1].

Below we state a few ideas that could be implemented in the measuring setup for improved detection of the features:

* Higher magnification and NA: The setup provides imaging magnification of 250× and NA = 0.85 on reflection and 125× and NA = 0.42 on the lateral side. Higher magnification and NA on the lateral side as well would help in selecting a target spot for WFS with better resolution and accuracy.

* Currently in the setup, the lateral scattering signal is partially clipped by the focusing objective MO1, which eclipses part of the scattered signal from the samples. Thus the effective NA of MO2 is lower, resulting in lower imaging resolution. Replacing MO1 with a longer working distance objective should solve this problem.

* Introduce a narrowband ($\Delta\lambda \ll 0.1$ nm) tunable laser with high temporal coherence to the setup. We have seen from analyses in chapter 3 that limited temporal coherence (broad linewidth) of our current source has an effect on the measurements.

[1]We thank Arie den Boef, Patrick Tinnemans, Vahid Bastani, Wim Coene, and Scott Middlebrooks from ASML for inspiring discussions that triggered this study.

- Replace components of the setup (*e.g.* SLM, objective MO2, lenses) that are not well-compatible with the whole range of NIR wavelengths that is scanned for the measurements.

Bibliography

[1] *The International Year of Light and Light-based Technologies 2015*. `https://www.light2015.org/Home/About/IYL-Final-Report.html`. 11

[2] M. Born, E. Wolf, and A. Bhatia, *Principles of Optics: Electromagnetic Theory of Propagation, Interference, and Diffraction of Light*, Macmillan (1959). 12

[3] E. Hecht and A. Zajac, *Optics*, Addison-Wesley Publishing Company (1987). 12, 13, 18

[4] S. Chu and S. Wong, *Linear Pulse Propagation in an Absorbing Medium*, Phys. Rev. Lett. **48**:738–741 (1982). 12

[5] R. Bartholin, *Experimenta Crystalli Islandici disdiaclastici, quibus mira et insolita refractio detegitur* (1669). 12

[6] D. Bicout, C. Brosseau, A. S. Martinez, and J. M. Schmitt, *Depolarization of multiply scattered waves by spherical diffusers: Influence of the size parameter*, Phys. Rev. E **49**:1767–1770 (1994). 12, 15, 67

[7] R. Ramaswami, *Optical fiber communication: from transmission to networking*, IEEE Communications Magazine **40**(5):138–147 (2002). 13

[8] H. E. Burton, *The Optics of Euclid1*, J. Opt. Soc. Am. **35**(5):357–372 (1945). 12

[9] P. W. Anderson, *Absence of Diffusion in Certain Random Lattices*, Phys. Rev. **109**:1492–1505 (1958). 13, 97, 117

[10] S. John, *Strong localization of photons in certain disordered dielectric superlattices*, Phys. Rev. Lett. **58**(23):2486–2489 (1987). 13, 14, 117

[11] M. Segev, Y. Silberberg, and D. Christodoulides, *Anderson localization of light*, Nat. Photonics **7**:197–204 (2013). 13

[12] P. W. Anderson, *More Is Different*, Science **177**(4047):393–396 (1972). 13

[13] R. Dalichaouch, J. P. Armstrong, S. Schultz, P. M. Platzman, and S. L. McCall, *Microwave localization by two-dimensional random scattering*, Nature **354**:53–55 (1991). 13

[14] D. S. Montgomery, R. J. Focia, H. A. Rose, D. A. Russell, J. A. Cobble, J. C. Fernández, and R. P. Johnson, *Observation of Stimulated Electron-Acoustic-Wave Scattering*, Phys. Rev. Lett. **87**:155001 (2001). 13

[15] M. F. Collins, V. J. Minkiewicz, R. Nathans, L. Passell, and G. Shirane, *Critical and Spin-Wave Scattering of Neutrons from Iron*, Phys. Rev. **179**:417–430 (1969). 13

[16] A. Wischnewski, U. Buchenau, A. J. Dianoux, W. A. Kamitakahara, and

J. L. Zarestky, *Sound-wave scattering in silica*, Phys. Rev. B **57**:2663–2666 (1998). 13

[17] J. E. G. J. Wijnhoven and W. L. Vos, *Preparation of Photonic Crystals Made of Air Spheres in Titania*, Science **281**(5378):802–804 (1998). 13, 82

[18] W. L. Vos, R. Sprik, A. van Blaaderen, A. Imhof, A. Lagendijk, and G. H. Wegdam, *Strong effects of photonic band structures on the diffraction of colloidal crystals*, Phys. Rev. B **53**:16231–16235 (1996). 13, 74, 93

[19] L. Novotny and B. Hecht, *Principles of Nano-Optics*, Cambridge University (2006). 13, 70

[20] J. D. Joannopoulos, S. Johnson, J. N. Winn, and R. D. Meade, *Photonic crystals: molding the flow of light*, Princeton University (2008). 13, 19, 70, 81, 103

[21] M. A. Noginov, G. Dewar, M. W. McCall, and N. I. Zheludev (editors), *Tutorials in Complex Photonic Media*, SPIE, Bellingham, Washington (2009). 13

[22] C. Soukoulis (editor), *Photonic Crystals and Light Localization in the 21st Century*, Springer Netherlands (2001). 13, 103

[23] R. B. Wehrspohn, H.-S. Kitzerow, and K. Busch (editors), *Nanophotonic Materials: Photonic Crystals, Plasmonics, and Metamaterials*, John Wiley & Sons, Ltd (2008). 13

[24] D. Pagnoux, J. Lourtioz, P. de Fornel, H. Benisty, V. Berger, J. Gerard, D. Maystre, and A. Tchelnokov, *Photonic Crystals: Towards Nanoscale Photonic Devices*, Springer Berlin Heidelberg (2008). 13

[25] M. Ghulinyan and L. Pavesi, *Light Localisation and Lasing: Random and Pseudo-random Photonic Structures*, Cambridge University Press (2015). 13, 70, 103

[26] C. Kittel, *Introduction to Solid State Physics*, John Wiley & Sons Inc., New York, NY, 8th edn. (2004). 14

[27] L. Rayleigh, *XXVI. On the remarkable phenomenon of crystalline reflexion described by Prof. Stokes*, The London, Edinburgh, and Dublin Philosophical Magazine and Journal of Science **26**(160):256–265 (1888). 14, 18

[28] E. Yablonovitch, *Inhibited spontaneous emission in solid-state physics and electronics*, Phys. Rev. Lett. **58**(20):2059–2062 (1987). 14, 20

[29] E. Yablonovitch, *Photonic band-gap crystals*, J. Phys.: Condens. Matter **5**(16):2443 (1993). 14

[30] J. Joannopoulos, R. Pierre, and S. F. Villeneuve, *Photonic crystals:putting a new twist on light*, Nature **386**:143–149 (1997). 14

[31] A. Lagendijk and B. A. van Tiggelen, *Resonant multple scattering of light*, Phys. Rep. **270**:143–215 (1996). 14, 103

[32] C. Bohren and D. Huffman, *Absorption and Scattering of Light by Small Particles*, Wiley Science Series, Wiley (2008). 14

[33] N. Ghosh, A. Pradhan, P. K. Gupta, S. Gupta, V. Jaiswal, and R. P. Singh, *Depolarization of light in a multiply scattering medium: Effect of the refractive index of a scatterer*, Phys. Rev. E **70**:066607 (2004). 15, 67

[34] M. Xu and R. R. Alfano, *Random Walk of Polarized Light in Turbid Media*,

Phys. Rev. Lett. **95**:213901 (2005). 15, 67
[35] J. Goodman, *Speckle Phenomena in Optics: Theory and Applications*, Roberts & Company (2007). 15, 44, 50, 53, 110
[36] J. C. Dainty, *Laser speckle and related phenomena*, Springer-Verlag Berlin; New York (1975). 15, 43
[37] J. W. Goodman, *Some fundamental properties of speckle∗*, J. Opt. Soc. Am. **66**(11):1145–1150 (1976). 15
[38] N. Antipa, G. Kuo, R. Heckel, B. Mildenhall, E. Bostan, R. Ng, and L. Waller, *DiffuserCam: lensless single-exposure 3D imaging*, Optica **5**(1):1–9 (2018). 15
[39] N. K. Metzger, R. Spesyvtsev, G. D. Bruce, B. Miller, G. T. Maker, G. Malcolm, M. Mazilu, and K. Dholakia, *Harnessing speckle for a sub-femtometre resolved broadband wavemeter and laser stabilization*, Nat. Commun. **8**:15610 (2017). 15
[40] C. Ventalon and J. Mertz, *Dynamic speckle illumination microscopy with translated versus randomized speckle patterns*, Opt. Express **14**(16):7198–7209 (2006). 15
[41] M. Pascucci, S. Ganesan, A. Tripathi, O. Katz, V. Emiliani, and M. Guillon, *Compressive three-dimensional super-resolution microscopy with speckle-saturated fluorescence excitation*, Nat. Comm. **10**(1):1327 (2019). 15
[42] R. Pappu, B. Recht, J. Taylor, and N. Gershenfeld, *Physical One-Way Functions*, Science **297**(5589):2026–2030 (2002). 15
[43] Y. Liu, P. Yu, Y. Li, and L. Gong, *Exploiting light field imaging through scattering media for optical encryption*, OSA Contin. **3**(11):2968–2975 (2020). 15
[44] A. Darskij and V. Markov, *Measurement of small displacements by speckle holography*, Opt. Laser Technol. **21**(3):193–197 (1989). 15
[45] I. M. Vellekoop and A. P. Mosk, *Focusing coherent light through opaque strongly scattering media*, Opt. Lett. **32**(16):2309–2311 (2007). 17, 57
[46] E. G. van Putten, D. Akbulut, J. Bertolotti, W. L. Vos, A. Lagendijk, and A. P. Mosk, *Scattering Lens Resolves Sub-100 nm Structures with Visible Light*, Phys. Rev. Lett. **106**:193905 (2011). 17, 57
[47] C. Park, J.-H. Park, C. Rodriguez, H. Yu, M. Kim, K. Jin, S. Han, J. Shin, S. H. Ko, K. T. Nam, Y.-H. Lee, Y.-H. Cho, and Y. Park, *Full-Field Subwavelength Imaging Using a Scattering Superlens*, Phys. Rev. Lett. **113**:113901 (2014). 17, 57
[48] X. Xu, H. Liu, and L. Wang, *Time-reversed ultrasonically encoded optical focusing into scattering media*, Nat. Photonics **5**:154–157 (2011). 17, 57
[49] Y. Choi, C. Yoon, M. Kim, T. D. Yang, C. Fang-Yen, R. R. Dasari, K. J. Lee, and W. Choi, *Scanner-Free and Wide-Field Endoscopic Imaging by Using a Single Multimode Optical Fiber*, Phys. Rev. Lett. **109**:203901 (2012). 17, 57
[50] I. N. Papadopoulos, S. Farahi, C. Moser, and D. Psaltis, *Focusing and scanning light through a multimode optical fiber using digital phase conjugation*, Opt. Express **20**(10):10583–10590 (2012). 17, 57

[51] R. Horstmeyer, B. Judkewitz, I. M. Vellekoop, S. Assawaworrarit, and C. Yang, *Focusing and scanning light through a multimode optical fiber using digital phase conjugation*, Sci. Rep. **3**(1):3543 (2013). 17, 58

[52] S. A. Goorden, M. Horstmann, A. P. Mosk, B. Škorić, and P. W. H. Pinkse, *Quantum-secure authentication of a physical unclonable key*, Optica **1**(6):421–424 (2014). 17, 58

[53] R. Tyson, *Principles of Adaptive Optics*, CRC Press (2015). 17

[54] I. M. Vellekoop, E. G. van Putten, A. Lagendijk, and A. P. Mosk, *Demixing light paths inside disordered metamaterials*, Opt. Express **16**(1):67–80 (2008). 17, 45

[55] I. M. Vellekoop, *Feedback-based wavefront shaping*, Opt. Express **23**(9):12189–12206 (2015). 17, 39, 90, 96, 102

[56] W. H. Bragg and W. L. Bragg, *The reflection of X-rays by crystals*, Proc. R. Soc. Lond. A **88**(605):428–438 (1913). 18

[57] N. W. Ashcroft and N. D. Mermin, *Solid State Physics*, Holt, Rinehart and Winston (1976). 19, 70, 74, 103

[58] H. M. van Driel and W. L. Vos, *Multiple Bragg wave coupling in photonic band-gap crystals*, Phys. Rev. B **62**:9872–9875 (2000). 20

[59] W. L. Vos and H. M. van Driel, *Higher order Bragg diffraction by strongly photonic fcc crystals: onset of a photonic bandgap*, Phys. Lett. A **272**:101–106 (2000). 20

[60] S. G. Romanov, T. Maka, C. M. Sotomayor Torres, M. Mller, R. Zentel, D. Cassagne, J. Manzanares-Martinez, and C. Jouanin, *Diffraction of light from thin-film polymethylmethacrylate opaline photonic crystals*, Phys. Rev. E **63**:056603 (2001). 20

[61] T. Tajiri, S. Takahashi, C. A. M. Harteveld, Y. Arakawa, S. Iwamoto, and W. L. Vos, *Reflectivity of three-dimensional GaAs photonic band-gap crystals of finite thickness*, Phys. Rev. B **101**:235303 (2020). 20

[62] R. Sprik, B. A. van Tiggelen, and A. Lagendijk, *Optical emission in periodic dielectrics*, Europhys. Lett. **35**(4):265–270 (1996). 20

[63] W. L. Barnes, S. A. R. Horsley, and W. L. Vos, *Classical antennae, quantum emitters, and densities of optical states*, J. Opt. (2020). 20

[64] V. P. Bykov, *Spontaneous emission in a periodic structure*, Sov. Phys. JETP **35**:269–273 (1972). 20

[65] S. John and J. Wang, *Quantum electrodynamics near a photonic band gap: Photon bound states and dressed atoms*, Phys. Rev. Lett. **64**(20):2418–2421 (1990). 20

[66] W. L. Vos and L. A. Woldering, *Cavity quantum electrodynamics with three-dimensional photonic bandgap crystals*, in M. Ghulinyan and L. Pavesi (editors), *Light Localisation and Lasing: Random and Quasi-random Photonic Structures*, pp. 180–213, Cambridge University (2015). 20, 70, 74

[67] G. S. Smith, M. P. Kesler, and J. G. Maloney, *Dipole antennas used with all-dielectric, woodpile photonic-bandgap reflectors: Gain, field patterns, and input impedance*, Microw. Opt. Technol. Lett. **21**(3):191–196 (1998). 20

[68] P. Bermel, C. Luo, L. Zeng, L. C. Kimerling, and J. D. Joannopoulos,

Improving thin-film crystalline silicon solar cell efficiencies with photonic crystals, Opt. Express **15**:16986 (2007). 20, 83

[69] R. B. Wehrspohn and J. Üpping, *3D photonic crystals for photon management in solar cells*, J. Opt. **14**:024003 (2012). 20, 83

[70] A. F. Koenderink, A. Alú, and A. Polman, *Nanophotonics: Shrinking light-based technology*, Science **348**(6234):516–521 (2015). 20, 90

[71] A. David, H. Benisty, and C. Weisbuch, *Photonic crystal light-emitting sources*, Reports Prog. Phys. **75**:126501 (2012). 20

[72] J. Wang and M. Qi, *Design of a compact mode and polarization converter in three-dimensional photonic crystals*, Opt. Express **20**(18):20356–20367 (2012). 20

[73] Z. Y. Li and K. M. Ho, *Waveguides in three-dimensional layer-by-layer photonic crystals*, J. Opt. Soc. Am. B **20**(5):801–809 (2003). 20

[74] S. A. Rinne, F. García-Santamara, and P. V. Braun, *Embedded cavities and waveguides in three-dimensional silicon photonic crystals* , Nat. Photonics **2**:52–56 (2008). 20, 22, 83, 97, 104, 116

[75] T. Tajiri, S. Takahashi, Y. Ota, K. Watanabe, S. Iwamoto, and Y. Arakawa, *Three-dimensional photonic crystal simultaneously integrating a nanocavity laser and waveguides*, Optica **6**:296–299 (2019). 20, 82

[76] A. Tandaechanurat, S. Ishida, D. Guimard, M. Nomura, S. Iwamoto, and Y. Arakawa, *Lasing oscillation in a three-dimensional photonic crystal nanocavity with a complete bandgap*, Nat. Photonics **5**:91–94 (2011). 20

[77] R. V. Nair, A. K. Tiwari, S. Mujumdar, and B. N. Jagatap, *Photonic-band-edge-induced lasing in self-assembled dye-activated photonic crystals*, Phys. Rev. A **85**:023844 (2012). 20

[78] A. A. Clerk, M. H. Devoret, S. M. Girvin, F. Marquardt, and R. J. Schoelkopf, *Introduction to quantum noise, measurement, and amplification*, Rev. Mod. Phys. **82**(2):1155–1208 (2010). 20, 83, 97

[79] A. F. Koenderink, A. Lagendijk, and W. L. Vos, *Optical extinction due to intrinsic structural variations of photonic crystals*, Phys. Rev. B **72**:153102 (2005). 21, 95, 100, 105

[80] C. P. Mavidis, A. C. Tasolamprou, S. B. Hasan, T. Koschny, E. N. Economou, M. Kafesaki, C. M. Soukoulis, and W. L. Vos, *The local density of optical states in the 3D band gap of a finite photonic crystal*, Phys. Rev. B **101**:235309 (2020). 21, 30, 97, 105

[81] J.-M. Gérard, *Solid-state cavity-quantum electrodynamics with self-assembled quantum dots*, vol. 90, pp. 269–315, Springer (2003). 21

[82] P. R. Villeneuve, S. Fan, J. D. Joannopoulos, K.-Y. Lim, G. S. Petrich, L. A. Kolodziejski, and R. Reif, *Air-bridge microcavities*, Appl. Phys. Lett. **67**(2):167–169 (1995). 22

[83] A. R. M. Zain, N. P. Johnson, M. Sorel, and R. M. D. L. Rue, *Ultra high quality factor one dimensional photonic crystal/photonic wire microcavities in silicon-on-insulator (SOI)*, Opt. Express **16**(16):12084–12089 (2008). 22

[84] S. G. Johnson, P. R. Villeneuve, S. Fan, and J. D. Joannopoulos, *Linear waveguides in photonic-crystal slabs*, Phys. Rev. B **62**:8212–8222 (2000).

22

[85] A. Mekis, J. C. Chen, I. Kurland, S. Fan, P. R. Villeneuve, and J. D. Joannopoulos, *High transmission through sharp bends in photonic crystal waveguides*, Phys. Rev. Lett. **77**(18):3787–3790 (1996). 22

[86] Y. Akahane, T. Asano, B.-S. Song, and S. Noda, *High-Q photonic nanocavity in a two-dimensional photonic crystal*, Nature **425**(6961):944–947 (2003). 22

[87] S. Noda, A. Chutinan, and M. Imada, *Trapping and emission of photons by a single defect in a photonic bandgap structure*, Nature **407**(6804):608–610 (2000). 22

[88] O. Painter, R. K. Lee, A. Scherer, A. Yariv, J. D. O'Brien, P. D. Dapkus, and I. Kim, *Two-Dimensional Photonic Band-Gap Defect Mode Laser*, Science **284**(5421):1819–1821 (1999). 22, 104

[89] M. Lončar, T. Yoshie, A. Scherer, P. Gogna, and Y. Qiu, *Low-threshold photonic crystal laser*, Appl. Phys. Lett. **81**(15):2680–2682 (2002). 22

[90] R. Colombelli, K. Srinivasan, M. Troccoli, O. Painter, C. F. Gmachl, D. M. Tennant, A. M. Sergent, D. L. Sivco, A. Y. Cho, and F. Capasso, *Quantum Cascade Surface-Emitting Photonic Crystal Laser*, Science **302**(November):1374–1377 (2003). 22

[91] X. Yang, M. Yu, D.-L. Kwong, and C. W. Wong, *All-Optical Analog to Electromagnetically Induced Transparency in Multiple Coupled Photonic Crystal Cavities*, Phys. Rev. Lett. **102**:173902 (2009). 22

[92] S. Dhuey, A. Testini, A. Koshelev, N. Borys, J. R. Piper, M. Melli, P. J. Schuck, C. Peroz, and S. Cabrini, *Three-dimensional woodpile photonic crystals for visible light applications*, J. of Phys. Comm. **1**(1):015004 (2017). 22, 104, 116

[93] E. Yablonovitch, T. J. Gmitter, R. D. Meade, A. M. Rappe, K. D. Brommer, and J. D. Joannopoulos, *Donor and acceptor modes in photonic band structure*, Phys. Rev. Lett. **67**:3380–3383 (1991). 22, 104

[94] A. Yariv, Y. Xu, R. K. Lee, and A. Scherer, *Coupled-resonator optical waveguide: a proposal and analysis*, Opt. Lett. **24**(11):711–713 (1999). 23, 105

[95] M. Bayindir, B. Temelkuran, and E. Ozbay, *Propagation of photons by hopping: A waveguiding mechanism through localized coupled cavities in three-dimensional photonic crystals*, Phys. Rev. B **61**:R11855–R11858 (2000). 23, 105

[96] H. Altug and J. Vučković, *Photonic crystal nanocavity array laser*, Opt. Express **13**(22):8819–8828 (2005). 23, 105

[97] S. A. Hack, J. J. W. van der Vegt, and W. L. Vos, *Cartesian light: Unconventional propagation of light in a three-dimensional superlattice of coupled cavities within a three-dimensional photonic band gap*, Phys. Rev. B **99**:115308 (2019). 23, 30, 97, 105, 112, 116

[98] H. Gersen, T. J. Karle, R. J. P. Engelen, W. Bogaerts, J. P. Korterik, N. F. van Hulst, T. F. Krauss, and L. Kuipers, *Direct Observation of Bloch Harmonics and Negative Phase Velocity in Photonic Crystal Waveguides*, Phys. Rev. Lett. **94**:123901 (2005). 23

[99] M. Sandtke and L. Kuipers, *Spatial distribution and near-field coupling of surface plasmon polariton Bloch modes*, Phys. Rev. B **77**:235439 (2008). 23

[100] L. A. Woldering, W. R. Tjerkstra, H. V. Jansen, I. D. Setija, and W. L. Vos, *Periodic arrays of deep nanopores made in silicon with reactive ion etching and deep UV lithography*, Nanotechnology **19**(14):145304 (2008). 25, 26, 91

[101] J. M. van den Broek, L. A. Woldering, R. W. Tjerkstra, F. B. Segerink, I. D. Setija, and W. L. Vos, *Inverse-woodpile photonic band gap crystals with a cubic diamond-like structure made from single-crystalline silicon*, Adv. Funct. Mater. **22**(1):25–31 (2012). 25, 26, 76

[102] R. W. Tjerkstra, L. A. Woldering, J. M. van den Broek, F. Roozeboom, I. D. Setija, and W. L. Vos, *Method to pattern etch masks in two inclined planes for three-dimensional nano- and microfabrication*, J. Vac. Sci. Technol. B **29**:061604 (2011). 25

[103] S. R. Huisman, R. V. Nair, A. Hartsuiker, L. A. Woldering, A. P. Mosk, and W. L. Vos, *Observation of Sub-Bragg Diffraction of Waves in Crystals*, Phys. Rev. Lett. **108**:083901 (2012). 26, 91, 100

[104] D. Devashish, *3D periodic photonic nanostructures with disrupted symmetries*, Ph.D. thesis, University of Twente (2017). 28

[105] K. M. Ho, C. T. Chan, C. M. Soukoulis, R. Biswas, and M. Sigalas, *Photonic band gaps in three dimensions: New layer-by-layer periodic structures*, Solid State Commun. **89**(5):413–416 (1994). 27, 82

[106] nanocops, *Animation: 3D Photonic Crystal with a Diamond Structure* (2012). 27

[107] R. Hillebrand, S. Senz, W. Hergert, and U. Gösele, *Macroporous-silicon-based three-dimensional photonic crystal with a large complete band gap*, J. Appl. Phys. **94**(4):2758–2760 (2003). 27, 74

[108] M. Maldovan and E. L. Thomas, *Diamond-structured photonic crystals*, Nat. Mater. **3**:593–600 (2004). 27

[109] L. A. Woldering, A. P. Mosk, R. W. Tjerkstra, and W. L. Vos, *The influence of fabrication deviations on the photonic band gap of three-dimensional inverse woodpile nanostructures*, J. Appl. Phys. **105**(9):093108 (2009). 27, 74, 85

[110] M. Adhikary, R. Uppu, C. A. M. Harteveld, D. A. Grishina, and W. L. Vos, *Experimental probe of a complete 3D photonic band gap*, Opt. Express **28**(3):2683–2698 (2020). 27, 107

[111] D. Devashish, S. B. Hasan, J. J. W. van der Vegt, and W. L. Vos, *Reflectivity calculated for a three-dimensional silicon photonic band gap crystal with finite support*, Phys. Rev. B **95**:155141 (2017). 29, 70, 71, 72, 73, 74, 76, 79, 80, 81, 107

[112] D. A. Grishina, C. A. M. Harteveld, L. A. Woldering, and W. L. Vos, *Method for making a single-step etch mask for 3D monolithic nanostructures*, Nanotechnology **26**(50):505302 (2015). 27, 76

[113] D. A. Grishina, *3D Silicon Nanophotonics*, Ph.D. thesis, University of Twente (2017). 27

[114] M. D. Leistikow, A. P. Mosk, E. Yeganegi, S. R. Huisman, A. Lagendijk, and W. L. Vos, *Inhibited Spontaneous Emission of Quantum Dots Observed in a 3D Photonic Band Gap*, Phys. Rev. Lett. **107**:193903 (2011). 30, 70

[115] L. A. Woldering, A. P. Mosk, and W. L. Vos, *Design of a three-dimensional photonic band gap cavity in a diamondlike inverse woodpile photonic crystal*, Phys. Rev. B **90**:115140 (2014). 30

[116] M. S. Thijssen, R. Sprik, J. E. G. J. Wijnhoven, M. Megens, T. Narayanan, A. Lagendijk, and W. L. Vos, *Inhibited Light Propagation and Broadband Reflection in Photonic Air-Sphere Crystals*, Phys. Rev. Lett. **83**:2730–2733 (1999). 31, 71

[117] G. Ctistis, A. Hartsuiker, E. van der Pol, J. Claudon, W. L. Vos, and J. M. Gérard, *Optical characterization and selective addressing of the resonant modes of a micropillar cavity with a white light beam*, Phys. Rev. B **82**(19):195330 (2010). 31, 81

[118] S. R. Huisman, R. V. Nair, L. A. Woldering, M. D. Leistikow, A. P. Mosk, and W. L. Vos, *Signature of a three-dimensional photonic band gap observed on silicon inverse woodpile photonic crystals*, Phys. Rev. B **83**(20):205313 (2011). 31, 71, 74, 76, 81

[119] H. Pedersen, *The roughness dependence of partially developed, monochromatic speckle patterns*, Opt. Commun. **12**(2):156–159 (1974). 44

[120] E. Jakeman, *Speckle Statistics With A Small Number Of Scatterers*, Opt. Eng. **23**(4):453–461 (1984). 44

[121] T. Tuthill, R. Sperry, and K. Parker, *Deviations from Rayleigh statistics in ultrasonic speckle*, Ultrason. Imaging **10**(2):81–89 (1988). 44

[122] S. Kubota and J. W. Goodman, *Very efficient speckle contrast reduction realized by moving diffuser device*, Appl. Opt. **49**(23):4385–4391 (2010). 44

[123] H. Fujii and T. Asakura, *Statistical properties of image speckle patterns in partially coherent light*, Nouvelle Revue d'Optique **6**(1):5–14 (1975). 44

[124] D. D. Postnov, X. Cheng, S. E. Erdener, and D. A. Boas, *Choosing a laser for laser speckle contrast imaging*, Sci. Rep. **9**(1):2542 (2019). 44

[125] V. Srikant and D. R. Clarke, *On the optical band gap of zinc oxide*, J. Appl. Phys. **83**(10):5447–5451 (1998). 45

[126] J. A. Johnson, J. J. Heidenreich, R. A. Mantz, P. M. Baker, and M. S. Donley, *A multiple-scattering model analysis of zinc oxide pigment for spacecraft thermal control coatings*, Prog. Org. Coat. **47**(3):432–442 (2003). Keystone 2002. 45

[127] S. S. Kumar, P. Venkateswarlu, V. R. Rao, and G. N. Rao, *Synthesis, characterization and optical properties of zinc oxide nanoparticles*, Int. Nano Lett. **3**(1):30 (2013). 45

[128] H. F. Wilson, C. Tang, and A. S. Barnard, *Morphology of Zinc Oxide Nanoparticles and Nanowires: Role of Surface and Edge Energies*, J. Phys. Chem. C **120**(17):9498–9505 (2016). 46

[129] E. G. van Putten, *Disorder-Enhanced Imaging with Spatially Controlled Light*, Ph.D. thesis, University of Twente (2011). 45, 60

[130] S. J. Kirkpatrick, D. D. Duncan, and E. M. Wells-Gray, *Detrimental effects of speckle-pixel size matching in laser speckle contrast imaging*, Opt. Lett.

33(24):2886–2888 (2008). 51

[131] J. C. Ramirez-San-Juan, E. Mendez-Aguilar, N. Salazar-Hermenegildo, A. Fuentes-Garcia, R. Ramos-Garcia, and B. Choi, *Effects of speckle/pixel size ratio on temporal and spatial speckle-contrast analysis of dynamic scattering systems: Implications for measurements of blood-flow dynamics*, Biomed. Opt. Express **4**(10):1883–1889 (2013). 51

[132] H. Elgala, R. Mesleh, and H. Haas, *Indoor optical wireless communication: potential and state-of-the-art*, IEEE Commun. Mag. **49**(9):56–62 (2011). 58

[133] H. Haas, L. Yin, Y. Wang, and C. Chen, *What is LiFi?*, J. Light. Technol **34**(6):1533–1544 (2016). 58

[134] H. Haas, L. Yin, C. Chen, S. Videv, D. Parol, E. Poves, H. Alshaer, and M. S. Islim, *Introduction to indoor networking concepts and challenges in LiFi*, J. Opt. Commun. Netw. **12**(2):A190–A203 (2020). 58

[135] F. van Beijnum, E. G. van Putten, A. Lagendijk, and A. P. Mosk, *Frequency bandwidth of light focused through turbid media*, Opt. Lett. **36**(3):373–375 (2011). 58, 62, 64, 65

[136] A. Z. Genack, *Optical Transmission in Disordered Media*, Phys. Rev. Lett. **58**:2043–2046 (1987). 58

[137] M. P. van Albada, J. F. de Boer, and A. Lagendijk, *Observation of long-range intensity correlation in the transport of coherent light through a random medium*, Phys. Rev. Lett. **64**:2787–2790 (1990). 58

[138] J. F. de Boer, M. P. van Albada, and A. Lagendijk, *Transmission and intensity correlations in wave propagation through random media*, Phys. Rev. B **45**:658–666 (1992). 58

[139] B. Shapiro, *Large Intensity Fluctuations for Wave Propagation in Random Media*, Phys. Rev. Lett. **57**:2168–2171 (1986). 58

[140] M. J. Stephen and G. Cwilich, *Intensity correlation functions and fluctuations in light scattered from a random medium*, Phys. Rev. Lett. **59**:285–287 (1987). 58, 59

[141] S. Feng, C. Kane, P. A. Lee, and A. D. Stone, *Correlations and Fluctuations of Coherent Wave Transmission through Disordered Media*, Phys. Rev. Lett. **61**:834–837 (1988). 58, 59

[142] J. F. de Boer , *Optical fluctuations on the transmission and reflection of mesoscopic systems*, Ph.D. thesis, University of Amsterdam (1995). 59

[143] O. L. Muskens and A. Lagendijk, *Method for broadband spectroscopy of light transport through opaque scattering media*, Opt. Lett. **34**(4):395–397 (2009). 62

[144] O. L. Muskens and A. Lagendijk, *Broadband enhanced backscattering spectroscopy of strongly scattering media*, Opt. Express **16**(2):1222–1231 (2008). 65

[145] V. Y. F. Leung, A. Lagendijk, T. W. Tukker, A. P. Mosk, W. L. IJzerman, and W. L. Vos, *Interplay between multiple scattering, emission, and absorption of light in the phosphor of a white light-emitting diode*, Opt. Express **22**(7):8190–8204 (2014). 65

[146] J.-M. Lourtioz, H. Benisty, V. Berger, J.-M. Gérard, D. Maystre, and

A. Tchelnokov, *Photonic Crystals*, Springer Verlag (2008). 70
[147] M. A. Noginov, G. Dewar, M. McCall, and N. I. Zheludev (editors), *Tutorials in Complex Photonic Media*, Cambridge University (2009). 70
[148] E. N. Economou, *The Physics of Solids*, Springer-Verlag (2010). 70
[149] C. Lòpez, *Materials aspects of photonic crystals*, Adv. Mater. **15**:1679–1704 (2003). 70
[150] H. Benisty and C. Weisbuch, *Photonic crystals*, in E. Wolf (editor), *Progress in Optics*, vol. 49, pp. 177–313, Elsevier (2006). 70
[151] J. F. Galisteo Lòpez, M. Ibisate, R. Sapienza, L. S. Froufe-Pérez, À. Blanco, and C. Lòpez, *Self-Assembled Photonic Structures*, Adv. Mater. **23**:30–69 (2011). 70
[152] S. Ogawa, M. Imada, S. Yoshimoto, M. Okano, and S. Noda, *Control of light emission by 3D photonic crystals*, Science **305**:227–229 (2004). 70
[153] P. Lodahl, A. F. Van Driel, I. S. Nikolaev, A. Irman, K. Overgaag, D. Vanmaekelbergh, and W. L. Vos, *Controlling the dynamics of spontaneous emission from quantum dots by photonic crystals*, Nature **430**(7000):654–657 (2004). 70, 97
[154] K. Aoki, D. Guimard, M. Nishioka, M. Nomura, S. Iwamoto, and Y. Arakawa, *Coupling of quantum-dot light emission with a three-dimensional photonic-crystal nanocavity*, Nat. Photonics **2**(11):688–692 (2008). 70
[155] A. F. Koenderink, L. Bechger, H. Schriemer, A. Lagendijk, and W. L. Vos, *Broadband fivefold reduction of vacuum fluctuations probed by dyes in photonic crystals*, Phys. Rev. Lett. **88**:143903 (2002). 71
[156] A. F. Koenderink, L. Bechger, A. Lagendijk, and W. L. Vos, *An experimental study of strongly modified emission in inverse opal photonic crystals*, phys. stat. sol. (a) **197**:648–661 (2003). 71
[157] S. B. Hasan, A. P. Mosk, W. L. Vos, and A. Lagendijk, *Finite-size Scaling of the Density of States in Photonic Band Gap Crystals*, Phys. Rev. Lett. **120**:237402 (2018). 71
[158] S. Y. Lin, J. G. Fleming, D. L. Hetherington, B. K. Smith, R. Biswas, K. M. Ho, M. M. Sigalas, W. Zubrzycki, S. R. Kurtz, and J. Bur, *A three-dimensional photonic crystal operating at infrared wavelengths*, Nature **394**(6690):251–253 (1998). 71
[159] S. Noda, K. Tomoda, N. Yamamoto, and A. Chutinan, *Full Three-Dimensional Photonic Bandgap Crystals at Near- Infrared Wavelengths*, Science **289**(5479):604–606 (2000). 71, 82
[160] A. Blanco, E. Chomski, S. Grabtchak, M. Ibisate, S. John, S. W. Leonard, C. Lòpez, F. Meseguer, H. Miguez, J. P. Mondla, G. A. Ozin, O. Toader, and H. M. van Driel, *Large-scale synthesis of a silicon photonic crystal with a complete three-dimensional bandgap near 1.5 micrometres*, Nature **405**(6785):437–440 (2000). 71, 82
[161] Y. A. Vlasov, X.-Z. Bo, J. C. Sturm, and D. J. Norris, *On-chip natural assembly of silicon photonic bandgap crystals*, Nature **414**:289–293 (2001). 71, 82
[162] E. Palacios-Lidón, A. Blanco, M. Ibisate, F. Meseguer, C. Lòpez, and

J. Sánchez-Dehesa, *Optical study of the full photonic band gap in silicon inverse opals*, Appl. Phys. Lett. **81**:4925–4927 (2002). 71

[163] M. Qi, E. Lidorikis, P. T. Rakich, S. G. Johnson, J. D. Joannopoulos, E. P. Ippen, and H. I. Smith, *A three-dimensional optical photonic crystal with designed point defects*, Nature **429**:538–542 (2004). 71, 83

[164] J. Schilling, J. White, A. Scherer, G. Stupian, R. Hillebrand, and U. Gösele, *Three-dimensional macroporous silicon photonic crystal with large photonic band gap*, Appl. Phys. Lett. **86**(1):011101 (2005). 71

[165] F. García-Santamaría, M. Xu, V. Lousse, S. Fan, P. V. Braun, and J. A. Lewis, *A germanium inverse woodpile structure with a large photonic band gap*, Adv. Mater. **19**(12):1567–1570 (2007). 71

[166] G. Subramania, Y. J. Lee, I. Brener, T. Luk, and P. Clem, *Nanolithographically fabricated titanium dioxide based visible frequency three dimensional gap photonic crystal*, Opt. Express **15**(20):13049–13057 (2007). 71

[167] S. Takahashi, K. Suzuki, M. Okano, M. Imada, T. Nakamori, Y. Ota, K. Ishizaki, and S. Noda, *Direct creation of three-dimensional photonic crystals by a top-down approach*, Nat. Mater. **8**(9):721–725 (2009). 71

[168] I. Staude, M. Thiel, S. Essig, C. Wolff, K. Busch, G. von Freymann, and M. Wegener, *Fabrication and characterization of silicon woodpile photonic crystals with a complete bandgap at telecom wavelengths*, Opt. Lett. **35**(7):1094 (2010). 71

[169] G. Subramania, Q. Li, Y. J. Lee, J. J. Figiel, G. T. Wang, and A. J. Fische, *Gallium nitride based logpile photonic crystals*, Nano Lett. **11**(11):4591–4596 (2011). 71

[170] A. Frölich, J. Fischer, T. Zebrowski, K. Busch, and M. Wegener, *Titania woodpiles with complete three-dimensional photonic bandgaps in the visible*, Adv. Mater. **25**(26):3588–3592 (2013). 71

[171] C. Marichy, N. Muller, L. S. Froufe-Pérez, and F. Scheffold, *High-quality photonic crystals with a nearly complete band gap obtained by direct inversion of woodpile templates with titanium dioxide*, Sci. Rep. **6**:21818 (2016). 71

[172] W. M. Robertson, G. Arjavalingam, R. D. Meade, K. D. Brommer, A. M. Rappe, and J. D. Joannopoulos, *Measurement of photonic band structure in a two-dimensional periodic dielectric array*, Phys. Rev. Lett. **68**:2023–2026 (1992). 71

[173] K. Sakoda, *Optical properties of photonic crystals*, Springer Verlag (2005). 71, 92

[174] Z. Y. Li and Z. Q. Zhang, *Fragility of photonic band gaps in inverse-opal photonic crystals*, Phys. Rev. B **62**:1516–1519 (2002). 72

[175] Z. L. Wang, C. T. Chan, W. Y. Zhang, Z. Chen, N. B. Ming, and P. Sheng, *Optical properties of inverted opal photonic band gap crystals with stacking disorder*, Phys. Rev. E **67**:016612 (2003). 72

[176] D. A. Grishina, C. A. M. Harteveld, A. Pacureanu, D. Devashish, A. Lagendijk, P. Cloetens, and W. L. Vos, *X-ray imaging non-destructively identifies functional 3D photonic nanostructures*, ACS Nano **13**:in print (2019).

72, 74, 76, 79, 82

[177] N. Muller, J. Haberko, C. Marichy, and F. Scheffold, *Photonic hyperuniform networks obtained by silicon double inversion of polymer templates* , Optica **4**:361–366 (2017). 72, 82, 98

[178] S. Datta, C. T. Chan, K. M. Ho, and C. M. Soukoulis, *Effective dielectric constant of periodic composite structures*, Phys. Rev. B **48**(20):14936–14943 (1993). 74, 82

[179] Ioffe Institute (Petersburg), *Semiconductors*, `http://www.ioffe.ru/SVA/NSM/Semicond/`. 76

[180] T. G. Euser, A. J. Molenaar, J. G. Fleming, B. Gralak, A. Polman, and W. L. Vos, *All-optical octave-broad ultrafast switching of Si woodpile photonic band gap crystals*, Phys. Rev. B **77**(11):115214 (2008). 76

[181] W. L. Vos, H. M. van Driel, M. Megens, A. F. Koenderink, and A. Imhof, *Experimental probes of the optical properties of photonic crystals*, in C. M. Soukoulis (editor), *Photonic Crystals and Light Localization in the 21st century*, pp. 181–198, Kluwer (2001). 76

[182] W. L. Vos, M. Megens, C. M. van Kats, and P. Bösecke, *X-ray Diffraction of Photonic Colloidal Single Crystals*, Langmuir **13**(23):6004–6008 (1997). 82

[183] J. E. G. J. Wijnhoven, L. Bechger, and W. L. Vos, *Fabrication and characterization of large macroporous photonic crystals in titania*, Chem. Mater. **13**:4486–4499 (2001). 82

[184] A. V. Petukhov, D. G. A. L. Aarts, I. P. Dolbnya, E. H. A. de Hoog, K. Kassapidou, G. J. Vroege, W. Bras, and H. N. W. Lekkerkerker, *High-Resolution Small-Angle X-Ray Diffraction Study of Long-Range Order in Hard-Sphere Colloidal Crystals*, Phys. Rev. Lett. **88**:208301 (2002). 82

[185] K. P. Furlan, E. Larsson, A. Diaz, M. Holler, T. Krekeler, M. Ritter, A. Y. Petrov, M. Eich, R. Blick, G. A. Schneider, I. Greving, R. Zierold, and R. Janssen, *Photonic materials for high-temperature applications: Synthesis and characterization by X-ray ptychographic tomography*, Appl. Mater. Today **13**:359–369 (2018). 82

[186] K. Ishizaki, M. Koumura, K. Suzuki, K. Gondaira, and S. Noda, *Realization of three-dimensional guiding of photons in photonic crystals*, Nat. Photonics **7**:133–137 (2013). 82, 97

[187] D. Devashish, O. S. Ojambati, S. B. Hasan, J. J. W. van der Vegt, and W. L. Vos, *Three-dimensional photonic band gap cavity with finite support: Enhanced energy density and optical absorption*, Phys. Rev. B **99**:075112 (2019). 83, 113, 124

[188] M. Fink, D. Cassereau, A. Derode, C. Prada, P. Roux, M. Tanter, J.-L. Thomas, and F. Wu, *Time-reversed acoustics*, Rep. Progr. Phys. **63**(12):1933 (2000). 89

[189] S. A. Cummer, J. Christensen, and A. Alù, *Controlling sound with acoustic metamaterials*, Nat. Rev. Mater. **1**(3):16001 (2016). 89

[190] S. Neusser and D. Grundler, *Magnonics: Spin waves on the nanoscale*, Adv. Mater. **21**(28):2927–2932 (2009). 90

[191] K. Wagner, A. Kákay, K. Schultheiss, A. Henschke, T. Sebastian,

and H. Schultheiss, *Magnetic domain walls as reconfigurable spin-wave nanochannels*, Nat. Nanotechnol. **11**(5):432–436 (2016). 90

[192] K. Klyukin, L. L. Tao, E. Y. Tsymbal, and V. Alexandrov, *Defect-Assisted Tunneling Electroresistance in Ferroelectric Tunnel Junctions*, Phys. Rev. Lett. **121**:056601 (2018). 90

[193] M. Aspelmeyer, T. J. Kippenberg, and F. Marquardt, *Cavity optomechanics*, Rev. Mod. Phys. **86**:1391–1452 (2014). 90

[194] W. Li and S. Fan, *Nanophotonic control of thermal radiation for energy applications*, Opt. Express **26**(12):15995–16021 (2018). 90

[195] A. Tandaechanurat, S. Ishida, D. Guimard, M. Nomura, S. Iwamoto, and Y. Arakawa, *Large-scale integration of wavelength-addressable all-optical memories on a photonic crystal chip*, Nat. Photonics **5**:91–94 (2011). 90, 97

[196] J. L. O'Brien, A. Furusawa, and J. Vučković, *Photonic quantum technologies*, Nat. Photonics **3**(12):687–695 (2009). 90

[197] E. Kuramochi, K. Nozaki, A. Shinya, K. Takeda, T. Sato, S. Matsuo, H. Taniyama, H. Sumikura, and M. Notomi, *Large-scale integration of wavelength-addressable all-optical memories on a photonic crystal chip*, Nat. Photonics **8**:474–481 (2014). 90

[198] N. W. Ashcroft and N. D. Mermin, *Solid state physics*, Holt, Rinehart, and Winston, New York, NY (1976). 90

[199] J. D. Joannopoulos, S. G. Johnson, J. N. Winn, and R. D. Meade, *Photonic crystals: molding the flow of light*, Princeton University Press, Princeton, NJ (2011). 90

[200] R. B. Wehrspohn and J. Üpping, *3D photonic crystals for photon management in solar cells*, J. Opt. **14**(2):024003 (2012). 90

[201] H. Inan, M. Poyraz, F. Inci, M. A. Lifson, M. Baday, B. T. Cunningham, and U. Demirci, *Photonic crystals: emerging biosensors and their promise for point-of-care applications*, Chem. Soc. Rev. **46**(2):366–388 (2017). 90

[202] A. F. Koenderink and W. L. Vos, *Light Exiting from Real Photonic Band Gap Crystals is Diffuse and Strongly Directional*, Phys. Rev. Lett. **91**:213902 (2003). 90

[203] D. A. Grishina, C. A. M. Harteveld, A. Pacureanu, D. Devashish, A. Lagendijk, P. Cloetens, and W. L. Vos, *X-ray Imaging of Functional Three-Dimensional Nanostructures on Massive Substrates*, ACS Nano **13**(12):13932–13939 (2019). 90

[204] A. P. Mosk, A. Lagendijk, G. Lerosey, and M. Fink, *Controlling waves in space and time for imaging and focusing in complex media*, Nat. Photonics **6**(5):283–292 (2012). 90

[205] S. Rotter and S. Gigan, *Light fields in complex media: Mesoscopic scattering meets wave control*, Rev. Mod. Phys. **89**(1):015005 (2017). 90, 95

[206] J. Harris, V. Grillo, E. Mafakheri, G. C. Gazzadi, S. Frabboni, R. W. Boyd, and E. Karimi, *Structured quantum waves*, Nat. Phys. **11**(8):629–634 (2015). 90

[207] Y. Xie, W. Wang, H. Chen, A. Konneker, B.-I. Popa, and S. A. Cummer, *Wavefront modulation and subwavelength diffractive acoustics with*

an acoustic metasurface, Nat. Commun. **5**(1):1–5 (2014). 90

[208] R. Sarma, A. G. Yamilov, S. Petrenko, Y. Bromberg, and H. Cao, *Control of energy density inside a disordered medium by coupling to open or closed channels*, Phys. Rev. Lett. **117**(8):086803 (2016). 93

[209] R. Sarma, A. Yamilov, and H. Cao, *Enhancing light transmission through a disordered waveguide with inhomogeneous scattering and loss*, Appl. Phys. Lett. **110**(2):021103 (2017). 93

[210] P. Fang, C. Tian, L. Zhao, Y. P. Bliokh, V. Freilikher, and F. Nori, *Universality of eigenchannel structures in dimensional crossover*, Phys. Rev. B **99**(9):094202 (2019). 93

[211] W. L. Vos, A. Lagendijk, and A. P. Mosk, *Light propagation and emission in complex photonic media*, in M. Ghulinyan and L. Pavesi (editors), *Light Localisation and Lasing: Random and Quasi-random Photonic Structures*, pp. 1–12, Cambridge University Press (2015). 93

[212] E. Akkermans and G. Montambaux, *Mesoscopic Physics of Electrons and Photons*, Cambridge University Press (2007). 93, 99, 103

[213] D. Wiersma, *Disordered photonics*, Nat. Photonics **7**(3):188–196 (2013). 93, 99

[214] I. M. Vellekoop and A. P. Mosk, *Universal optimal transmission of light through disordered materials*, Phys. Rev. Lett. **101**:120601 (2008). 95

[215] S. M. Popoff, A. Goetschy, S. F. Liew, A. D. Stone, and H. Cao, *Coherent control of total transmission of light through disordered media*, Phys. Rev. Lett. **112**:133903 (2014). 95

[216] D. A. B. Miller, *Waves, modes, communications, and optics: a tutorial*, Adv. Opt. Photon. **11**(3):679–825 (2019). 95

[217] F. Evers and A. D. Mirlin, *Anderson transitions*, Rev. Mod. Phys. **80**:1355–1417 (2008). 96, 101

[218] A. Goetschy and A. Stone, *Filtering random matrices: the effect of incomplete channel control in multiple scattering*, Phys. Rev. Lett. **111**(6):063901 (2013). 97

[219] C. W. Hsu, A. Goetschy, Y. Bromberg, A. D. Stone, and H. Cao, *Broadband coherent enhancement of transmission and absorption in disordered media*, Phys. Rev. Lett. **115**(22):223901 (2015). 97

[220] J. Pendry, A. MacKinnon, and A. Pretre, *Maximal fluctuations – A new phenomenon in disordered systems*, Physica A **168**(1):400–407 (1990). 97

[221] We expect qualitatively similar results for light incident along the orthogonal crystal direction as the crystal also supports a gap along the ΓM direction. Since our crystal thus has a 2D band gap, the results hold for a 2D band gap, and likely also for a full 3D band gap. 97

[222] M. Fujita, S. Takahashi, Y. Tanaka, T. Asano, and S. Noda, *Simultaneous inhibition and redistribution of spontaneous light emission in photonic crystals*, Science **308**(5726):1296–1298 (2005). 97

[223] N. Vats, S. John, and K. Busch, *Theory of fluorescence in photonic crystals*, Phys. Rev. A **65**(4):043808 (2002). 97

[224] S. F. Liew, J.-K. Yang, H. Noh, C. F. Schreck, E. R. Dufresne, C. S. O'Hern, and H. Cao, *Photonic band gaps in three-dimensional network structures*

with short-range order, Phys. Rev. A **84**:063818 (2011). 98

[225] A. Ledermann, L. Cademartiri, M. Hermatschweiler, C. Toninelli, G. A. Ozin, D. S. Wiersma, M. Wegener, and G. Von Freymann, *Three-dimensional silicon inverse photonic quasicrystals for infrared wavelengths*, Nat. Mater. **5**(12):942–945 (2006). 98

[226] W. Man, M. Florescu, E. P. Williamson, Y. He, S. R. Hashemizad, B. Y. Leung, D. R. Liner, S. Torquato, P. M. Chaikin, and P. J. Steinhardt, *Isotropic band gaps and freeform waveguides observed in hyperuniform disordered photonic solids*, Proc. Natl. Acad. Sci. U.S.A. **110**(40):15886–15891 (2013). 98

[227] S. Vignolini and N. Bruns, *Bioinspiration across all length scales of materials*, Adv. Mater. **30**(19):1801687 (2018). 98

[228] R. A. Sepkhanov, Y. B. Bazaliy, and C. W. J. Beenakker, *Extremal transmission at the Dirac point of a photonic band structure*, Phys. Rev. A **75**:063813 (2007). 98

[229] S. Yves, R. Fleury, T. Berthelot, M. Fink, F. Lemoult, and G. Lerosey, *Crystalline metamaterials for topological properties at subwavelength scales*, Nat. Commun. **8**(1):16023 (2017). 98

[230] T. Ozawa, H. M. Price, A. Amo, N. Goldman, M. Hafezi, L. Lu, M. C. Rechtsman, D. Schuster, J. Simon, O. Zilberberg, and I. Carusotto, *Topological photonics*, Rev. Mod. Phys. **91**:015006 (2019). 98

[231] J. G. F. Francis, *The QR Transformation A Unitary Analogue to the LR Transformation: Part 1*, Comput. J. **4**(3):265–271 (1961). 101

[232] J. G. F. Francis, *The QR Transformation: Part 2*, Comput. J. **4**(4):332–345 (1962). 101

[233] V. Kublanovskaya, *On some algorithms for the solution of the complete eigenvalue problem*, USSR Comput. Math. & Math. Phys. **1**(3):637–657 (1962). 101

[234] O. N. Dorokhov, *On the coexistence of localized and extended electronic states in the metallic phase*, Solid State Commun. **51**:381–384 (1984). 101

[235] P. Mello, P. Pereyra, and N. Kumar, *Macroscopic approach to multichannel disordered conductors*, Ann. Phys. **181**:290–317 (1988). 101

[236] C. W. J. Beenakker, *Random-matrix theory of quantum transport*, Rev. Mod. Phys. **69**:731–808 (1997). 101

[237] D. Akbulut, T. Strudley, J. Bertolotti, E. P. A. M. Bakkers, A. Lagendijk, O. L. Muskens, W. L. Vos, and A. P. Mosk, *Optical transmission matrix as a probe of the photonic strength*, Phys. Rev. A **94**(4):043817 (2016). 101

[238] W. van Haeringen and D. Lenstra (editors), *Analogies in Optics and Micro Electronics*, Springer, Dordrecht (1990). 103

[239] M. C. W. van Rossum and T. M. Nieuwenhuizen, *Multiple scattering of classical waves: microscopy, mesoscopy, and diffusion*, Rev. Mod. Phys. **71**:313–371 (1999). 103

[240] K. Inoue and K. Ohtaka, *Photonic Crystals: Physics, Fabrication and Applications*, Springer Series in Optical Sciences, Springer Berlin Heidelberg (2004). 103

[241] N. Ashcroft and N. Mermin, *Solid State Physics*, Cengage Learning (2011).

104

[242] S. T. Pantelides, *The electronic structure of impurities and other point defects in semiconductors*, Rev. Mod. Phys. **50**:797–858 (1978). 104

[243] S. Zwerdling, K. J. Button, B. Lax, and L. M. Roth, *Internal Impurity Levels in Semiconductors: Experiments in p-Type Silicon*, Phys. Rev. Lett. **4**:173–176 (1960). 104

[244] A. Onton, P. Fisher, and A. K. Ramdas, *Spectroscopic Investigation of Group-III Acceptor States in Silicon*, Phys. Rev. **163**:686–703 (1967). 104

[245] F. Bassani, G. Iadonisi, and B. Preziosi, *Electronic impurity levels in semiconductors*, Rep. Prog. Phys. **37**(9):1099–1210 (1974). 104

[246] N. Hauke, A. Tandaechanurat, T. Zabel, T. Reichert, H. Takagi, M. Kaniber, S. Iwamoto, D. Bougeard, J. J. Finley, G. Abstreiter, and Y. Arakawa, *A three-dimensional silicon photonic crystal nanocavity with enhanced emission from embedded germanium islands*, New J. Phys. **14**(8):083035 (2012). 104

[247] A. J. Danner, J. J. Raftery, N. Yokouchi, and K. D. Choquette, *Transverse modes of photonic crystal vertical-cavity lasers*, Appl. Phys. Lett. **84**(7):1031–1033 (2004). 104

[248] A. Sugitatsu, T. Asano, and S. Noda, *Characterization of line-defect-waveguide lasers in two-dimensional photonic-crystal slabs*, Appl. Phys. Lett. **84**(26):5395–5397 (2004). 104

[249] T. van der Sar, J. Hagemeier, W. Pfaff, E. C. Heeres, S. M. Thon, H. Kim, P. M. Petroff, T. H. Oosterkamp, D. Bouwmeester, and R. Hanson, *Deterministic nanoassembly of a coupled quantum emitter-photonic crystal cavity system*, Appl. Phys. Lett. **98**(19):193103 (2011). 104

[250] J. D. Thompson, T. G. Tiecke, N. P. de Leon, J. Feist, A. V. Akimov, M. Gullans, A. S. Zibrov, V. Vuletić, and M. D. Lukin, *Coupling a Single Trapped Atom to a Nanoscale Optical Cavity*, Science **340**(6137):1202–1205 (2013). 104

[251] H. Altug, D. Englund, and J. Vučković, *Ultrafast photonic crystal nanocavity laser*, Nat. Phys. **2**:484–488 (2006). 105

[252] M. Kozon, M. Schlottbom, J. J. W. van der Vegt, and W. L. Vos, *Classification of Confined wave states in 3D superlattices using finite-size scaling*, in *Conference on Lasers and Electro-Optics Europe & European Quantum Electronics Conference (CLEO/Europe-EQEC)* (2021). 107

[253] J. Dainty, *Laser Speckle and Related Phenomena*, Topics in Applied Physics, Springer, Berlin Heidelberg (2013). 110

[254] J. Li, M. Chong, J. Zhu, Y. Li, J. Xu, P. Wang, Z. Shang, Z. Yang, R. Zhu, and X. Cao, *35% efficient nonconcentrating novel silicon solar cell*, Appl. Phys. Lett. **60**(18):2240–2242 (1992). 116

[255] Luque, Antonio and Martí, Antonio, *Increasing the Efficiency of Ideal Solar Cells by Photon Induced Transitions at Intermediate Levels*, Phys. Rev. Lett. **78**:5014–5017 (1997). 116

[256] C. Tablero, P. Palacios, J. Fernndez, and P. Wahnn, *Properties of intermediate band materials*, Sol. Energy Mater. Sol. Cells **87**(1):323–331 (2005). 116

[257] J. T. Sullivan, C. B. Simmons, J. J. Krich, A. J. Akey, D. Recht, M. J. Aziz, and T. Buonassisi, *Methodology for vetting heavily doped semiconductors for intermediate band photovoltaics: A case study in sulfur-hyperdoped silicon*, J. Appl. Phys. **114**(10):103701 (2013). 116

[258] Q. Liu, Z. Cai, D. Han, and S. Chen, *Natural Intermediate Band in I2-II-IV-VI4 Quaternary Chalcogenide Semiconductors*, Sci. Rep. **8**(1):1604 (2018). 116

[259] M. P. A. Fisher, P. B. Weichman, G. Grinstein, and D. S. Fisher, *Boson localization and the superfluid-insulator transition*, Phys. Rev. B **40**:546–570 (1989). 117

[260] T. Vreman, *Shaping waves in 3D photonic band gap crystals*, Master's thesis, University of Twente (2021). 124

Nederlandse samenvatting

In dit proefschrift wordt de gecontroleerde lichtvoortplanting bestudeerd in verschillende nanofotonische media, te weten willekeurig verstrooiende, periodieke en superperiodieke media. Diverse voorbeelden van deze materialen zijn experimenteel bestudeerd op de verschillende mogelijke manieren om (gecontroleerde) interactie tussen licht in het nabij-infrarood en deze materialen. Het uiteindelijke doel is om geheel nieuwe kennis en expertise op te bouwen over de bijzondere voortplantingswijze van licht in de super-periodieke systemen. Deze bijzondere structuren bestaan uit een driedimensionaal (3D) rooster van gekoppelde optische trilholtes. Een dergelijke configuratie geeft toegang tot een vorm van lichttransport die tot nu toe alleen bekend was in elektronische systemen. Deze bijzondere toestanden kan toegang geven tot nog niet eerder waargenomen faseovergangen zoals, Anderson lokalisatie. Tevens zijn deze structuren CMOS-compatibel en functioneel telecom banden. Dit geeft in de toekomst de mogelijkheid om deze structuren te combineren met andere bestaande electro-optische componenten. Hieronder volgt een korte samenvatting per hoofdstuk:

Hfdst. 2 Dit hoofdstuk geeft een gedetailleerd overzicht van de experimentele opstelling die wordt gebruikt in alle hieropvolgende hoofdstukken. Met deze opstelling is het mogelijk om zowel reflectie, transmissie alsmede laterale verstrooiing van diverse optische media te meten. Verder stelt een spatial light modulator (SLM) ons in staat om golfront-vorming (wavefront shaping) toe te passen. Het speciale aan deze opstelling is dat het deze metingen kan doen over een breed spectraal bereik van 950 nm tot 2000 nm met een nauwe spectrale lijnbreedte van 0.7 nm. Alle relevante technische details worden behandeld en de limitaties van de opstelling worden verkend. Daarnaast wordt een overzicht gegeven van de CMOS-compatiblele optische monsters die doorgemeten worden in hoofdstukken 5, 6 en 7, namelijk 2D fotonische kristallen, 3D fotonische kristallen, en 3D superperiodieke kristallen.

Hfdst. 3 De waargenomen spikkel in elk experiment is het gevolg van een samenspel tussen enerzijds het verstrooiende materiaal, anderzijds de details van de lichtbron, optiek en detector. Typisch wordt spikkel gemeten in een klein frequentiebereik met een nauwbandige lichtbron omdat dit licht een lange coherentielengte heeft. Echter, de opstelling zoals beschreven in hoofdstuk 2 is een breedbandige opstelling. De relatief grote lijnbreedte reduceert de

coherentie van het licht en beïnvloedt daarmee de spikkelstatistiek. In dit hoofdstuk onderzoeken we hoe deze wisselwerking tussen bandbreedte en coherentie de speckle beïnvloeden met behulp van metingen aan een monster bestaande uit ZnO nanodeeltjes. We laten zien dat de spikkel statistiek afwijkt van de verwachtte exponentiele verdeling. Deze afwijking is het gevolg van zowel de gebruikte lichtbron en als meede de veel ruis in de detector. Deze conclusie is gevalideerd met metingen met een -bij benadering- monochromatisch lichtbron en een detector met minder ruis. De nauwkeurigheid van de opstelling voor het meten van spikkelstatistiek isbepaald, en deze is voldoende voor de metingen die in de volgende hoofdstukken worden omschreven.

Hfdst. 4 Door de spatiële fase van het golffront van het inkomende licht te veranderen is het mogelijk om achter een verstrooiend medium een focus te realiseren . Dit proces heet "wavefront shaping"(WFS). De fase van het optimale golffront is uniek voor de frequentie van het inkomende licht, echter is er wel een correlatie met het optimale golffront bij dichtbij zijnde frequenties. In dit hoofdstuk onderzoeken we de spectrale breedte van deze correlatie voor het gehele bereik van telecom banden . Hieruit volgt dat voor zwak verstrooiende media het mogelijk is om de spectrale bandbreedte van WFS enorm te verhogen tot tientallen THz (ongeveer 100 nm) in het nabij infrarood. Deze resultaten geven de mogelijkheid aan om WFS te implementeren met verstrooiingsmedia voor het focusseren van licht over een breed frequentiebereik.

Hfdst. 5 De frequentieafhankelijke reflectie van 3D fotonische kristallen met inverse houtstapelstructuur zijn bestudeerd. Deze kristallen hebben een goed ontwikkelde blandkloof in diverse telecom banden en hebben -naar ons weten- een record maximum van 96% reflectie in de bandkloof. Dit is belangrijk omdat dit ten eerste een veelbelovende aanwijzing is dat de kristallen van hoge kwaliteit zijn met zeer weinig fabricagefouten. De fabricagefouten van met name de nanoporiën en de roosterafstand zijn klein genoeg dat ze de collectieve Bloch modi zwak verstoren. Ten tweede is een hoge reflectie essentieel voor de afschermen van de trilholtes en eventuele activering daarvan door bijvoorbeeld quantum dots te plaatsen in deze trilholtes.

Hfdst. 6 Spectrale metingen van zowel de reflectiviteit alsmede de laterale verstrooiing bij 2D-fotonische kristallen laten de richtingsafhankelijkheid zien van de fotonische bandkloof. In de bandkloof zijn geen Bloch modi aanwezig en kan inkomend licht niet verder dan de Bragglengte doordingen. Echter, imperfecties in het kristal maken het mogelijk om inkomend licht in de bandkloof tot wel 8× verder dan deze Bragglengte door te laten dringen. Hierbij wordt gebruik gemaakt van wavefront shaping (WFS). De toegenomen intensiteit wordt met grote precisie verklaard met een geheel nieuw theoretisch mesoscopisch model. Hiermee laten we zien dat functionele eenheden, bijvoorbeeld trilholten, binnen in de fotonische kristallen alsnog optisch geadresseerd kunnen worden.

Hfdst. 7 Een structuur van periodiek geplaatste en gekoppelde trilholtes ingebed in een 3D fotonisch kristal vormen een superperiodiek fotonisch medium. Een dergelijk medium geeft de mogelijkheid om licht te laten springen tussen de verschillende naburige trilholtes. Dit springen vindt plaats binnen de bandkloof van het kristal, waar normaal gesproken geen enkele licht voortplanting mogelijk is. Zowel reflectie- alsmede verstrooiingsmetingen aan een dergelijk superperiodieke kristal tonen het bestaan van deze cavity modes binnen in de bandkloof van de 3D fotonisch kristal aan. Dit vormt de allereerste observatie van het geheel nieuwe vorm van lichttransport in een dergelijk 3D super-periodiek fotonisch kristal.

Acknowledgments

It has been an amazing experience for me during the past 4 years, combining the thrill of moving to a far-away land with a completely different culture and getting the opportunity to work as a PhD candidate in one of the prestigious universities of Western Europe. I feel fortunate to be able to work here and I could grow a lot professionally while at the same time providing a very good and comfortable environment. At the end of this thesis, I take this opportunity to offer my sincere gratitude to all the people who have helped me make this journey possible.

First of all, I would like to thank my supervisor **Willem** for his excellent guidance in carrying out the research work. I learned a lot from your in-depth knowledge in physics and your ability to deliver the information in a clear and simplistic manner. Your organization skills are admirable, knowing the workload you have as the chair of COPS. Yet you manage to find time for discussions, be it about physics, writing, or technical details of experimental setups. I really appreciate your efforts to make me more confident and positive about my work. I am also very thankful to you for showing me how to present my work in a clear way so that everyone can understand, by guiding the audience through the presentation. You have been a very supportive supervisor.

I also take this opportunity to thank my co-supervisor **Ravi**, who took the primary responsibility to help me kick-start my PhD. You provided me the much appreciated support to learn all the details of the experimental setup that I inherited from you. Your knowledge in science is admirable and I liked the fact that when anyone in the group had a question, they would approach you and you would be happy to help and provide a solution.

I am very grateful to the other committee members Profs. **Wim Bogaerts**, **Allard Mosk**, **Sonia Garcia Blanco**, and **Marcelo Ackermann** for taking their valuable time to read and evaluate my thesis.

I would like to express my gratitude to the other senior members of the group. **Ad**, you are like the physics backbone of the group and every one of us has benefited from this. I learned a lot from you about scattering theory and also from the discussions with you, whether in the group meetings or in person. **Pepijn**, your enthusiasm for science is inspiring, and I am very happy that you now have your own chair AQO. Also, thank you very much for inviting me to apply for a PhD at COPS. **Bill**, your occasional visits to UT were very pleasant and I could learn a lot from the discussions I had with you. **Jan**, it is really nice to see your group growing and the very interesting research that you have been pursuing.

Rebecca, you are an inspiration to many young scientists with your enthusiasm and positivity.

During my PhD research, I had the much-appreciated support from my colleagues at COPS and AQO. **Marek**, all my photonic crystal experimental results would have half their meaning without your theoretical support. Also thank you for making the illustration of the cavity superlattice. I thank former colleagues **Devashish**, **Sjoerd**, and **Diana** for the helpful discussions and based on whose work I proceeded with my project and derive meaningful conclusions. **Cock**, I am grateful to you for fabricating the silicon samples, and your continued effort to fabricate better samples despite numerous problems in the cleanroom. Thank you **Chris** for your contributions to the experimental setup. **Timon**, it was one amazing experience being your masters' thesis supervisor. I enjoyed working with you, and the discussions that often started out of your curious questions were really interesting and I also learned a lot in the process. **Matthijs**, thank you so much for all the help in the lab and repairing the lock-in amplifier. Together with Matthijs, I am also grateful to have colleagues like **Reinier**, **Mario**, and **Ozan** who never hesitated to step forward whenever I needed some help in the lab.

I would like to thank the very helpful support staff of the group. **Nicole**, thank you very much for all the secretarial help, and I really admire your kind and cheerful personality. **Cock**, thank you for taking care of many technical and bureaucratic tasks. Thank you **Marlon** and **Richard** for your immediate ICT support whenever there was any problem with computers.

My project being part of the NWO-TTW Free-Form Scattering Optics (FFSO) program, I had the opportunity to interact with all the other members of the program from two other universities namely the group of **Wilbert IJzerman** from TU Eindhoven, and that of **Paul Urbach** and **Aurèle Adam** from TU Delft, and a number of industrial partners ASML, Demcon, Lumileds, Schott, Signify, and TNO. It was a pleasure to interact with the co-PhD students in the program from TU/e and TUD, *viz.*, **Alex**, **Lotte, Maikel, Robert, Thomas, and Ví**. The regular meetings with all the members have been very interesting where we could discuss the research of various groups as well as connect the industry needs to our projects to come up with new ideas.

Being part of the Applied Nanophotonics (ANP) cluster of the UT, I got the opportunity to know colleagues from various optics groups at the university. The monthly ANP meetings have been very useful and interesting to share and discuss research problems, progress, and get useful feedback. It was a pleasure to meet **Abhilash**, **Caterina**, **Jinfeng**, **Lissane**, **Michiel**, and **Simen** from different research groups within ANP. It was a fun and an unforgettable experience for me to organize the ANP retreat meeting in 2018, together with **Pepijn**, **Jesse**, and **Ward**. I also take this opportunity to thank **Allard** for his useful inputs on my work.

I thank **Arie den Boef**, **Patrick Tinnemans**, **Vahid Bastani**, **Wim Coene**, and **Scott Middlebrooks** from ASML for inspiring discussions related to signal extraction from noisy data for identifying superlattice modes.

For all the scientific and social interactions, I would like to thank past and pre-

sent COPS and now AQO members **Alfredo**, **Andreas**, **Ben**, **Charlie**, **Chris**, **Daan**, **Diana**, **Duy**, **Devashish**, **Evangelos**, **Femi**, **Frank**, **Haider**, **Innes**, **Jelmer**, **Kayleigh**, **Klaas-Jan**, **Lars C.**, **Lars vdH.**, **Lucas**, **Maarten**, **Malaquias**, **Marek**, **Mario**, **Marnix**, **Maryna**, **Matthijs**, **Melissa**, **Ozan**, **Peter**, **Pim**, **Ravi**, **Reinier**, **Sjoerd Shivan**,, **Shravan**, **Shweta**, **Timon**, **Tristan**, and **Willemijn**. These colleagues have been really amazing and I had a great time with them both inside and outside work. The variety of discussions at the coffee table about all kinds of random topics, making fun of one another have been a routine during the breaks. Before the pandemic, the regular evening outings with these friendly colleagues were really nice to get to know one another. During my first year, former colleagues **Evangelos**, **Tristan**, and **Ravi** have been very supportive to get me used to and explore the new place. I had a good time discussing many different things with **Evangelos**. **Pepijn**, you have always been very friendly and kind, and I really enjoy talking to you. Thank you so much for being so supportive to me since my first day. It was a great pleasure for me to take care of your bird during your vacations. **Jelmer**, I find it amusing that you still *blame* me for your bird-watching obsession, and thanks for the tons of bird pictures from you every weekend and the regular updates on Grebe spotting. **Tristan**, your excitement about mango and elephant is just precious. **Reinier**, I hope someday you will be able to make memes that are actually funny, and also thank you very much for helping me with writing the Dutch summary of this thesis. **Chris**, I appreciate that you repeat the same stories with the same enthusiasm every time a new person joins, and also all the efforts to make fun of me. **Mario**, it was really nice to have you as my office mate, and thank you so much for the amazing T-rex skull that you have 3D printed. **Lars**, I admire your endless enthusiasm to join projects and explore new ideas and also your passion for good tea. Thank you for your help with writing the Dutch summary. **Marek**, it was nice to have your chilled personality around. **Shweta**, thanks for your efforts in trying to make me socialize more, it is really nice to have a friend like you. **Ozan**, I had a lot of fun discussing with you all kinds of gossips and complaining about random things. **Alfredo**, you are so enthusiastic and passionate about whatever you do, specifically your exceptional climbing skills. **Melissa**, you are a great addition to the group with your chemistry knowledge and your dynamic presence.

I also thank colleagues from our neighboring group LPNO both for technical help in the lab and interesting conversations at our common coffee table. **Klaus**, you are an amazing physicist and a great storyteller. Any kind of discussion with you is always interesting and uplifting. **David**, thank you for being in my PhD qualifier committee, and I also admire your intelligent and cheerful personality.

I would like to extend my gratitude to my former supervisor **Sushil** from TIFR, India, and his group members whose guidance and motivation lead to to be here in the first place.

During my PhD time, I am glad to be associated with cultural activities. I feel very happy to be a member of the vocal group **Musilon**. Singing and meeting with you guys every week was very helpful to relax after the tiring working days, and performing at the half-yearly and other concerts have been

a great experience. Sad that we had to switch to online rehearsals due to the pandemic, but I still enjoyed editing the online concerts. It was also really fun to sing Christmas songs with the **MESA+ choir**, and I thank **Caterina** for her amazing conducting skills.

My sincere gratitude goes towards **Reinier**, whose constant care, support, and motivation through my best and the worst times kept me going the past few years. The time spent with you has been indulging, from the amusing vacations, cooking adventures, the weekend walks in nature, to the endless discussions on all kinds of topics. I also take this opportunity to thank your loving and supportive parents.

All that I have achieved in my life so far would not have been possible without the unconditional love and support of my family: my dear **father** and **sister**. My father has inspired me to study technical subjects and has been supporting me and my dreams and trusted my decisions despite all the difficulties. Being a PhD graduate herself, my sister **Nabanita** has been my motivation and our regular conversations have always made me feel at home, even though I could not visit them for a really long time because of the pandemic years of covid-19.

I will cherish the memory of my PhD life forever, and I thank all my colleagues, friends, and family again, whether mentioned or not here, for their support, contributions, and the good times.

-Manashee